Chair of Materials Physics

Doctoral Thesis

# Improving the mechanical properties of metallic glasses through structure and stress engineering: A molecular dynamics simulations study

Xudong Yuan

October 2022

MONTANUNIVERSITÄT LEOBEN
www.unileoben.ac.at

## AFFIDAVIT

I declare on oath that I wrote this thesis independently, did not use other than the specified sources and aids, and did not otherwise use any unauthorized aids.

I declare that I have read, understood, and complied with the guidelines of the senate of the Montanuniversität Leoben for "Good Scientific Practice".

Furthermore, I declare that the electronic and printed version of the submitted thesis are identical, both, formally and with regard to content.

Date 03.10.2022

Xudong Yuan

Signature Author
Xudong Yuan

MONTANUNIVERSITÄT LEOBEN
www.unileoben.ac.at

Xudong Yuan
Jahnstraße 12
8700 Leoben

To the Dean of graduate Studies of the Montanuniversitaet Leoben

**Declaration of Approval for the Digital Publication of Scientific Theses**

I am aware that the thesis entitled "Improving the mechanical properties of metallic glasses through structure and stress engineering: A molecular dynamics simulations study" will be subject to a plagiarism assessment and may be stored by Montanuniversität Leoben for an unlimited period of time.

I agree that the University Library of Montanuniversität Leoben may publish the thesis open access in the World Wide Web. For embargoed theses this will be done after the embargo expires.

Note: in case you refuse the open access publication in the World Wide Web, the thesis will only be published in printed form (after a possible embargo has expired) in the University Library (dissertations also in the Austrian National Library).

I hereby agree with the open access publication of my thesis on the World Wide Web:

Ⓧ Yes

O No

Date 03.10.2022

Xudong Yuan

Signature Author

# Acknowledges

First, I would like to sincerely appreciate Dr. Daniel Şopu for his support and patient guidance. His professional knowledge and rigorous attitude toward science helped me so much and without him, I could not finish my Ph.D.. From simulation setup and data analysis to scientific writing, I learned plenty of things from him and I am so proud that I can have the opportunity to study with him.

I would like to appreciate my supervisor Prof. Jürgen Eckert for giving me the opportunity to do my Ph.D. at ESI. I appreciate his insightful opinion on my work and the great help to my publications. I also would like to thank Prof. Kaikai Song for supporting me to embark on the road of science work. Without his encouragement and help during my Master's time, I would not had the chance to do my Ph.D..

I am very grateful to my colleague Franco Moitzi for the help in the programming and soft compiling. Great thanks to Dr. Christoph Gammer, Dr. Florian Spieckermann, Dr. Wenping Wu, Dr. Long Zhang, Dr. Huaping Sheng. The discussions with you help me a lot.

I would like to thank the China Scholarship Council for the financial help during my Ph.D. time in the past years. I would like to thank my parents and sister for their selfless love, support, and understanding. In the past, they have provided me excellent help and encouragement and it is my honor to be their family member.

Ph.D. work is not an easy process but thanks to all the friendly people that I met in the past years, your appearance make my life become colorful.

# Abstract

This thesis has further explored the atomic-level deformation mechanism of metallic glasses under various conditions using molecular dynamics simulations and, additionally, exposed the effect of structure rejuvenation/relaxation on the mechanical properties of metallic glasses. In the end, a systematic guide on the design of high-performance metallic glasses which combines strain hardening together with enhanced tensile ductility was provided.

The effects of cooling rate, temperature, and applied strain rate on the tensile deformation behavior of a $Cu_{64}Zr_{36}$ metallic glasses are investigated. An increase in the quenching rate during sample preparation, as well as an increase in the temperature or the applied strain rate, causes a brittle-to-ductile transition in the deformation behavior of metallic glasses. High quenching rates lead to lower energy barriers for activation of local atomic rearrangements as compared to those metallic glasses obtained at low quenching rates. The kinetic energy of the atoms increases dramatically with the increase of loading temperature, which allows the homogeneous activation of shear events. As for the strain rate, faster loading can store a large amount of elastic energy in the glassy matrix and induce a high density of shear events and, therefore, results in a low probability for strain localization and formation of critical shear bands.

Structural rejuvenation is an excitation process that can bring metallic glasses to a higher energy state and usually improve their plasticity. In this work, by using a dilution procedure conducted by randomly removing atoms from the glass matrix, the degree of rejuvenation was systematically controlled and the maximum rejuvenation threshold of $Cu_{64}Zr_{36}$ metallic glasses are identified. The structural relaxation is activated during the rejuvenation process and the dynamic balance between free volume creation and annihilation defines the rejuvenation ability of metallic glasses. Furthermore, loading-unloading tensile tests reveal that stress-induced relaxation of the highly rejuvenated metallic glasses provides strain-hardening, but, can never make them exceed the strength of their initial as-cast state.

To overcome the brittleness of metallic glasses, their structure and chemistry are usually modified. Additionally, the thesis also proved that the mechanical properties of metallic glasses could be controlled by introducing residual stress. During loading, the designed stress modulated metallic glasses heterostructures show enhanced ductility together with strain hardening. The stress heterogeneity leads to shear band multiplication that consequently enhances the macroscopic ductility of metallic glasses. In addition, the residual compressive stress significantly increases the strength of the glass and is responsible for the observed strain hardening

during tensile deformation.

# Kurzfassung

In der vorliegenden Arbeit wurden die atomaren Verformungsmechanismen von metallischen Gläsern unter verschiedenen Bedingungen mit Hilfe von Molekulardynamik Simulationen erforscht. Darüber hinaus wurden die Auswirkungen der Rekristallisierung und Erholungsmechanismen auf die mechanischen Eigenschaften metallischer Gläser untersucht. Schlussendlich wurde ein Leitfaden zur Entwicklung von Hochleistungs-Metallgläsern durch die Kombination von Kaltverfestitung und Zugduktilität erstellt.

Die Auswirkungen der Abkühlungsrate, der Temperatur und der Dehnungsrate auf das Verformungsverhalten von $Cu_{64}Zr_{36}$ metallischen Gläsern wurden untersucht. Bei der Herstellung der Proben führt eine Erhöhung der Abschreckrate, der Temperatur oder der angewandten Dehnungsrate dazu, dass das Verformungsverhalten versprödet. Hohe Abschreckraten führen zu niedrigeren Energiebarrieren für die Aktivierung lokaler atomarer Umlagerungen im Vergleich zu metallischen Gläsern mit niedrigen Abschreckraten. Die kinetische Energie der Atome nimmt mit der Erhöhung der Belastungstemperatur drastisch zu, was eine homogene Aktivierung von Scherereignissen ermöglicht. Was die Dehnungsgeschwindigkeit betrifft, so kann eine schnellere Belastung eine große Menge an elastischer Energie in der glasartigen Matrix speichern und eine hohe Dichte an Scherereignissen hervorrufen, was zu einer geringen Wahrscheinlichkeit für die Lokalisierung der Dehnung und die Bildung kritischer Scherbänder führt.

Die strukturelle Verjüngung ist ein Anregungsprozess, der metallische Gläser in einen höheren Energiezustand versetzen und in der Regel ihre Plastizität verbessern kann. In dieser Arbeit wurde mit Hilfe eines Verdünnungsverfahrens, bei dem nach dem Zufallsprinzip Atome aus der Glasmatrix entfernt wurden, der Grad der Verjüngung systematisch kontrolliert und die maximale Verjüngungsschwelle von $Cu_{64}Zr_{36}$ Metallgläsern ermittelt. Die strukturelle Relaxation wird während des Verjüngungsprozesses aktiviert und das dynamische Gleichgewicht zwischen der Schaffung von freiem Volumen und der Vernichtung definiert die Verjüngungsfähigkeit von metallischen Gläsern. Darüber hinaus zeigen Belastungs-/Entlastungszugversuche, dass die spannungsinduzierte Relaxation der stark verjüngten metallischen Gläser zwar zu einer Kaltverfestigung führt, aber niemals die Festigkeit des ursprünglichen Gusszustandes übersteigen kann.

Um die Sprödigkeit von metallischen Gläsern zu überwinden, werden in der Regel ihre Struktur und Chemie verändert. Außerdem konnten die These nachweisen, dass die mecha-

nischen Eigenschaften von MG durch das Einbringen von Eigenspannungen gesteuert werden können. Während der Belastung zeigen die entworfenen spannungsmodulierten Heterostrukturen aus metallischen Gläsern eine erhöhte Duktilität bei gleichzeitiger Kaltverfestigung. Die Spannungsheterogenität führt zu einer Scherbandvervielfachung, die folglich die makroskopische Duktilität der metallischen Gläser erhöht. Darüber hinaus erhöht die Druckeigenspannung die Festigkeit des Glases erheblich und ist für die beobachtete Kaltverfestigung bei Zugverformung verantwortlich.

# Thesis structure

This thesis consists of two parts. **Part I** includes the general introduction and background, the motivation and object of this work, the basic theory and methods, and the summary of the publications correlated to this thesis. **Part II** presents the main results of the thesis in the form of a paper collection. Four published journal papers are included.

# Contents

# Part I: Introduction, Motivation and Summary

# 1 Introduction

## 1.1 Metallic glasses

### 1.1.1 Brief introduction

The first report about metallic glasses (MGs) can be traced back to 1960 in Caltech, USA. By cooling the metallic liquids with a cooling rate of $10^6$ K/s, Duwez et al. [1] discovered the first binary amorphous alloy $Au_{80}Si_{20}$. At very fast cooling rate, the process of nucleation and growth of the crystalline phase can be inhibited during solidification. Accordingly, MGs inherit a disordered structure from the liquid. Since then, the formation, structure, and properties of this new type of material have attracted increasing attention because of its application potential [2–4].

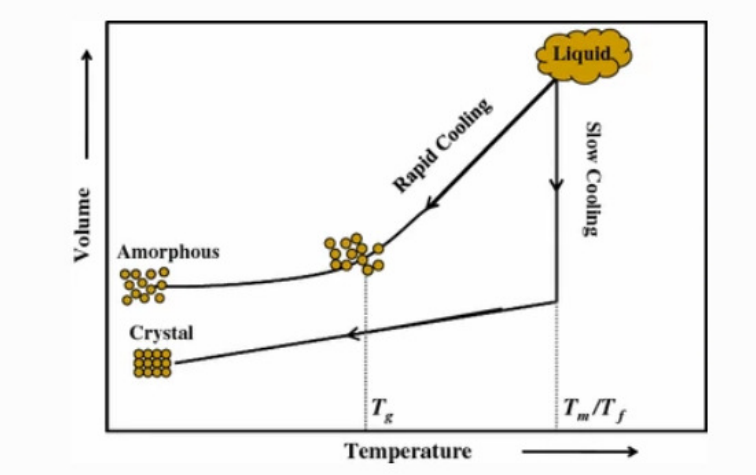


**Figure 1.1:** The volume versus temperature during the glass formation and crystallization processes [5].

Cooling history is vital to the glass formation process. The volume or enthalpy versus the temperature during quenching can be used to describe the glass formation as shown in Fig. 1.1. Obviously, slow cooling will transfer the metallic liquid to typical crystal state, resulting in the abruptly decrease of the volume below melting temperature. On the contrary, fast quenching helps the melt towards the supercooled liquid region and lead to the formation of a "liquind-like" structure. The volume will slowly decrease during the glass formation process and results in the so-called second-order phase transformation. After further decreasing the temperature, the supercooled liquid will finally develops into the amorphous material. By extrapolating the supercooled liquid line and the solid line, one can get one of the most critical definable parameter called the glass transformation temperature ($T_g$). The glass formation region is highly controlled by the dynamic behaviors which can be affected by the cooling rate

during the quenching process.

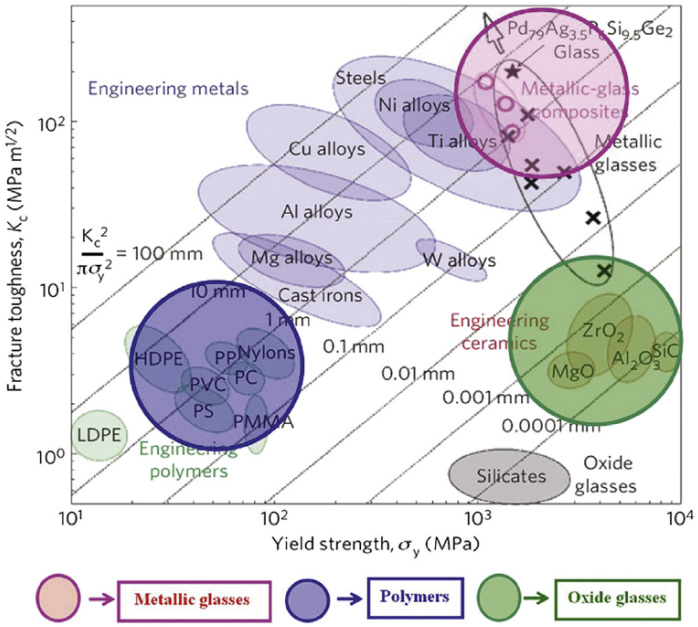


**Figure 1.2:** Schematic illustration of yield strength and fracture toughness of various of materials. MGs and MG-based composites can show both high yield strength and high fracture toughness [6].

Due to the restriction of the production process, MGs specimen geometry could only be formed to thin ribbons or powders in the early days and could only be achieved with sizes of the order of microns [7]. Many efforts have been made by researchers to find MGs with good glass formaing abilities (GFA) in the past decades. In 1969, Turnbull et al. [8] designed a ternary Pd-Si-based amorphous sphere with a diameter of 0.5 mm. Additionaly, Turnbull pointed out that a ratio of $T_g$ to the melting temperature ($T_m$) can be used as a criterion for determining the GFA of an alloy, a metal liquid with $T_g/T_m$ = 2/3 will crystallize within a very narrow temperature range and it can be undercooled at a low cooling rate into the amorphous state [9, 10]. Turnbull's criterion is treated as one of the integral rules in predicting the GFA of metal liquid and it plays a significant role in designing and developing big size MGs. With the guidance of Turnbull's theory, the design of bulk metallic glasses (BMGs) with the size of millimeter-scale becomes possible and a great number of new BMGs with various compositions have been identified.

With the rapid development the field of MGs, Inoue et al. [11, 12] proposed three rules for the production of BMGs with good GFA based on the amount of experimental data: (1) multi-component alloy systems that consists at least three elements; (2) the main constituent elements should have significant difference in atomic size ratios (usually above 12%) ; (3) negative heats of mixing among the main constituent elements. Inoue's empirical rules made a big leap forward in the development of amorphous alloys. More and more BMGs with special

mechanical and chemical properties have been investigated and put into applications [13–16].

### 1.1.2 Atomic structure

The unique formation condition endows the MGs in extortionary properties such as high strength and good elasticity (Fig. 1.2). Identifying the atomic-level structure of the MGs can promote the understanding of their physics and chemical properties. MGs have totally different structures compared to the normal crystal materials and their structure is closely related to their original liquid state, especially the supercooled liquid. Long-range order (LRO) structure is usually inhibited during fast solidification and results in the formation of short-range order (SRO) clusters [17, 18]. Over the years, series of models has been proposed to describe the special atomic packaging style of the glassy system.

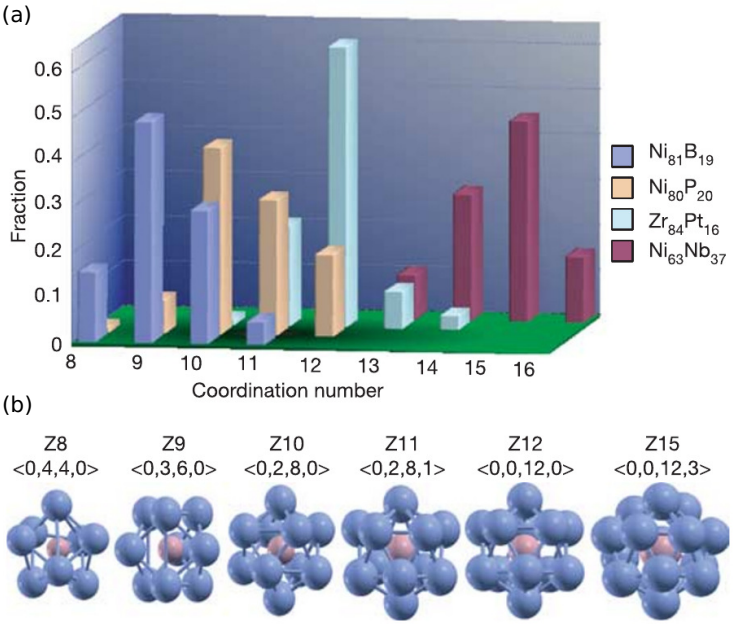


**Figure 1.3:** Schematics of the SRO clusters described by the VP and their distribution in different MG systems. (a): The fraction of VP structures in different MG systems. (b): The packing configurations six kinds of representative VP structures corresponding to different coordination numbers. [19].

The first widely accepted model is the random dense packing model, which was first proposed to describe the structure of liquid and considers a pure liquid as the packaging of hard spheres with single size [20–24]. The model describes the liquid as a coherent and irregular homogeneous system with all atoms that can be seen as rigid balls stacking together and no extra space whose volume is bigger that an atom. This model was proved by Cargill [25] that is useful in interpreting the properties of some amorphous systems. However, due to the neglection of the interaction between atoms, the model can not be used as a universal structural description of the MGs. Hence a more realistic approach comes which describes the interaction of "hard

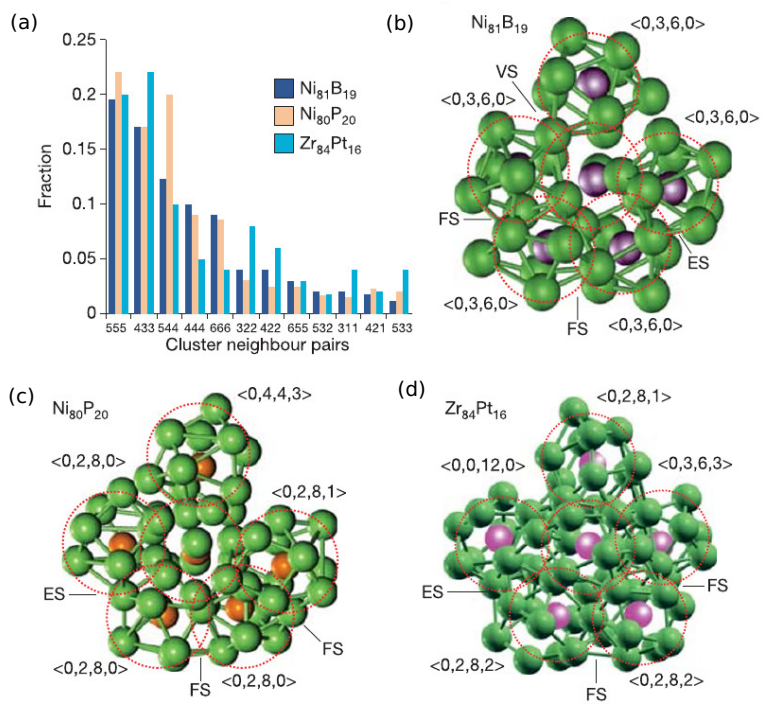


**Figure 1.4:** Illustration of the MRO in the (b) $Ni_{81}B_{19}$, (c) $Ni_{80}P_{20}$ and (d) $Zr_{84}Pt_{16}$ MG systems. (a) shows that the local clusters in the MGs exhibit icosahedral type ordering. For each local cluster, the Voronoi index is given to indicate its identity. FS, ES and VS denote face-sharing, edge-sharing and vertex-sharing, respectively. Adapted from [19].

balls" using pair potentials so that the atoms are not only treated as soft spheres but also have the potential energy between them [24].

Wang [26] first suggested that the MGs should have short range structure which was formed by the stacking of various types of polyhedra [27]. Frank and Kasper [28–30] introduced the well-known polytetrahedral packing model to explain the atomic structure of complex alloys which then became a convincing theory to explain the short range structure in amorphous alloys. This model was examined by the amount of computer simulation work [31–33] and further proved the existence of SRO in the glassy matrix. The best tool for the description of the SRO in glassy materials is the Voronoi tessellation method [34]. Utilizing this tool, the glassy materials can be represented as the combination of various Voronoi polyhedra (VP) around each atom and the VP contains information sufficient to describe the neighborhood of the associated central atom completely [23]. Generally, the VP in the MG systems can be manifested by the Voronoi indexes [n3, n4, n5, n6] where **ni** is the number of i-edged sides of the polyhedron and the sum of **ni** represents the coordination number of the centeral atom. As shown in Fig. 1.3, Sheng et al. [19] identified and modeled the most popular VP clusters in different MG systems and concluded that the fraction of VPs in the glass matrix can vary with different MG systems.

Only the description of SRO is far away from the totally determined structure of MGs and

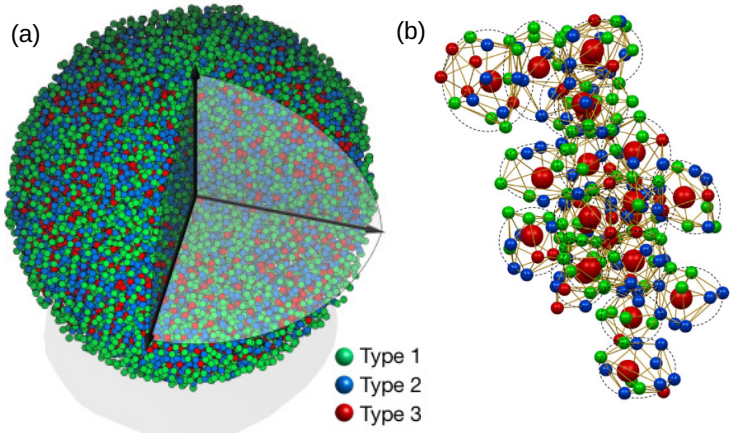


**Figure 1.5:** Schematic of an experimental observed atomic-level structure model of MG. (a) The structure of a glassy nanoparticle with the diameter of 8 nm. Differently colored sprhere representing different types of atoms. (b) The 3D atomic packing model of a MRO clusters within the glassy structure. Adapted from [35].

how the local clusters are connected with each other and arranged in the glassy matrix are then investigated by researchers. Beyond the SRO, the medium-range order (MRO) is the next-level structural organization which describes the connection and configuration of SRO. MRO shows a variety of packing characters depending on the compositions of the glass systems (see Fig. 1.4). Using the pair distribution function, MRO can be represented as the structural features beyond the first peak to a distance of up to 1–2 nm [24] and it effectively exhibits the packing behavior of the SRO on medium-range size. Very recently, J. Miao et al. [35] determines the 3D atomic packaging characteristic in amorphous solid in an experiment with the atomic electron tomography reconstruction method (Fig. 1.5 a). The structure that they investigated corresponded very well to the earlier computational simulation results which prove the existence of the MRO clusters inside MG systems (Fig. 1.5 b).

The characteristic of local SRO and MRO structures is highly dependent on the composition of MGs. Hence, establishing indirect parameters that reflect the structure but can be incorporated into constitutive models is quintessential to understand the structure-property correlation in MGs. One of the effective indicator is free volume that was first proposed to describe the transport processes in liquid of hard spheres by Cohen and Turnbull [36–38]. The free volume $V_f$ can be defined as the volume of the Voronoi cage ($V_m$) less the center atomic core volume $V_a$ [39, 40] and the content of $V_f$ in the glassy matrix is a convenient indicator of the internal glass state [24]. Moreover, the state transition between order and disorder in the glass structure is usually accompanied by the changes in the free volume and many key features of the MG behaviors have been illustrated by the free volume model [40–43]. Besides the free

volume, the configurational potential energy is also one of the widely accepted parameter for the rheology of metallic liquids and the studying of deformation in MGs. With the help of the configurational potential energy model, the thermal dynamic properties of metallic liquids and deformation behavior of MGs have been further investigated by researches [44, 45]. Based on the development of numerous indicators, the structure nature of the amorphous alloys was gradually exposed to our view. Quantitatively analyzing of the changes in the atomic-level structure during the stress- and thermally-induced transitions becomes more and more convenient and, additionally, it provides an effective way to study the structure-properties relationship in MGs.

## 1.2 Relaxation process in metallic glasses

### 1.2.1 Definition of relaxation

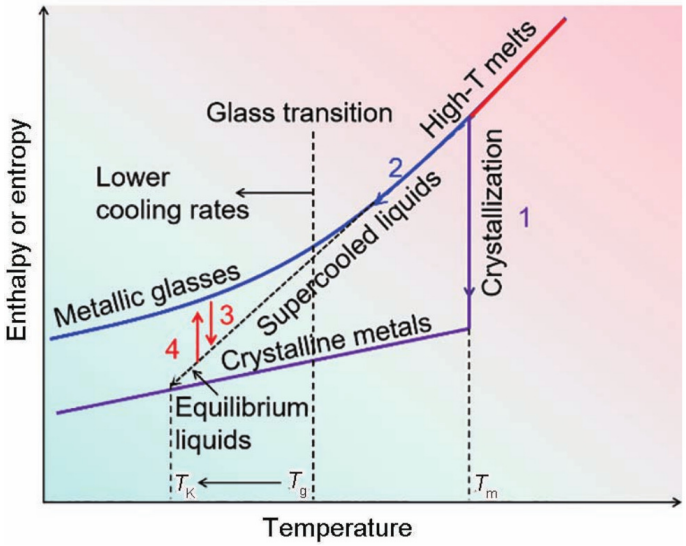


**Figure 1.6:** Schematic illustration of the relationship between enthalpy or entropy and temperature during crystalization (line 1) and glass formation (line 2) process. $T_g$ will decrease with the decrease of cooling rate and the theoretically lowest $T_g$ is Kauzmann Temperature ($T_k$), which corresponds to the ideal stable MGs. Line 3 indicates the transition from less stable to a more stable state (relaxation process) and line 4 represents a contrary process, i.e. rejuvenation [46].

MGs are metastable structures and their energy state is highly determined by the cooling history. The low cooling rate results in the low enthalpy or entropy in the glass and also corresponds to the low $T_g$. Theoretically, the MGs have an ideal stable state with the lowest energy and the corresponding $T_g$ is defined as Kauzmann Temperature ($T_k$) (see Fig. 1.6). The time-dependent change of an MG from one thermodynamic state to another more stable state is called relaxation. Usually, relaxation is a consequence of atomic dynamic behavior that can be activated by the applied external stimuli [47] such as stress or temperature. Spontaneous relaxation is also possible, however, this process usually takes months or years and is defined as

aging. Evidence shows that MGs usually have complex relaxation dynamics, including chemical, mechanical, and structural or stress relaxation [47–49], moreover, the relaxation processes have complicated modes and can cover spacious time and temperature ranges and also in the frequency domain from $10^{-7}$ to $10^{14}$ [47, 49–52]. Basically, two types of relaxation processes, i.e. the $\alpha$ relaxation and the $\beta$ relaxation, which represent two kinds of atomic rearrangements, are worth studying in MG systems.

### 1.2.2 Relaxation mechanisms

Thermally activated relaxation can be detected in glassy materials during the temperature variation process. The $\alpha$ relaxation, also known as main structural relaxation in MG system, can be seen as large scale structural rearrangement [47]. The dramatically temperature-dependent features of $\alpha$ relaxation determine that the relaxation time can be altered orders of magnitude even when the temperature of the glass only decreases several degrees. The $\alpha$ relaxation usually exists in the supercooled liquid region (above $T_g$) and can be seen as frozen in the low temperature [48, 53]. When the temperature of the glass systems is below $T_g$ and continues to decrease, a secondary dynamic behavior gradually starts and becomes dominant which is called $\beta$ relaxation [48, 54]. Unlike the large scale of $\alpha$ relaxation, the $\beta$ relaxation associated with the local structural rearrangement (Fig. 1.7) or the string-like motions of atoms [55] and it is weakly temperature dependent [48]. Typically, dynamical mechanical analysis (DMA) is an effective and most common way in exposing relaxation behavior in MGs due to its wide applicability and high sensitivity in detecting atomic dynamics [48]. The features of relaxation can be represented by two distinct peaks in the temperature-dependent storage and loss modulus curves as shown in Fig. 1.8, the strong $\alpha$ relaxation peak appears at the high temperature and followed by a weaker $\beta$ relaxation wings. Compared to the $\alpha$ relaxation, $\beta$ relaxation demonstrates low amplitude but a more comprehensive temperature range which indicates its wide distribution of relaxation times. Moreover, with the temperature increase close to the $T_g$, the $\beta$ relaxation wing gradually merges into the $\alpha$ relaxation peak, manifesting the connection between the two types of dynamic behaviors. From an energy point of view, the two different relaxation modes can be represented by two kinds of hopping event in the potential energy landscapes as shown in Fig. 1.9. The $\beta$ relaxation corresponds to small scale hooping events between neighboring energy minima, while $\alpha$ relaxation can move the configurations from one megabasin to another [48, 56].

Research indicates that $\beta$ relaxation has a close correlation with other dynamic processes

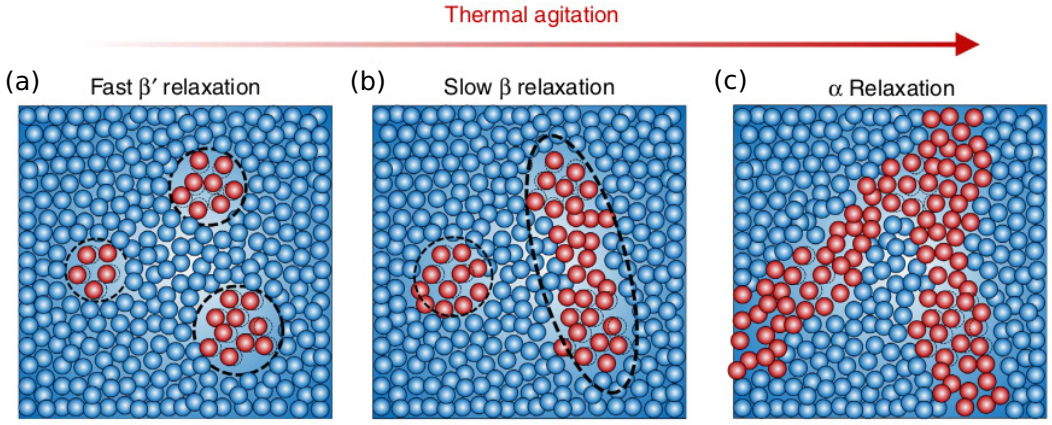


**Figure 1.7:** The illustrated mechanisms of relaxations in MG. (a) and (b): The $\beta$ relaxation is associated with the local structural rearrangements. (c): The $\alpha$ relaxation is associated with the percolation of the local relaxations through the entire system [57].

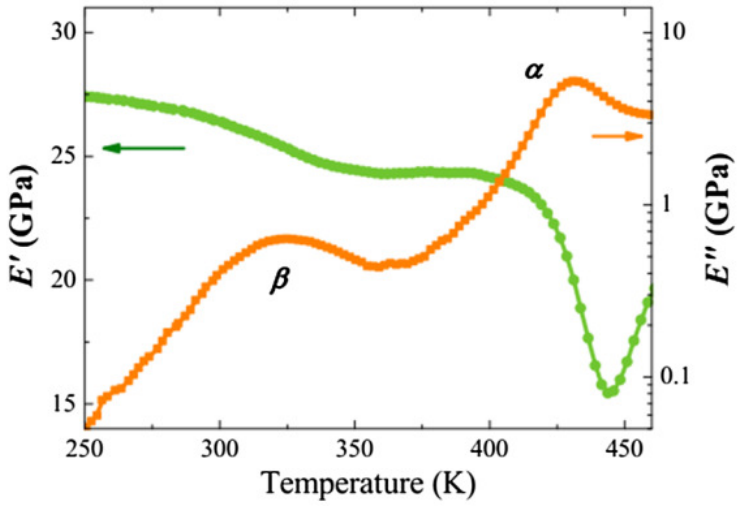


**Figure 1.8:** The isochronal dynamical mechanical spectrum of relaxation behavior for the La-based MG system [47].

in MGs that make the study of $\beta$ relaxation a vital route to understanding the structural and mechanical characteristics of MGs [59–63]. The relaxation process and characteristics are highly affected by the structural nature of the glass materials and one of the most essential factors is the chemical composition. After systematically studying of relaxation behavior of various MG systems, Yu et al. [64] pronounced that $\beta$ relaxation is associated with regions where all the atomic pairs have large similar negative values of mixing enthalpy. Additionally, the effect of atomic pairs on the relaxation behavior is not only determined by their atomic properties, but also depends on their specific chemical environments and interactions with other atoms [48, 64]. The cooling process of the glass material, as well as the aging history, also plays an essential role in the relaxation dynamics. For example, slow quenching can make the glass more stable than the fast quenched system hence reducing the intensity of $\beta$ relaxation in MGs, however,

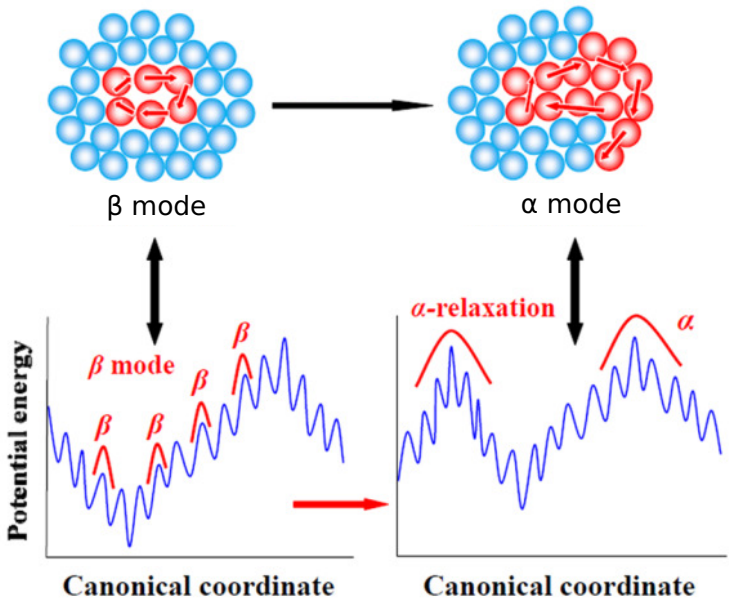


**Figure 1.9:** Two relaxation modes correspond to potential energy landscapes. The $\beta$ relaxation represents local atomic motion while $\alpha$ relaxation incorporates large-scale atomic migration. As illustrated in the potential energy landscapes, the $\beta$ mode relaxation is the stochastically activated hopping events across sub-basins and the $\alpha$ relaxation is large scale hopping events extending across megabasins [47].

it can never totally suppress the relaxation [48, 65]. The mystery of $\beta$ relaxation has not been totally determined, nevertheless, studies have identified its basic mechanism and its correlation with the $\alpha$ relaxation. In general, the $\beta$ relaxation is an inhomogeneous local atomic motion in the glassy matrix. The length scale of the motion could only be located in the regions containing approximately 200 atoms [66, 67] and no evidence shows that all the atoms will participate in the $\beta$ relaxation behavior.

Further studies investigated that the $\beta$ relaxation event has similar activation energy as the basic shear unit in MG's deformation, i.e. shear transformation zone (STZ). Furthermore, the length scale of the STZ in MGs is also proven to be close to tens or hundreds of atoms. The insight that $\beta$ relaxation shows the same nature as the STZ in MG systems brings a straightforward idea that the deformation mechanism of MG can be affected by the control of the $\beta$ relaxation. The modulation of $\beta$ relaxation can tailor the structural inhomogeneities of the glass system then tune the macroscopic plastic flow and enhance the ductility of MGs [47]. Generally, the $\beta$ relaxation can be modulated by designing the compositions of MGs, by modulating the cooling history of the glassy and applying non-affine strain to the sample [60, 68–70]. The La-based MGs with well-designed addition of Al and Ni elements can tune the activation energy of $\beta$ relaxation that can be manifested by the strong and wide wing of relaxation peak at low-temperature (Fig. 1.10 left panel). Compared to the traditional MG system, the flow

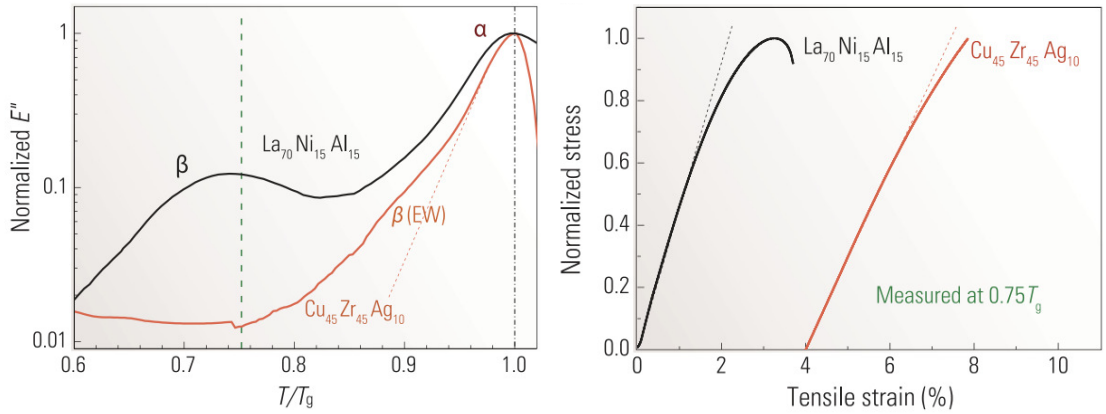


**Figure 1.10:** Comparative studies between a La MG and a CuZr MG (a) DMA spectra and (b) tensile stress–strain curves, redrawn from [47].

units in La-based MG can be activated at room temperature, therefore, exhibits a better tensile plasticity begins to appear (Fig. 1.10 right panel). Fast cooling and non-affine strain enable the MG system to exist in a higher energy state that allows the activation of more flow units and a pronounced $\beta$ relaxation behavior. Hence, contrary to the highly localized shear deformation mode in the extremely slow cooled glass, the fast quenched glasses are prone to show a more homogeneous deformation process. More intriguingly, the mechanism of $\beta$ relaxation is highly correlated to the glass forming process, and a linear relationship between the activation energy of $\beta$ relaxation $E_b$ and $T_g$ is described as $E_b \approx 26RT_g$ where R is gas constant [66]. This evokes people that the mechanical properties of MGs can also be tailored by controlling $T_g$ and an effective way is to systematically design the constituent elements of MG systems [71, 72].

Beyond the significantly primary $\alpha$ and secondary $\beta$ relaxation process, the third relaxation mode defined as $\gamma$ relaxation comes into the researcher's eyes since very recently. The $\gamma$ relaxation appears as a very low temperature relaxation mechanism ($0.26\,T_g - 0.29\,T_g$) and was first detected in the cooling process of ZrCu-based MGs [58]. Analogous to other relaxations, the $\gamma$ relaxation can be represented by the extra small peak in the dynamic mechanism spectrum (Fig 1.11). The activation energy for $\gamma$ relaxation is distinctly lower than $\beta$ relaxation and it can be seen as the fast structural transition process during the glass formation process. Further study indicates that the $\gamma$ relaxation is a non-affine atomic rearrangement that arises by the atomic-level thermal stress generated during cooling [58]. However, due to the lack of detailed study of this new relaxation mode, its atomic-level structure and mechanism is still unclear and further analysis must be done to make a systematic picture of it.

The study of the remarkable nature of different kinds of relaxation behaviors opened a new

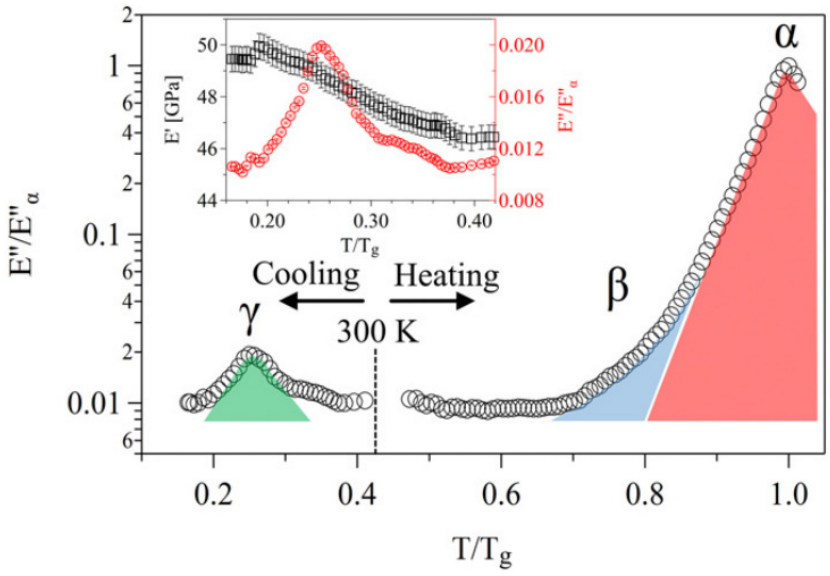


**Figure 1.11:** The relaxation spectrum of ZrCuNiAlNb MG sample. Besides the $\alpha$ and $\beta$ relaxation peaks, a small extra wing appears in the low temperature region, indicating the existence $\gamma$ relaxation behavior [58].

chapter for scientists to reveal the structural and mechanical characteristics of MGs, research has significantly advanced the understanding of a number of important issues [73–76]. However, many critical issues regarding relaxation in MGs remain puzzling and need to be further studied.

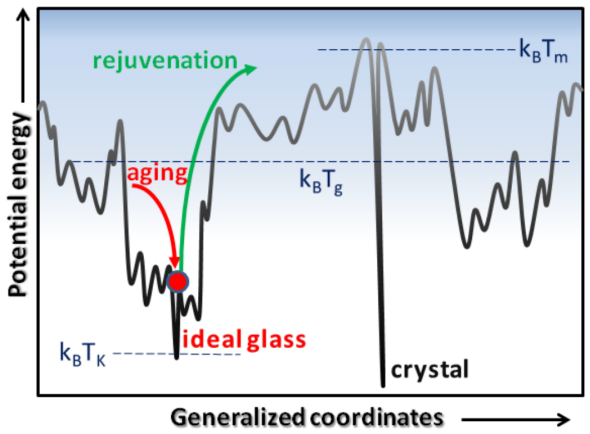


**Figure 1.12:** The schematic of the aging and rejuvenation behavior represented by the potential energy landscapes [77].

## 1.3 Rejuvenation process in metallic glasses

### 1.3.1 Thermally activated rejuvenation

The well relaxed as-cast MGs can undergo an energy increase process with the external energy injection which is called rejuvenation. The rejuvenation process arouses the structure of MGs back to a more liquid-like state, corresponding to the increase of the degree of disorder.

As the inverse process of structural aging, rejuvenation can effectively increase the energy state of the MGs (Fig. 1.12) and usually introduce more free volume and rheological units into the glassy matrix. More importantly, rejuvenation can tune the MGs towards a state that cannot be obtained by traditional rapid cooling methods, providing new insights into the understanding of microstructure and properties nature of amorphous metals.

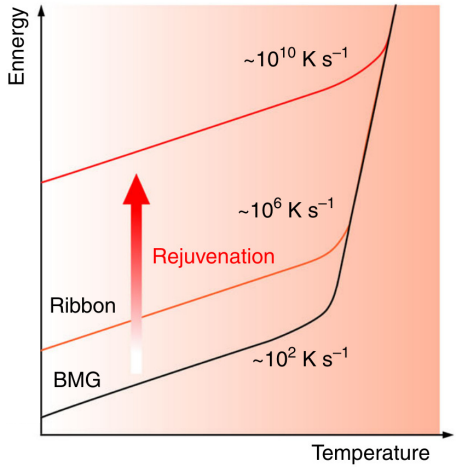


**Figure 1.13:** The relationship between rejuvenation and cooling rate in MGs. A slowly cooling rate results to a make the well-relaxed glass while a fast cooling rate generates a more disordered (rejuvenated) glass [78].

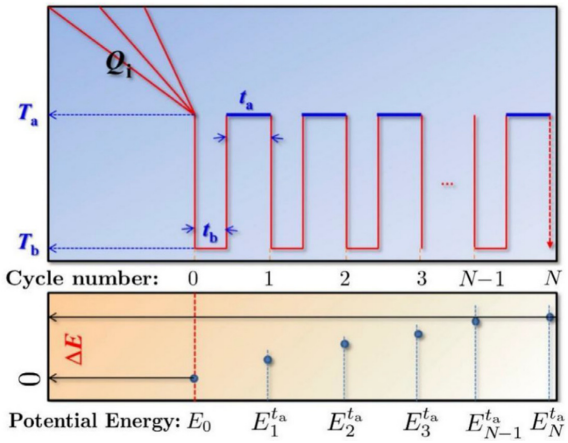


**Figure 1.14:** The potential energy evolution of $Cu_{50}Zr_{50}$ MG sample during the N times thermal cycling. At each cycle, the sample was annealed at $T_a$ = 400 K (0.54 $T_g$) and then quenched and relaxed at $T_b$ = 1 K. After cycling, the potential energy of MG increased by $\Delta$E indicates the rejuvenation [79].

Until now, extensive research has been carried out on the rejuvenation behavior of MGs and many methods that can achieve rejuvenation are proposed. Contrary to the relaxation procedure, an effective way to rejuvenate a glass is to increase its cooling rate during solidification. As shown in Fig. 1.13, in contrast to the well-relaxed glass, that is fabricated by slowly cooling, fast cooling can freeze the glass in a more disordered state with the combination of higher

free volume and high enthalpy. As shown in Fig. 1.14, thermal cycling is another strategy to rejuvenate the MGs and can increase the potential energy of the material [79, 80]. The response of thermal expansion during thermal cycling is highly dependent on the local heterogeneity of the MG's structure, which leads to the inhomogeneous distribution of the local strain and increases the internal energy state of the MGs [80, 81]. The rejuvenation behavior that arose by thermal cycling is also highly related to the initial composition of MGs. For instance, thermal cycling contributes to the apparent rejuvenation in Zr-based amorphous alloy but causes only an inconspicuous rejuvenation in Pd-based system [82]. Furthermore, the rejuvenation degree of low-purity La-based MG is significantly higher than that of the high-purity La-based glassy system [83]. For La-based glassy system [80] it has been found that the rejuvenation is always followed by a relaxation process during cryogenic thermal cycling. Thermal induced rejuvenation result in the change of mechanical properties of glass materials. Ketov at al. [80] demonstrated that thermal-cycling rejuvenation can excite the activation of more flow units in the Zr-based MGs, which turn the highly localized deformation mode into the homogeneous flow and finally increase its plasticity from 1.4% to 5.1%. Rejuvenation shows the potential to improve the plasticities of MGs and now it can be treated as an option to control the mechanical properties of amorphous alloys.

### 1.3.2 Mechanically activated rejuvenation

Deformation is adopted as a rejuvenation method which can induce the generation of a large amount of free volume and significantly store deformation energy into the glassy structure that, finally, increase the energy state of the MG [84]. By applying heavy elastic deformation to 90% of the yield stress, Lee et al. [85] demonstrates that the $Cu_{65}Zr_{35}$ MG can be rejuvenated and result in the increase of enthalpy. Ultrasonic vibration elastically compressed MG presents a more disordered local structure state compared to the as-cast glass materials indicating the rejuvenation behavior, while, the degree of rejuvenation is correlated with the compression level [86].

Besides elastic deformation, rejuvenation can also be detected in the glass that are plastically deformed by high-pressure torsion (HPT), cold-rolling and shot-peening [87–91]. HPT induces in the glass a more loosely packed local structure and injects energy to the glass sample and increases its enthalpy equal to the value of the glass that is fabricated with a ten times faster cooling rate [87]. Heavy plastic deformation such as cold-rolling induces shear bands inside the glass materials, and studies indicate that the shear band areas are the "highly rejuvenated"

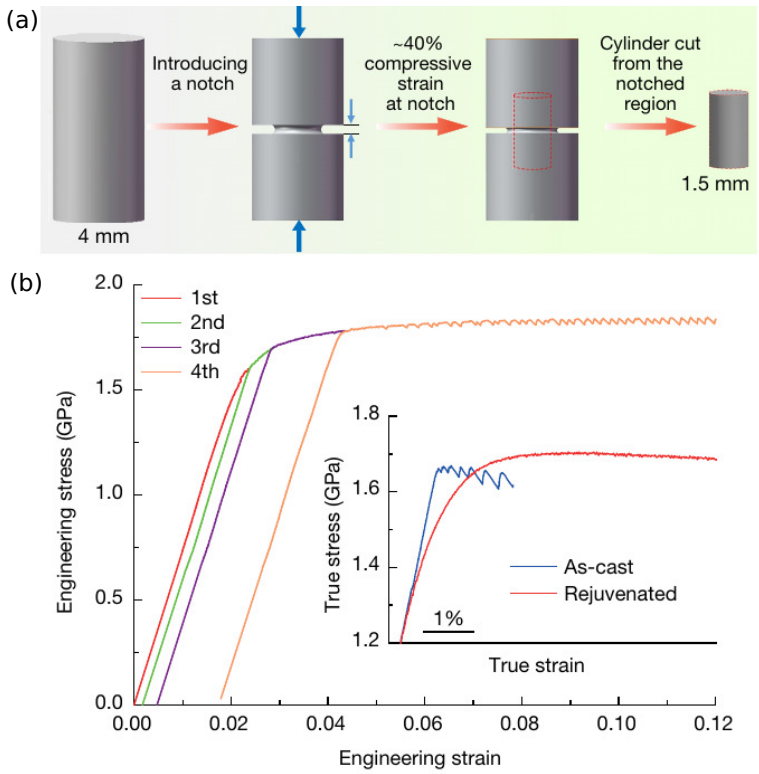


**Figure 1.15:** (a): A Zr-based BMG is machined to have a circumferential notch. The cylinder part that is cutted form the notch region is rejuvenated due to the uniaxial compression. (b): Four engineering stress–strain curves for uniaxial compression, corresponding to three unloading–reloading cycles of one sample rejuvenated as in (a). The rejuvenated glass shows extensive homogeneous flow and strain-hardening [84].

part in the deformed MGs. Compare to the "slightly rejuvenated" glass matrix, the shear bands area contains a large amount of free volume and has high energy. However, the localized shear bands restrict the rejuvenation to these narrow bands that can only occur very inhomogeneous in the deformed MG, which limits the rejuvenation process.

Rejuvenation provides a possible way to excite the glass structure to a more active state and make the material to show better properties, and it also shows potential to overcome the MGs overcome the strain-softening drawback. Pan et al. [84] first reported that plastic deformation under triaxial compression can rejuvenate the notched-BMG sample sufficiently to enable strain-hardening during the cycling loading-unloading tensile test. As shown in Fig. 1.15, by introducing a circle notch around the as-cast MG sample and followed by the uniaxial compressive deformation, the center notched region can be homogeneously rejuvenated. The highly rejuvenated sample cut from the notch region shows strain-hardening during the cycling-loading tensile. They claim that the hardening is raised by the stress-induced structural relaxation of the rejuvenated materials. Nevertheless, one should also take into consideration the residual stress generated during the sample preparation. Even removing the external stresses, after cutting out

the highly rejuvenated region within the notched rod, the residual stress may remain confined in the structure and can be considered as an apparent contribution to the increased strength in materials [92].

Control of the degree of rejuvenation and understanding the nature of rejuvenation dynamics of MGs is remain a hot topic and numerous inspiring works have been published in the past decades. However, there are still some issues to be further explored. Most of the accepted methods, such as thermal cycling, recovery annealing, or heavy plastic deformation, can only locally rejuvenate the MG structures. Hence, a rejuvenation method with low cost and a high degree of rejuvenation, and easy industrial application, is of great significance for the development of MGs. Amorphous alloys in ultra-high-energy states show different atomic-level structures and thermodynamic behaviors. Although MGs can be rejuvenated through various ways and their energy state can be significantly increased, the limits of rejuvenation are still not known and an amorphous alloy with the "highest rejuvenation" state has noThe t been yet produced. Identifying the maximum rejuvenation threshold and determining the structure of the "highly rejuvenation" MGs plays an important role in fully understanding the dynamic behavior of amorphous metals.

The fact that modulating the degree of rejuvenation in MGs can also provide physical means to turn the MG's properties inspired people to think about the correlation between rejuvenation and relaxation. Both rejuvenation and relaxation can describe the structural dynamic behavior of MGs. The correlation between relaxation and rejuvenation plays a significant role in designing the MG materials with specific properties [47].

## 1.4 Deformation mechanism of metallic glasses

### 1.4.1 From atomic excitations to macroscopic plasticity

The structure of amorphous alloys is unlike their crystalline counterparts, lacks long-range order [16, 94], which means that they can show totally different deformation mechanism compared to the crystal materials. In general, MGs show high yield strength during elastic deformation and show strain-softening during the plastic deformation regime followed by catastrophic failure and the formation of highly localized shear bands (SBs) [95]. The lack of room temperature plasticity restricts the application of MGs as the structural and functional materials. Understanding the atomic-level deformation mechanism of MGs was a critical challenge in the past few decades and a large number of mechanistic theories describing the deformation behavior of MGs have been proposed. Among them, Spaepen and Agon proposed the most cited and

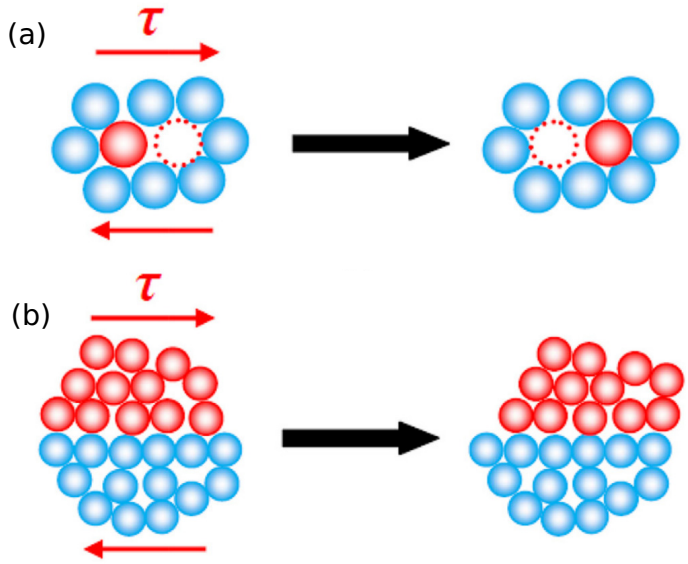


**Figure 1.16:** Schematic of the deformation mechanism of MGs. (a): The "free-volume" model, the plastic flow can occur through a series of atomic jumps. (b): "Shear transformation zone" in which strain accommodation occurs through localized cluster of atoms undergoing intense distortion. Adapted from [93].

instructive theories. Spaepen [96, 97] considered plastic flow on the basis of the "free-volume" model and viewed plastic deformation as a series of local atomic jumps into vacant sites in regions of large free volume (Fig. 1.16 a) [94]. With the increase of the external pressure, the atoms can overcome the activation energy barrier to rearrange around and jump into the near neighbor of high free volume which can accommodate them more readily. Due to the long-range disordered structure characteristics, free volumes and flow events in the glassy matrix are distributed inhomogeneously.

Agon [100] proposed a more detailed way to describe the localized plastic event in MGs and first mentioned shear transformation conception which was finally developed to the STZ theory (Fig. 1.16 b) [42]. An STZ involves a group of atoms with much larger atomic displacements than its surrounding neighbor matrix during the deformation process. Although such a zone may not have readily recognizable boundaries [95]. Nevertheless, one should make clear that unlike dislocations in the crystal metals, STZ can not be treated as structural defects in the glass material but rather transient states whose trigger is highly influenced by local atomic environment [94]. Since STZ is a precursor of SB formation, the structural and dynamical characteristics of the STZ, such as its shape and size, the activation energy for the formation and the correlation with its local structure are of special interest. However, the size scale of the atomic-level shear event determines that the STZ is very diffcult to detect in experiments, hence, computer simulations plays a significant role in the last decades in the study of the mechanism

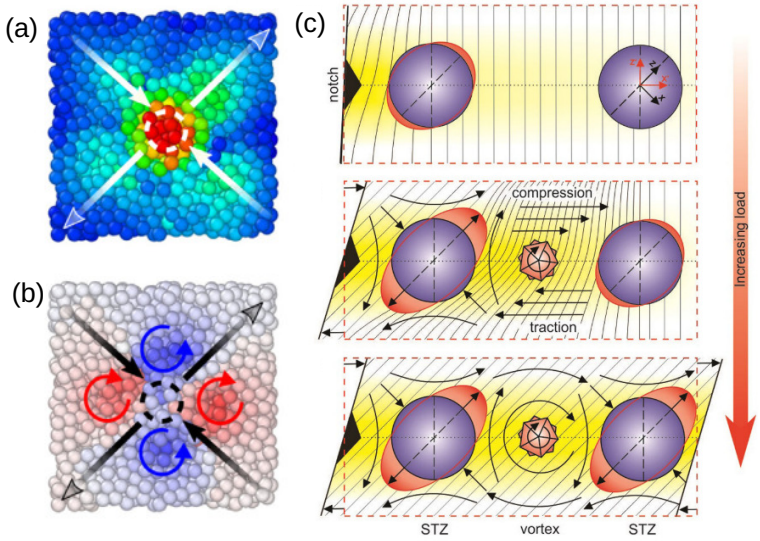


**Figure 1.17:** Schematic of the atomic-level structure of STZ and the generation mechanism of the shear band. (a): The STZ structure revealed by the atomic strain calculation. (b): The sign of the rotation angle around STZ. The atomic strain around the center of the STZ shows a quadrupolar distribution. (c): The activation of STZ can generate a strong antisymmetric stress field, which causes a collective vortexlike motion. This vortex structure already induces the first deformation in the neighboring STZ and after the applied external stress exceeds the threshold value, the neighboring STZ will be activated. The repetition of this two-unit STZ-vortex mechanism leads to STZ percolation along a specific direction and, ultimately, to the formation and propagation of a SB. Adapted from [98] and [99].

of STZ activation and percolation. The size of the STZ varies over a fairly wide range and depends on its original surrounding disordered structure. A study based on the 3D monatomic glass model revealed that the local plastic events typically involve tens of atoms [101]. Furthermore, Zink et al. [102] studied the CuTi binary glass and calculated that the boundary of an STZ can be wider than 1.5 nm which thus contains more than 120 atoms. All in all, STZs may have a diameter of about 1 nm which contains a few tens to a few hundred atoms and it has several tenths of $eV$ activation energy [95].

More statistical studies have been done to fully understand STZ and their roles in the deformation and crack behavior in MGs and, until now, many molecular dynamics simulations have provided useful insights into the correlation between microscopic structural heterogeneity and STZ activation. Simulation works revealed that the effective area of STZ can be expanded to a larger space around the center of the group of atoms and shows a quadrupolar distribution of strain field behaving like Eshelby inclusions [98, 99, 103–105]. Very recently, Şopu et al. firstly highlighted the atomic structure of the STZ and its affected areas based on the build of the STZ Vortex model [98]. Moreover, the STZ-Vortex hypothesis proposed a novel atomic-level mechanism underlying the STZ activation and percolation processes [99] (Fig. 1.17). The atomic strain distributed around STZ center shows a quadrupolar distribution and, meanwhile,

induce the generation of rotation fields that also display a quadrupolar distribution (Fig. 1.17 a). The arrangement of STZ atoms causes a strong antisymmetric stress field in the neighbor resulting in the generation of regions where atoms show circular displacements resembling a vortexlike motion (Fig. 1.17 b). The Vortex structure induced small excitations in the first neighboring STZ and when the applied external stress exceeds the threshold value, the next STZ will be activated (Fig. 1.17 c).

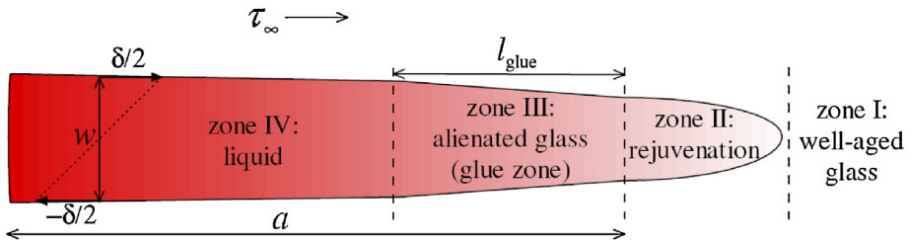


**Figure 1.18:** Aged-rejuvenation-glue-liquid model of SB in BMGs. [95, 106].

### 1.4.2 Shear band formation and propagation

Regarding the SB formation process, three possible hypothesis are most acceptable today. The first hypothesis assumes that the SB is formed by the percolation of homogeneously activated STZs [95]. The STZs will be activated one after another with the applied stress and with a sufficiently large population of STZs percolate along with the maximum stress orientation, a deformation band is generated which is softened and will concentrate subsequent shear strains. This hypothesis illustrates that the SB can form due to structural fluctuations in the amorphous material itself, rather than extrinsic flaws that serve as heterogeneous nucleation sites [107]. Contrary to the first hypothesis, the second theory that are concluded by the experiment work maintains that one of the crucial conditions for the formation of SB is the presence of defects, such as voids and surface irregularities. The casting defects serve as stress concentrators when the material is under external stresses. During loading, the local stress in the defect's region is much higher than the global average which helps the atoms overcome the activation energy barrier and start to rearrange as STZ. The first activated group STZs creates the embryonic SB and with the increase of the external stress, the embryonic SB can grow to the critical size and then propagate and develop into a mature SB. Clearly, this hypothesis defines the SB formation as a heterogeneous nucleation process and divides the SB into four zones in sequence representing well-aged, rejuvenation, glue and liquid regions (Fig. 1.18) [106]. The third hypothesis considers the formation of a SB as two consecutive stages as illustrated in Fig. 1.19. In the first stage, the structural disorder process that is initialed by the activation of STZs will create

a viable rejuvenated band along the maximum stress plane for shearing. This rejuvenated band can propagate at a extremely high speed through the material but only induce limited plastic deformation. The followed synchronized sliding and shear-off occurs along the rejuvenation band causing the glass to experience large plastic strains and finally a SB forms.

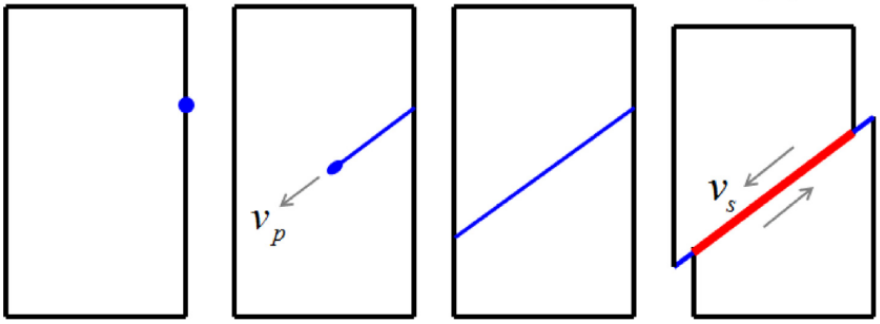


**Figure 1.19:** Schematics showing how a SB forms in a MG under compression test. The first shear usually starts from a stress concentration region, e.g. the surface with a notch. The propagating front reaches the other end of the sample, leaving to the formation of localized band and causes the catastrophic failure of the material. Adapted from [95].

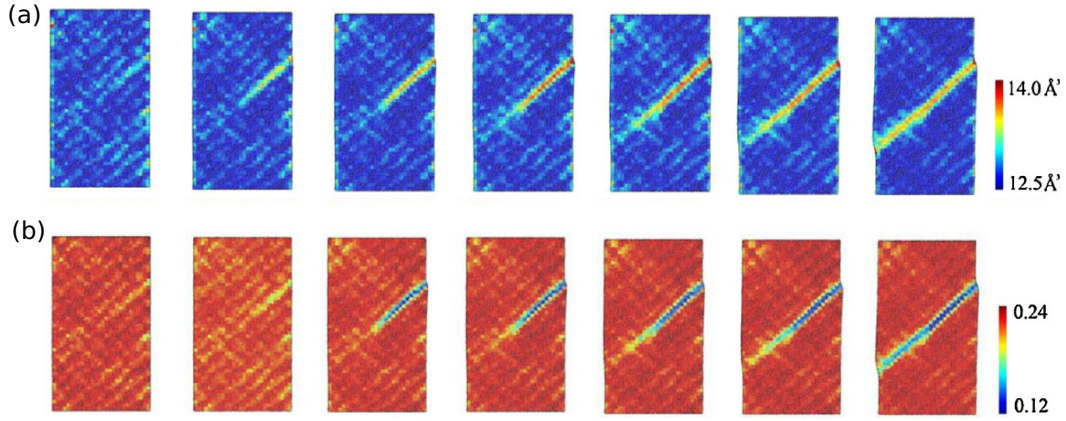


**Figure 1.20:** The evolution of free volume and icosahedral during the formation of SB. (a): The generation of free volume inside the SB area during deformation. (b): The decrease of icosahedral fraction. Adapted form [95, 108].

As the heaviest deformation region in the MG sample, the structure inside the SB are expected to change and show different characteristics compared to the undeformed matrix. The structure inside the SB is diffcult to be investigated in the real-life experiment due to the restriction of its size scale (10-20nm) and fast dynamics. Hence the computer simulation is an ideal tool to reproduce and analyze the structural evolution during SB formation. As shown in Fig. 1.20, simulation studies highlight that the formation of the SB leads to the break of icosahedral clusters along the shear plane, meanwhile, a volumetric increase associated with SB formation

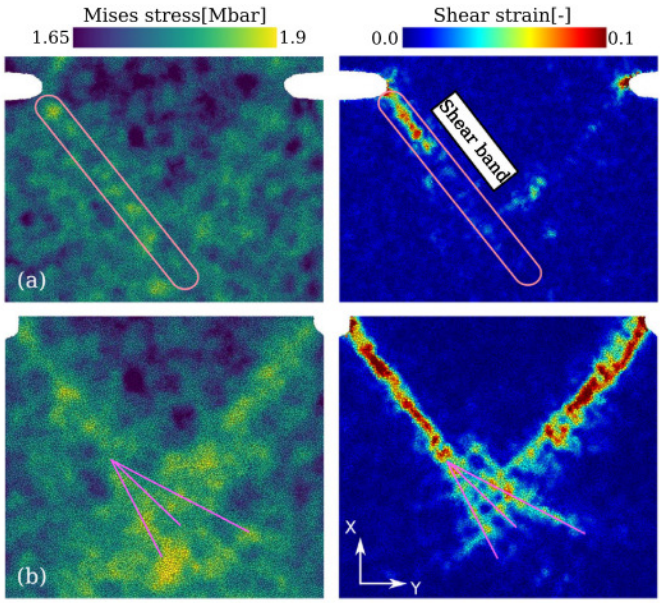


**Figure 1.21:** The evolution of von Mises stress and SB formation in $Cu_{64}Zr_{36}$ with two notches deformed in tension. (a): The stress distribution predicts the generation and propagation of SB. (b): The interaction of two SBs modifies the distribution of the stress, causing shear band branching and multiplication [105].

can be found [108]. Moreover, studies found that both shorter and longer interatomic bonds are created during the generation of SB, suggesting a high degree of disorder. The generated free volumes can be as small as the interstitial sites of dense atomic packing that can also be found in the relaxed glass, indicating that they are associated with intrinsic structural fluctuations in the glassy matrix. In contrast, large size free volume can also generated and can be observed only in deformed glass, implying that they are created during plastic deformation inside the SBs. Beyond the free volumes generation, experiment works revealed the presence of various voids with a scale of around 1 nm inside the SB of ZrTiCuNiAl glass system which indicates the appear of cavitation arising from free volume coalescence [109]. However, subsequent research proves that no nanovoids but only structural disordering can be found in the SB of the uniaxial compressed PdNiP glassy metarial [110]. It seems that the SB dynamics during plastic deformation are highly dependent on the original structure of the glassy system. Additionally, the structure within the SB core is very sensitive to the loading conditions [111].

Similar to the deformation behavior of regular crystal materials, the deformation response and SB formation dynamics in MGs is also sensitively dependent on quite many parameters that can exacerbate the underlying instability, i.e. the sample characteristics and size, the testing environments and conditions. As mentioned above, the generation sites of the SB are usually located in stress concentration areas such as the surface and notches. Moreover, simulation works reveal that the percolation path of SB can be predicted by the stress distribution in the

glassy matrix as shown in Fig. 1.21. Hence it is obvious that the SB nucleation and development can be toiled by the stress distribution in the MG samples. Besides the stress condition, the test conditions are also important factors that influence the SB formation behavior in MGs. The experiments and simulations have revealed that the environmental temperature needs to be considered a vital factor for the SB dynamics cause temperature controls the internal atomic rearrangements kinetics [112]. The deformation mode of MGs can be inhomogeneous and homogeneous depending on the loading temperature. At room temperature, a highly localized SB formation is always expected and with the increasing of temperature, strain localization can be replaced by a more homogeneous plastic flow (Fig. 1.22).

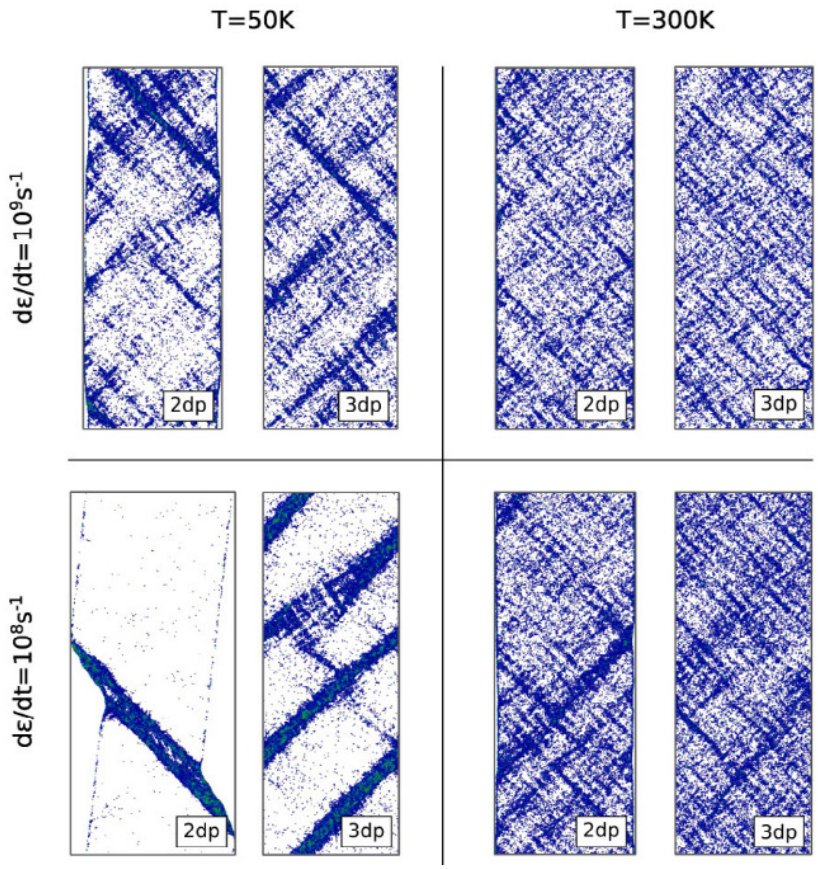


**Figure 1.22:** Schematics of SB morphology under uniaxial tensile deformation at different temperatures and strain rate. The transition from localized SB to homogeneous deformation mode can be found with the increase of temperature and strain rates [113].

In fact, SB is a double-edged sword for the mechanical properties of MGs. Highly localized SB formation will result in catastrophic failure while on the other hand, the interaction of multiple SBs can delay the fracture of material, and in the end, enhance the plasticity. The SB propagation process can be affected by both structural modification and stress modulating. For structural modification, changing the cooling rate during solidification will be the first method

to be taken into consideration. A higher cooling rate does increase the fraction of free volume inside the glassy matrix, which gives rise to the formation of multiple SBs during deformation. The cold-working is seen as a possible way to induce the structural inhomogeneity on a wide range of length-scale in MGs [95], which can modify the SB propagation path and introduce more sites for the generation of multiple SBs. The stress modulation is likely to induce residual stresses that may have an influence on the SBs formation process and delay the generation and propagation of SBs, resulting in the excellent plasticity [114–116].

Numerous experiments and simulations have advanced our understanding of SB dynamics in MG systems. The mystery of SB structural characteristics and formation process is gradually revealed, even so, many critical issues remain puzzling. Nevertheless, better characterization would lead to a better understanding and control of SBs, that in the end, will provide improved mechanical properties for MGs.

# 2 Motivation and objectives

Despite their excellent properties, the future application of MGs is still, to a great extent, highly dependent on understanding the atomic-level deformation mechanism and improving their plasticity. Thus, analyzing the strain localization and, at the atomic level, the activation and percolation of STZ remains a major ongoing issue. Significant plasticity has been reported during high temperatures deformation tests, for high strain rate loading conditions as well as MGs fabricated with higher cooling rates. The atomic-level mechanism behind the observed brittle-to-ductile transition is, however, not well understood and more research is needed to ascertain the relationship between STZ dynamics and the macroscopic flow behavior. Hence, the first part work is to couple temperature, cooling rate, and applied strain rate effects to the deformation behavior of MGs and provide insights into the correlation between the atomic-scale mechanism of STZ activation and percolation and the macroscopic deformation process. To do this, the $Cu_{64}Zr_{36}$ MG system was selected as the object system and use MD simulations to provide a systematic investigation of the brittle-to-ductile transition during tensile deformation. A quantitative analysis of the impact of intrinsic and extrinsic factors on the strain localization process is provided. Moreover, this thesis work aims to disclose the characteristics of the brittle-to-ductile transition with increasing temperature by analyzing the kinetic energy per atom. The effect of the cooling rate and, basically, the effect of thermal history on structural fluctuations will be quantified by sampling the activation energy barrier of local atomic rearrangements. Finally, the observed improved ductility during high strain rate deformation will be elucidated by calculating the sign of the rotation angle.

Structural rejuvenation and relaxation of MGs not only provides fundamental insights into their dynamic behavior but also extends their practical applications and hence, captured increasing attention. One beneficial effect of rejuvenation is on the mechanical properties and previous researches have shown that rejuvenation is an effective way to improve the plasticity of MGs. Moreover, it has been shown that rejuvenation can be followed by a relaxation process [80] indicating a correlation between rejuvenation and relaxation. Although many strategies have been successfully applied to rejuvenate the glass material, the critical factor that determines the degree of rejuvenation and the fabrication of "highly rejuvenated" glasses is still a challenging task, restricted to the understanding of the atomistic mechanism by which MGs can be systematically rejuvenated. In the second part of my work, by choosing the $Cu_{64}Zr_{36}$ and $Pd_{35}Si_{65}$ glassy systems as the prototype material, the degree of rejuvenation in MGs is systematically

controled a "highly rejuvenated" MG system is designed. The systematic atomic-level analysis of the key factors that determine the degree of rejuvenation in MGs will be provided and the structural nature of the "highly rejuvenated" MG will be analysed.

Over the years, many investigations have been conducted on the relationship between rejuvenation and deformation behavior in MGs. Research revealed that rejuvenation can induce strain-hardening in MGs under special loading conditions [84]. However, a systematic understanding of how the degree of rejuvenation affects the deformation behavior of MGs is missing and additionally, the correlation between structural rejuvenation and strain-hardening behavior needs to be further studied. Inspired by this, the third part of this thesis aims to extend the second part of the work and mostly focuses on the "rejuvenation" induced strain-hardening behavior in MGs. the strain-hardening of the rejuvenated MGs actually comes from the stress-induced structure and residual stress relaxation behavior. The strain-hardening in the deformation of the rejuvenated sample is systematically investigated to expose the correlation between strain-hardening and rejuvenation/relaxation.

The strain-softening during plastic deformation has precluded the extensive use of metallic MGs in many fields. Up to date, many strategies have been proposed to design MG materials with enhanced plasticity, however, studies about how to make MGs that show strain-hardening are still rare and this topic deserves futher study. It has been proven that residual stress is one of the critical factors for strain-hardening in traditional glass materials. Inspired by this, this thesis turns the focus to the modification of stress state in MGs and aim to achieve strain-hardening by inducing residual stress. Therefore, in the fourth part work, the stress modulation will be applied to the $Cu_{64}Zr_{36}$ MG systems, and the samples with various residual stress states will be fabricated and tested. The work aims to clarify the reason for the origins of strain-hardening in MGs as one of the most debated aspects of the last decades that in the end, can extend the potential application of MGs as structural and functional materials.

# 3 Methodological and theory

## 3.1 Molecular dynamics simulations

### 3.1.1 Basic approach

Molecular dynamics (MD) is the method that can simulate the time-dependent behavior of particles and then generate atomic positions and velocities. One of the essential elements for classical MD simulation is the interaction potential, from which the interatomic forces for the particles in the simulated system can be calculated. The dynamics of the particles can then be described by the Newton's equation of motion,

$$F_i = m_i a_i, (i = 1, 2, ...n), \tag{1}$$

where $m_i$ is the mass of the atom *i*, $a_i$ is the acceleration and $F_i$ represent the forces acting on the atom *i* due to its interaction with other atoms. For the multiple atoms system (n $\gg$ 3), it is imposible to analytically solve the equation. Hence in MD simulation, the force for each atom is regarded as a constant value during an extremely small time steps $\mathrm{d}t$ (on the order of femtoseconds) and can be treated as the negative gradient of the potential energy *V* which is:

$$F_i = m_i a_i = -\nabla_i V = -\mathrm{d}E/\mathrm{d}r_i, (i = 1, 2, ...n). \tag{2}$$

Then the velocities *v* of the atom *i* are calculated from $a_i$

$$v_i(t + \mathrm{d}t) = v_i(t) + a_i \mathrm{d}t, (i = 1, 2, ...n). \tag{3}$$

Finally, the positions *r* of can be got from velocities

$$r_i(t + \mathrm{d}t) = r_i(t) + v_i \mathrm{d}t, (i = 1, 2, ...n). \tag{4}$$

In short, the new positions and velocities in the next step can be determined by the forces acting on the atoms combined with the current positions and velocities. After the atoms are moved to the new positions, the new forces and velocities information are computed and these dynamic cycles will be repeated as long as the simulation need. The equation of motion determines that the MD is a deterministic technique, which means the subsequent time evolution is completely determined by the current atomic positions and velocities. Moreover, the dynamic process has time-reversal symmetry and the microscopic physics is independent of the direction of the time flow [117].

MD simulations have the power to describe the microscopic properties of atoms. Based on the Gibbs ensemble concept, one can predict the macroscopic properties of a very large system by simply averaging over a large number of tiny identical systems with each of them in individual microscopic configurations. In short, the macroscopic observables of a system are

formulated in terms of ensemble averages [117]. The statistical ensembles commonly accepted in MD simulations are characterized by constantly fixed values of thermodynamic parameters; such as the isothermal-isobaric ensemble (NPT) with constant particle number N, constant pressure P and constant temperature T.

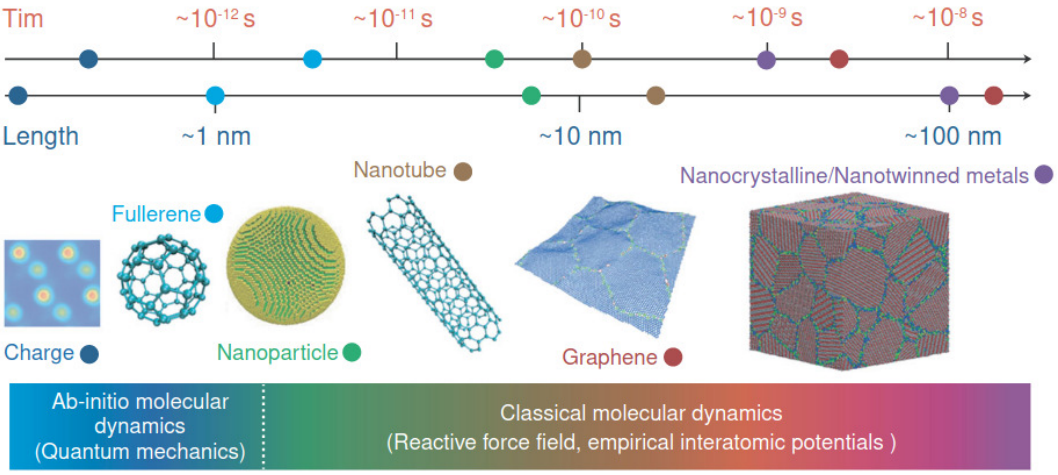


**Figure 3.1:** A schematic illustration time-scale and length-scale of Ab-initio and classical MD simulations. Some typical nanostructured materials that are corresponded to the time/length scale are shown as illustrative examples [118].

The MD simulations provide possibilities for the determination of microscopic properties of atoms, however, there are still has many limitations and their application is often limited by the computational power. The simulation's time duration is dependent on the time-step between each dynamic cycles hence the time-step must be well designed. In principle, the time-step should be small enough so that the discretization errors can be avoided, and moreover, the sum of time-steps must be large enough to capture the effect being modeled without taking an extraordinary period of time, i.e. smaller than the vibrational frequency of the system [117]. Therefore, the time scale for classical MD simulations is often limited from picoseconds to several hundreds of microseconds. The time scale limitation of MD simulations also reflects on the works of this thesis. For instance, compared to the cooling rates in real life experiment, much higher values have to be adopted during the fabrication of MG systems in MD simulations. Moreover, during the deformation simulations, extremely high strain rates, that are several order of magnitude higher than in the experiment,are usually applied to the system so that the thermally activated processes are not possible to be captured. That is why the yield stress is much higher than the values found in experiments.

Apart from time scale limitation, the length scale is also an unignorable limitation for MD simulations. The size of the simulated model was limited by the available storage of the

computational system and also by the processor speed. In the past, only samples not bigger than thousands of atoms have been used for MD simulations- With the dramatic development of computer technology, the sample size can go nowdays to hundreds of millions of atoms (Fig. 3.1). An effective strategy to ameliorate the length scale problem is the application of periodic boundary conditions (PBC) during simulation. PBC can make the atoms on one side of the model interact with atoms on the opposite side and are useful for simulating bulk systems [119].

Despite the above limitations, MD simulations is a helpful method that links microscopic behavior to macroscopic properties through statistical mechanics when studying nanostructured materials. Furthermore, MD simulations are proven to describe the properties and topologies of many matters in precise, especially the amorphous materials such as MGs and nanoglasses [120–122]. In this thesis, all of the glass formation processes and deformation mechanisms of the MG systems are investigated using classical MD simulations by using the Large-scale Atomic/Molecular Massively Parallel Simulator (LAMMPS).

### 3.1.2 Interatomic potential

One of the indispensable parts of the MD simulations is the potential for the system which defines the interactions between atoms within a cutoff distance. The potentials that are chosen in the works of this thesis are embedded-atom method (EAM) potentials and Tersoff potential. The EAM potential is used to compute the pairwise interactions of metal alloys in MD simulations. As described by the EAM potential, the total energy $E_i$ of an atom can be written as

$$E_i = F_\alpha \left( \sum_{i \neq j} \rho_\beta \left( r_{ij} \right) \right) + \frac{1}{2} \sum_{i \neq j} \phi_{\alpha\beta} \left( r_{ij} \right) \tag{5}$$

where $\alpha$ and $\beta$ means the types of atoms *i* and its surrounding neighbor atoms *i* respectively. *F* in the first term represents the embedding energy that is induced by the atomic electron density $\rho$ at the position of atom *i*, while the second term shows the pair potential interaction of atom *i* and *j*.

Compare to the EMA potential, the Tersoff potentials are based on the bond order concept and usually chosen to describe the atomic interaction of covalent materials. The strength of a bond between two atoms depends on their local environment and is not constant. Briefly, the energy of atoms in the system can be calculated as

$$E = \frac{1}{2} \sum_i \sum_{j \neq i} V_{ij} \tag{6}$$

where $V_{ij}$ is the bonding energy and can be described as

$$V_{ij} = f_C \left( r_{ij} + \delta \right) \left[ f_R \left( r_{ij} + \delta \right) + b_{ij} f_A \left( r_{ij} + \delta \right) \right] \tag{7}$$

here, the $r_{ij}$ is the distance between the atom *i* and *j*, $\delta$ is the optional negative shift of the equilibrium bond length, $f_A$ is the attractive pair potnetial and $f_R$ represents the repulsive pair potential, and $f_C$ is a cut-off radius function which the formular is

$$f_C(r) = \begin{cases} 1 & r < R - D \\ \frac{1}{2} - \frac{1}{2}\sin\left(\frac{\pi}{2}\frac{r-R}{D}\right) & R - D < r < R + D \\ 0 & r > R + D \end{cases} \tag{8}$$

with the cutoff distance (*R* + *D*).

In the works of this thesis, the Mendelev's EAM potentials [123, 124] are used to investigate the glass formation and deformation process of the CuZr MG systems while the Tersoff's potential [125] only chosen to study the dynamic behavior Si atom in PdSi metal-metalloid alloy.

### 3.1.3 Simulating the deformation mechanism

The simulation of the deformation mechanism of MGs starts with the fabrication of glass systems with different sizes and cooling rates. Basically, the MGs system was produced by quenching the initial equilibrium liquids system from 2000 K to 50 K with extremely fast cooling rates ($10^{10}$ K/s $-$ $10^{12}$ K/s). The strain-controlled uniaxial tensile tests with different loading rates ($4\times10^{7}$/s $-$ $10^{9}$/s) were applied to the MGs to continuously stretch the samples until heavy plastic deformation with the formation of SBs. The kinetic energy, potential energy, stress tensor, and strain tensor were monitored during the whole deformation process and were analyzed and visualization by Open Visualization Tool (OVITO) [126].

The deformation mechanism was described by calculating the atomic-level strain which was accomplished in OVITO based on the comparison of the initial principle configuration with the deformed atoms' positions. The atom displacement vectors were calculated from the initial and the deformed models and the deformation gradient tensor *F* can be defined. The atomic strain tensor for each atom can then be derived by $E = 1/2(F^T F - I)$ and the von Mises local shear invariant and the hydrostatic strain strain is measured. A parameter used to describe the deformation mode of different MG samples is the degree of strain localization $\psi$ which is defined by Cheng et al. [127] as:

$$\psi = \sqrt{\frac{1}{N}\sum_{i=1}^{N}(\eta_i^{\text{Mises}} - \eta_{\text{ave}}^{\text{Mises}})^2}, \tag{9}$$

and $\eta_i^{Mises}$ represents the von Mises strain of the object atom and $\eta_{ave}^{Mises}$ is the average von Mises stress of all atoms. $\psi$ can be used to differ the shear mode and a large $\psi$ means highly localized deformation such SBs formation.

## 3.2 Activation–relaxation technique

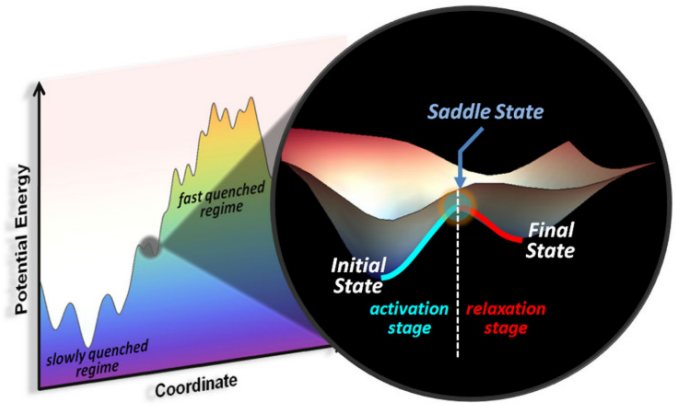


**Figure 3.2:** A schematic of the PEL and an atomic activation process from the perspective of the PEL [128].

The potential energy landscape (PEL) surface is a mapping of all possible states that the system can have and it can be used to describe the atomic-scale structure evolution direction of the given system. The description of the system's PEL gives a way to provide all possible events that may occur. Therefore, determination the energy map of the system by analyzing PEL will lead to a thorough understanding of the kinetic dynamics behavior of structural evolution of materials [129]. In general, the atomic rearrangement event can be represented by the evolution between the initial state, the saddle state, and the final state in the PEL, and the potential energy difference between the initial and saddle is defined as the activation energy barrier (see Fig. 3.2). Atoms and clusters can overcome the activation energy barrier by gaining energies from the applied input and move from the initial energy minimization state to a new adjacent minimum.

In this thesis, the activation energy histogram of the CuZr MG systems activated with different cooling rates will be described by the activation-relaxation technique (ART) with the help of ART nouveau. The ART nouveau is an open-ended saddle point search algorithm package that calculates the energy evoluation during the activation-relaxation process. Generally, an event during the activation-relaxation process can be proceeded into three steps [130]:

(I) Leaving the initial state. In order to reduce the computational cost, a region instead of the entire configuration will be selected as the object. The atoms in the object region were situated in the local energy minimum and a random perturbation will be applied to deform it in order to identify a direction of activation.

(II) Convergence to a saddle point. After the activation direction is identified, the system will be pushed slightly along this direction and atoms will be activated to leave the initial energy

minimization and, if successfully, atoms will reach their first-order saddle point in the PEL.
(III) Relaxation into a adjacent minimum. After the second step, the system will be in the transition state and situated in the first-order saddle point. Then, the system is generally pushed in the direction away from the initial minimum and moves nearly a distance of 0.15 times the distance between the saddle and the initial point. After that, the system will be pushed to a new local minima with the application of energy minimization.

# 4 Summary of the publications

Before the finalization of this thesis, four papers have been published based on the objective of this work. All of the publications are included in the second part of the thesis and a brief summary is provided below.

## 4.1 The brittle-to-ductile transition in metallic glasses

In order to give a systematic investigation on the brittle-to-ductile transition during tensile deformation, the effects of cooling rate, temperature, and strain rate on the tensile deformation behavior of $Cu_{64}Zr_{36}$ MGs have been investigated and discussed in the **Publication I**. In conclusion, an improved ductility can be induced to MG systems by increasing the cooling rate, the testing temperature and the strain rate.

The atomic structure of MGs is determined by the cooling history and high cooling rate leads to a higher degree of disorder corresponding to a low density of close packed Cu-centered full icosahedra (FI). The FI cluster exhibits a high packing density, high shear resistance, and low local atomic mobility, hence, the sample prepared with a high cooling rate contains lower average activation energy compared to the one prepared with a much lower cooling rate. Therefore, local atomic rearrangements events will be more likely in the fast quenched sample, and STZ events can be activated at lower stresses.

By increasing the loading temperature from 50 K to 300 K ($\approx 0.38T_g$), the deformation mechanism changes from one single dominant SB to multiple SBs formation. At high temperatures, although the local structure does not suffer important variations, the increase in the kinetic energy allows the atoms to easily overcome the activation energy barriers for rearrangement and hence, raises the probability for thermal activation of STZs. However, it has to be mentioned that the structures obtained in MD simulations are not well-relaxed as those quenched in experiments at cooling rates order of magnitudes lower. Hence, the roughness of the potential energy surface is higher in experimental samples and consequently, the brittle-to-ductile transition takes place at temperatures much higher than those found in simulations.

Approved by the simulations, by deforming the MGs at an extremely high strain rate, better plasticity can be found compared to the slower loading. In the fast loading condition, a large amount of energy is stored in a short time in the glassy matrix, resulting in the activation of numerous STZ events when yielding starts. The competing interaction of the homogeneous network of STZs restricts the formation of one dominate SB (Fig. 4.1). Therefore, instead of

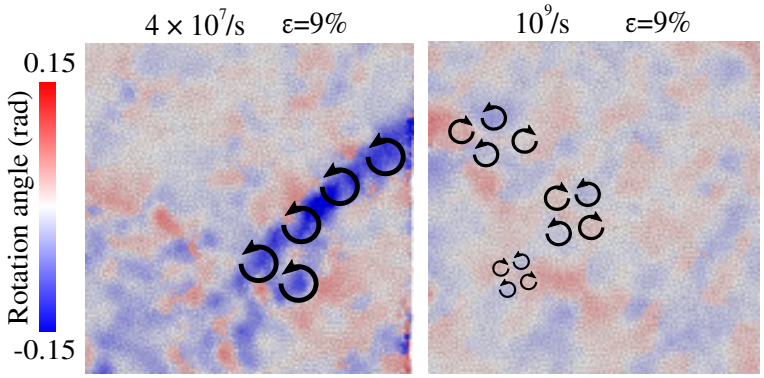


**Figure 4.1:** Atomic deformation mechanism resolved by the STZ-rotation unit. As shown in the left panel, during low strain rate loading, the first STZ activate close to the surface of the sample, while the connected rotation field activates the next STZ. As represented by the right panel, during the high strain rate loading, many STZs with low atomic shear strain can be activated simultaneously and interact with each other through the rotation fields. Vortices of different rotation directions (clockwise and counter-clockwise rotations represented by red and blue colors, respectively) hinder STZ percolation and prevent formation of a dominant SB.

theformation of a single SB, a homogeneous deformation can be found in the extremely fast deformation. However, one should mention that in experiments, a brittle-to-ductile transition is usually observed with decreasing the strain rate and uniform elongation of a MG nanowire was observed at a low strain rates. The difference between the strain rates used in these experiments and in MD simulations is ten orders of magnitude. At such a low strain rate, thermally activated driven processes induced structural relaxation that compensate for structural rejuvenation, i.e., STZ activation. Hence, the balance between the two processes (STZs activation $vs$ local $\beta$-relaxation process) delays the onset of catastrophic shear. In the MD time scale, the thermally activated relaxation (diffusional atomic rearrangement) is suppressed, while the number of STZs (the degree of rejuvenation) increases with the applied strain rate.

## 4.2 The structure rejuvenation in metallic glasses

The monolithic $Cu_{64}Zr_{36}$ MG with the different degrees of rejuvenation was designed and further investigated, the relaxation transition process from localized $\beta$ to homogeneously $\alpha$ can be founded. The detailed discussion is shown in the **Publication II**. In summary, a dilution procedure was applied to the MG systems by randomly removing atoms, one by one, from the glassy matrix. In this way, vacancies creation allows to generate free volume and disrupt the structure of the glass and pushs the system to a more disordered state and, consequently, systematically rejuvenate the MGs.

The degree of rejuvenation was represented by the fraction of free volumes inside the system and four stages of rejuvenation have been identified and as shown in Fig. 4.2: (I) At the

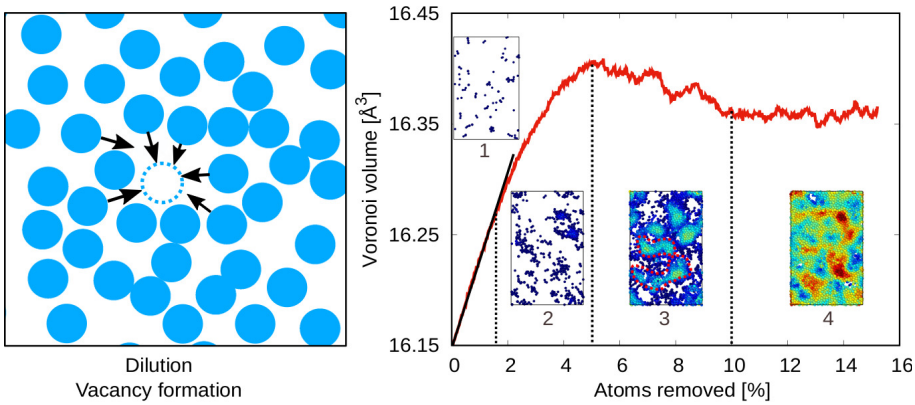


**Figure 4.2:** The left panel indicates the schematic of the one-step dilution procedure. One atom was removed from the glassy matrix and free volume was generated, which induced the activation of its surrounding atoms. The right panel represents the free volume evolution during the dilution process and the inset shows the atomic displacement during the four stages of dilution.

begining of dilution process, the linear increase in free volume correlates to individual vacancy formation and illustrates a homogeneous rejuvenating process. At this stage, individual vacancies are created and only a few neighboring atoms are activated trying to close the vacancy while most of the free volume remains localized into the matrix. The free volume generation is much faster than its annihilation through vacancy squeezing, rejuvenation is the dominant dynamic behavior.

(II) After 2% of atoms were removed, vacancies precipitates and clusters of atoms of high displacement start forming that could correlate to the initiation of $\beta$ relaxation.

(III) When enough free spaces were induced into the glassy matrix, the clusters grow during dilution and string-like atomic rearrangement takes place as a result of the linkage of many highly localized rearrangements, which contributes to the deceleration of the $\beta$ relaxation and the transition to $\alpha$ relaxation. At this point, the dynamic behavior of the system changes from rejuvenation domination to a complex rejuvenation-relaxation competing mode.

(IV) Finally, with further dilution, the local atomic hops develop into a long-range chain reaction, resulting in the dominant $\alpha$ relaxation behavior when the atomic rearrangement can not be restricted locally anymore. The spatially homogeneous relaxation corresponds to the presence of “mobile” atoms in the glass matrix. Hence, although atoms are still removed from the sample (free volume continue to be generated), the “mobile" atoms will fill the vacancy place immediately that leads, in the end, to the dynamic balance between free volume creation and annihilation.

During the final stage of dilution, a steady fluctuation in the free volume illustrates that no more free volume can be injected into the sample and the glassy structure can not be further

rejuvenated. Based on the results, one may reasonably assume that the MGs can not be rejuvenated unlimitedly and the threshold for rejuvenation can be found. Further studies proves that the degree of excess free volume in the MG material correlates to the yield flow of the material. Moreover, the atomic level structure and the density of SBs show similar values as found in the final stage of dilution. Basically, the structure of a SB can be seen as the "highest rejuvenated" state.

## 4.3 Strain-hardening in rejuvenated metallic glasses

As the extension work of Publication II, **Publication III** is mostly focusing on giving a systematic understanding of the relationship between the degree of rejuvenation and deformation behavior in MGs. Furthermore, it aims to further study the correlation between structural rejuvenation and the transition from strain-softening to strain-hardening behavior.

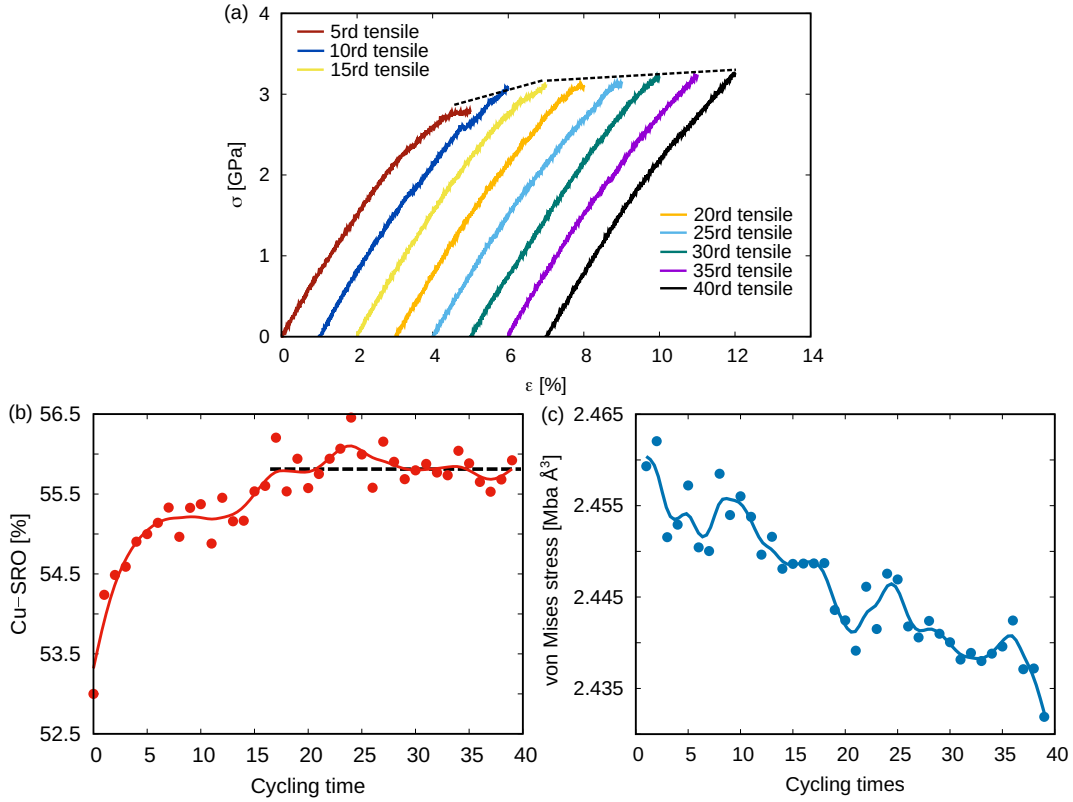


**Figure 4.3:** (a) 40 times strain-hardening in the loading-unloading tensile test for the highly rejuvenated MG sample. Evolution of (b) the fraction of Cu–SRO and (c) the von Mises stress of the system.

Tensile and compressive tests illustrate that with the increase in the degree of rejuvenation, the plasticity of MGs will increase while the strength will decrease. Furthermore, the strain-hardening can be found in the highly rejuvenated MG during the unloaded-reloaded uniaxial tensile test. The highly rejuvenated MG has a higher initial energy state and contains a higher fraction of free volume compared to the as-cast MG. The excess free volume could be released

via a stress-driven relaxation turning to a more stable state that, in the end, causes the observed strain-hardening behavior in the highly rejuvenated MG. Strain-hardening can still be found even after 40 cycles of tensile reloading (Fig. 4.3 a), however, the significant hardening is found from the 1st to the 10th cycles and a slow increase in strength is found from the 15th to 40th cycles indicates two mechanisms. Apart from the high energy state, the highly rejuvenated MG also contains internal residual stresses. At the early stage of cycling loading, stress-induced structural relaxation pushes the system towards a more ordered state and leads to significant strain-hardening behavior (Fig. 4.3 b). After, the structural relaxation becomes sluggish but residual stresses still exist in the glass. Therefore, as the cycling loading continues, the residual stresses are still released during each loading stage slightly lowers the excess free volume and the potential energy of the system and, consequently, increasing the yield stress at the next cycle (Fig. 4.3 c). Although the stress relaxation during the unloading–reloading process continues to increase the strength of the MGs, it is worth noticing that the hardening effect would level off and the rejuvenated MG could not achieve the strength of the as-cast state. Hence, one may reasonably predict that cycling loading can never relax a highly rejuvenated MG back to its initial as-cast state (at least after a reasonable number of cycles).

## 4.4 Strain-hardening in stress modulated metallic glasses

The **Publication IV** provided a stress-modulation strategy that can generate residual stress inside the MG and induce stress heterogeneity and, in the end, make the MG show "real" strain-hardening and extensive ductility.

Different types of two-zone stress-modulated MG systems were designed and the uniaxial tensile tests were applied. **Type 1** contains stress heterogeneity with tensile residual stress in the left side zone while compressive residual stress in the right side, moreover, the absolute stress magnitude are same hence the overall residual stress is zero. The tensile test illustrates that the **Type 1** heterostructure can only show better plasticity without strain-hardening when compared to the as-cast MG. In the **Type 2** MG, the tensile residual stress (T region) in the left zone is much lower than the compressive residual stress in the right part (C region) and, therefore, the **Type 2** sample includes both stress-heterogeneity plus overall compressive residual stress (Fig. 4.4). As shown in the Fig. 4.4 b, the homogeneously distributed entropy in **Type 2** sample illustrates no structure heterogeneity in the system. Surprisingly, as shown in Fig. 4.4 a, tensile tests prove that the **Type 2** system has excellent plasticity, moreover, the yield stress can increase with the applied strain which indicating a “real” strain-hardening behavior.

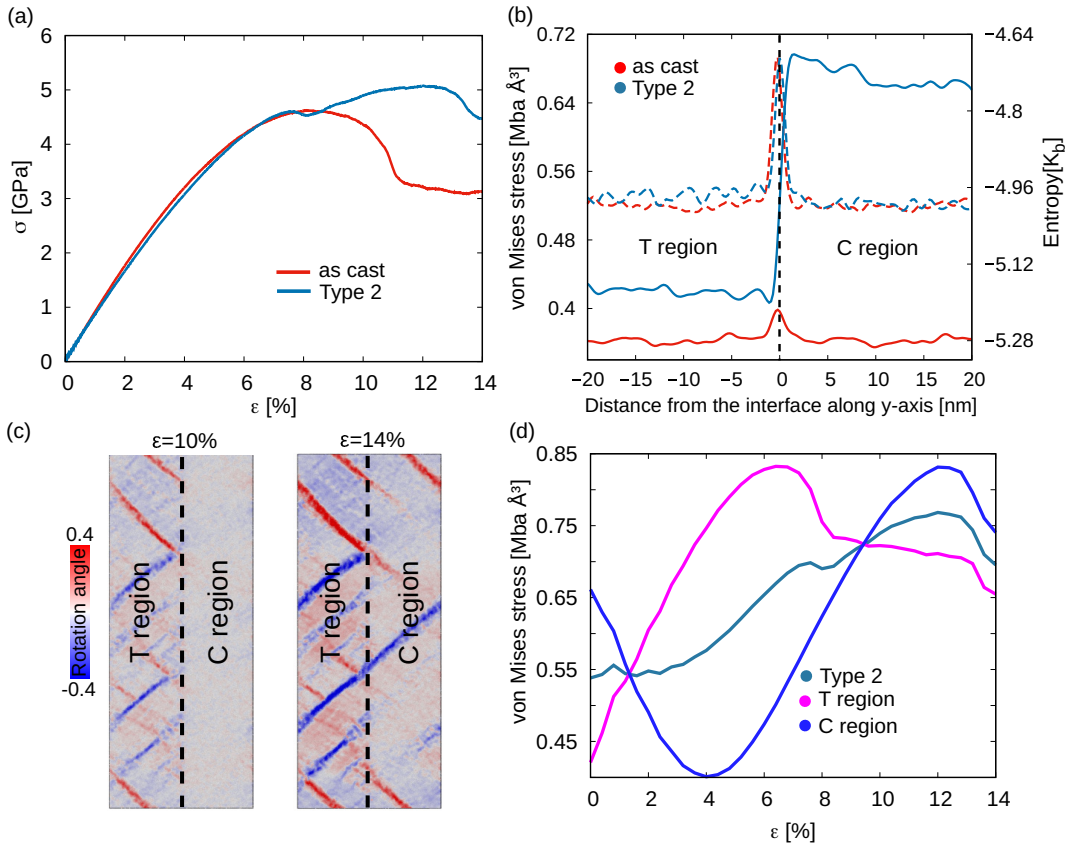


**Figure 4.4:** (a) Tensile stress-strain curves of the Type 2 and as-cast samples. (b) Distribution of stress (solid lines) and local entropy (dashed lines) along the y-axis in the as cast and Type 2 samples at $\epsilon = 0\%$. (c) The deformation mode of the Type 2 sample represents by the sign of the rotation angle (radians) at $\epsilon$ = 10% and $\epsilon$ = 14%. (d) The von Mises stresses of the tensile residual stress (T region), the compressive residual stress (C region), and the entire sample during deformation are calculated individually for comparison. The decrease in von Mises stress in the C region before 4% strain corresponds to the dismissal process of the residual compressive stress.

Under tensile loading, the residual compressive stress can be seen as a back stress that must be overcome by the system to switch to a tensile stress state. During the early stage of deformation, the T region yields first, the SBs will be confined and have no chance to propagate through the interface due to the existence of C region (Fig. 4.4 c). Since none of these SBs becomes critical, the applied stress cannot be compensated by the shear stress released which causes the observed strain-hardening up to a strain level of $\epsilon$ = 13%.

As applied tensile stress continues to increase, compressive residual stress can be overcome gradually and turn into a tensile stress state. This can be proven by the von Mises stress evolution in **Type 2** system during tensile loading as shown in Fig. 4.4 d. The von Mises stress in the T region starts to increase monotonically until the yielding point when partially the stress is released during the shearing process. On the other hand, initially, the von Mises stress in the C region decreases until a strain level of 4% followed by an increase up to a strain level of 13%

when some SBs from the T region propagating through the C region. Based on the comparison of the tensile deformation behavior of **Type 1** and **Type 2**, one may conclude that while structural or stress heterogeneities contribute to ductile improvement, the compressive residual stress is the crucial factor for strain-hardening during tensile.

# 5 Conclusions

Improved plasticity can be induced in MGs by increasing the cooling rate during glass formation, the loading temperature, and the applied strain rate. A higher cooling rate results in the formation of a more disordered glassy structure and, therefore, the fast quenched glass has lower activation energy barriers compared to the slow quenched glass. Consequently, the STZ can be homogeneously dispersed activated in the fast quenched MG which results in a better plasticity during deformation. From the view of energy, the atomic kinetic energy can be increased by increasing the environment temperature during deformation that allows the atoms to easily overcome the activation energy barriers for rearrangement and hence raises the probability for thermal activation of STZs. By applying extremely fast loading, quenties of mechanical energy can be stored in MGs within a short time, resulting in the activation of a large number of STZ events. The interaction of the homogeneous network of STZs can be arised through the vortex mechanism restricts STZ percolation and the formation of one dominate shear band, thus, resulting in a homogeneous deformation. In general, the brittle-to-ductile transition in MGs can be promoted by controlling the STZ activation process. A large number of STZs and, consequently, improved plasticity can be achieved, to the same extent, by thermal treatment, enhancing thermal vibrations or injecting energy into the glassy structure.

By randomly introdicing free volume inside the glassy matrix, the rejuvenation level can be controlled and the threshold for rejuvenation can be found. A dynamic balance between rejuvenation and structural relaxation defines the "highest rejuvenated" state for MGs and no more free volume can be generated inside the glassy matrix. Moreover, a SB shows similar fraction of free volume and atomic-level structure characteristics as the highly rejuvenated MGs. During uniaxial cycling loading, the highly rejuvenated MGs can show strain-hardening with is caused by the stress-induced structural or stress relaxation. Moreover, the incremental relaxation process leads the rejuvenated MG towards a more stable state. Nevertheless, no evidence shows that it can recover the hardness and strength of the initial as-cast state.

Strain-hardening together with enhanced tensile ductility in monolithic MGs can be attained by only modulating the internal residual stress without changing their local structure. Overall, compressive residual stresses together with a heterogeneous stress distribution enable strain-hardening together with the extensive homogeneous flow. Moreover, the residual compressive stress offsets the external tensile stress, which delays SB formation and, therefore, is responsible for efficient strain-hardening and toughness. The fact that MGs can overcome

shear-softening mechanical behavior and achieve strain-hardening and extensive ductility at room temperature without affecting their structure expends the potential of using MGs as structural and functional materials.

# 6 Outlooks

Expanding the application area of MGs is still a challenging field that deserves to be put effort into. Hence, the structural nature and the atomic-level dynamic behavior of MGs need to be further investigated.

One of the open questions that are worth to consisting is the correlation between the energy state and microstructure of MGs. The recent thesis exposed that the MG can be pushed into a "highly rejuvenated" state which contains high fraction of free volume and extremely high energy level. However, the current understanding of the atomic-level structures correlated to different energy state is seriously insufficient. Establishing the relationship between energy state and microstructure will help to understand the origin and structural evolution of amorphous alloys, and provide guidance for the exploration of new materials.

The original mechanism of structural relaxation should also be taken into account in future work. Until now, three type of relaxation mode has been found in MGs but the nature of various relaxation and their connection remains unclear. The fact that the relaxation behavior varies with the different compositions of MGs reminds that the nature of relaxation dynamics may be correlated to the SRO structures in glass materials. Moreover, as our work illustrated the existence of the rejuvenation threshold in MGs, it is worthing to figure out the possibilities of relaxation limitations in MGs. Additionally, the design and study of the mechanism of well-relaxed MG may expand the understanding of the structure of MGs.

Nowadays, strain softening is still a critical issue that limits the application of MGs as functional materials. This thesis provides new insights that can explain strain-hardening during tensile deformation by modulating the stress state of MGs. Evidence indicates that engineering stress is a superior tool for strain-hardening in glassy materials and it is obviously that the propagation of SBs can be delayed by the stress heterogeneity. However, the atomic-level mechanism of STZ activation and percolation under the effect of stress modulation needs to be further investigated which may provide a new understanding of STZ activation and SB formation.

# References

[1] W. Klement, R. Willens, P. Duwez, Non-crystalline structure in solidified gold–silicon alloys, Nature 187 (4740) (1960) 869–870.

[2] W.-H. Wang, C. Dong, C. Shek, Bulk metallic glasses, Materials Science and Engineering: R: Reports 44 (2-3) (2004) 45–89.

[3] A. L. Greer, Metallic glasses, Science 267 (5206) (1995) 1947–1953.

[4] W. L. Johnson, Thermodynamic and kinetic aspects of the crystal to glass transformation in metallic materials, Progress in Materials Science 30 (2) (1986) 81–134.

[5] M. Abiad, M. Carvajal, O. Campanella, A review on methods and theories to describe the glass transition phenomenon: applications in food and pharmaceutical products, Food Engineering Reviews 1 (2) (2009) 105–132.

[6] J. Qiao, J.-M. Pelletier, Dynamic mechanical relaxation in bulk metallic glasses: a review, Journal of Materials Science & Technology 30 (6) (2014) 523–545.

[7] G. Kumar, P. Neibecker, Y. H. Liu, J. Schroers, Critical fictive temperature for plasticity in metallic glasses, Nature communications 4 (1) (2013) 1–7.

[8] H. Chen, D. Turnbull, Formation, stability and structure of palladium-silicon based alloy glasses, Acta metallurgica 17 (8) (1969) 1021–1031.

[9] D. Turnbull, J. C. Fisher, Rate of nucleation in condensed systems, The Journal of chemical physics 17 (1) (1949) 71–73.

[10] D. Turnbull, Under what conditions can a glass be formed?, Contemporary physics 10 (5) (1969) 473–488.

[11] H. Wang, H. Fu, H. Zhang, Z. Hu, A practical thermodynamic method to calculate the best glass-forming composition for bulk metallic glasses, International Journal of Nonlinear Sciences and Numerical Simulation 8 (2) (2007) 171–178.

[12] A. Inoue, Stabilization of metallic supercooled liquid and bulk amorphous alloys, Acta materialia 48 (1) (2000) 279–306.

[13] A. Inoue, T. Zhang, T. Masumoto, Al–la–ni amorphous alloys with a wide supercooled liquid region, Materials transactions, JIM 30 (12) (1989) 965–972.

[14] A. Inoue, T. Zhang, T. Masumoto, Production of amorphous cylinder and sheet of la55al25ni20 alloy by a metallic mold casting method, Materials Transactions, JIM 31 (5) (1990) 425–428.

[15] A. Peker, W. L. Johnson, A highly processable metallic glass: Zr41. 2ti13. 8cu12. 5ni10.

0be22. 5, Applied Physics Letters 63 (17) (1993) 2342–2344.

[16] W. L. Johnson, Bulk glass-forming metallic alloys: Science and technology, MRS bulletin 24 (10) (1999) 42–56.

[17] L. Zhang, J. Jasa, G. Gazonas, A. Jerusalem, M. Negahban, Extracting continuum-like deformation and stress from molecular dynamics simulations, Computer Methods in Applied Mechanics and Engineering 283 (2015) 1010–1031.

[18] Z. Zhang, V. Keppens, O. N. Senkov, D. B. Miracle, Elastic properties of ca-based bulk metallic glasses studied by resonant ultrasound spectroscopy, Materials Science and Engineering: A 471 (1-2) (2007) 151–154.

[19] H. Sheng, W. Luo, F. Alamgir, J. Bai, E. Ma, Atomic packing and short-to-medium-range order in metallic glasses, Nature 439 (7075) (2006) 419–425.

[20] J. Bernal, Geometry of the structure of monatomic liquids, Nature 185 (4706) (1960) 68–70.

[21] J. D. Bernal, The bakerian lecture, 1962. the structure of liquids, Proceedings of the Royal Society of London. Series A, Mathematical and Physical Sciences 280 (1382) (1964) 299–322.

[22] G. D. Scott, Packing of spheres: packing of equal spheres, Nature 188 (4754) (1960) 908–909.

[23] J. Finney, Random packings and the structure of simple liquids. i. the geometry of random close packing, Proceedings of the Royal Society of London. A. Mathematical and Physical Sciences 319 (1539) (1970) 479–493.

[24] Y. Cheng, E. Ma, Atomic-level structure and structure–property relationship in metallic glasses, Progress in materials science 56 (4) (2011) 379–473.

[25] G. Cargill III, Dense random packing of hard spheres as a structural model for noncrystalline metallic solids, Journal of applied physics 41 (5) (1970) 2248–2250.

[26] R. Wang, Short-range structure for amorphous intertransition metal alloys, Nature 278 (5706) (1979) 700–704.

[27] X. Yue, A. Inoue, C.-T. Liu, C. Fan, The development of structure model in metallic glasses, Materials Research 20 (2017) 326–338.

[28] F. C. Frank, Supercooling of liquids, Proceedings of the Royal Society of London. Series A. Mathematical and Physical Sciences 215 (1120) (1952) 43–46.

[29] F. t. Frank, J. Kasper, Complex alloy structures regarded as sphere packings. i. definitions

and basic principles, Acta Crystallographica 11 (3) (1958) 184–190.

[30] F. t. Frank, J. Kasper, Complex alloy structures regarded as sphere packings. ii. analysis and classification of representative structures, Acta Crystallographica 12 (7) (1959) 483–499.

[31] Y. Cheng, H. Sheng, E. Ma, Relationship between structure, dynamics, and mechanical properties in metallic glass-forming alloys, Physical Review B 78 (1) (2008) 014207.

[32] D. Qi, S. Wang, Icosahedral order and defects in metallic liquids and glasses, Physical review B 44 (2) (1991) 884.

[33] E. Ma, Tuning order in disorder, Nature materials 14 (6) (2015) 547–552.

[34] G. Voronoi, Nouvelles applications des paramètres continus à la théorie des formes quadratiques. premier mémoire. sur quelques propriétés des formes quadratiques positives parfaites., Journal für die reine und angewandte Mathematik (Crelles Journal) 1908 (133) (1908) 97–102.

[35] Y. Yang, J. Zhou, F. Zhu, Y. Yuan, D. J. Chang, D. S. Kim, M. Pham, A. Rana, X. Tian, Y. Yao, et al., Determining the three-dimensional atomic structure of an amorphous solid, Nature 592 (7852) (2021) 60–64.

[36] M. H. Cohen, D. Turnbull, Molecular transport in liquids and glasses, The Journal of Chemical Physics 31 (5) (1959) 1164–1169.

[37] D. Turnbull, M. H. Cohen, Free-volume model of the amorphous phase: glass transition, The Journal of chemical physics 34 (1) (1961) 120–125.

[38] D. Turnbull, M. H. Cohen, On the free-volume model of the liquid-glass transition, The journal of chemical physics 52 (6) (1970) 3038–3041.

[39] Q.-K. Li, M. Li, Free volume evolution in metallic glasses subjected to mechanical deformation, Materials transactions 48 (7) (2007) 1816–1821.

[40] S. Feng, K. Chan, L. Zhao, S. Pan, L. Qi, L. Wang, R. Liu, Rejuvenation by weakening the medium range order in zr46cu46al8 metallic glass with pressure preloading: A molecular dynamics simulation study, Materials & Design 158 (2018) 248–255.

[41] W. L. Johnson, J. Lu, M. D. Demetriou, Deformation and flow in bulk metallic glasses and deeply undercooled glass forming liquids—a self consistent dynamic free volume model, Intermetallics 10 (11-12) (2002) 1039–1046.

[42] M. L. Falk, J. S. Langer, Dynamics of viscoplastic deformation in amorphous solids, Physical Review E 57 (6) (1998) 7192.

[43] M. D. Demetriou, W. L. Johnson, Modeling the transient flow of undercooled glass-forming liquids, Journal of applied physics 95 (5) (2004) 2857–2865.

[44] M. D. Demetriou, J. S. Harmon, M. Tao, G. Duan, K. Samwer, W. L. Johnson, Cooperative shear model for the rheology of glass-forming metallic liquids, Physical Review Letters 97 (6) (2006) 065502.

[45] W. L. Johnson, M. D. Demetriou, J. S. Harmon, M. L. Lind, K. Samwer, Rheology and ultrasonic properties of metallic glass-forming liquids: A potential energy landscape perspective, MRS bulletin 32 (8) (2007) 644–650.

[46] M. JIANG, Y. GAO, Structural rejuvenation of metallic glasses and its effect on mechanical behaviors, Acta Metall Sin 57 (4) (2021) 425–438.

[47] W. H. Wang, Dynamic relaxations and relaxation-property relationships in metallic glasses, Progress in Materials Science 106 (2019) 100561.

[48] H.-B. Yu, W.-H. Wang, K. Samwer, The $\beta$ relaxation in metallic glasses: an overview, Materials Today 16 (5) (2013) 183–191.

[49] H. B. Yu, W. H. Wang, H. Y. Bai, K. Samwer, The $\beta$-relaxation in metallic glasses, National Science Review 1 (3) (2014) 429–461.

[50] K. Ngai, Relaxation and diffusion in complex systems, Springer Science & Business Media, 2011.

[51] P. Lunkenheimer, U. Schneider, R. Brand, A. Loid, Glassy dynamics, Contemporary Physics 41 (1) (2000) 15–36.

[52] M. Ediger, P. Harrowell, Perspective: Supercooled liquids and glasses, The Journal of chemical physics 137 (8) (2012) 080901.

[53] J. C. Dyre, Colloquium: The glass transition and elastic models of glass-forming liquids, Reviews of modern physics 78 (3) (2006) 953.

[54] K. Ngai, M. Paluch, Classification of secondary relaxation in glass-formers based on dynamic properties, The Journal of chemical physics 120 (2) (2004) 857–873.

[55] H.-B. Yu, R. Richert, K. Samwer, Structural rearrangements governing johari-goldstein relaxations in metallic glasses, Science advances 3 (11) (2017) e1701577.

[56] F. H. Stillinger, A topographic view of supercooled liquids and glass formation, Science 267 (5206) (1995) 1935–1939.

[57] Q. Wang, S. Zhang, Y. Yang, Y. Dong, C. Liu, J. Lu, Unusual fast secondary relaxation in metallic glass, Nature communications 6 (1) (2015) 1–6.

[58] S. Küchemann, R. Maaß, Gamma relaxation in bulk metallic glasses, Scripta Materialia 137 (2017) 5–8.

[59] H.-B. Yu, K. Samwer, Y. Wu, W. H. Wang, Correlation between $\beta$ relaxation and self-diffusion of the smallest constituting atoms in metallic glasses, Physical review letters 109 (9) (2012) 095508.

[60] H. Yu, X. Shen, Z. Wang, L. Gu, W. Wang, H. Bai, Tensile plasticity in metallic glasses with pronounced $\beta$ relaxations, Physical review letters 108 (1) (2012) 015504.

[61] Z. Wang, P. Wen, L. Huo, H. Bai, W. Wang, Signature of viscous flow units in apparent elastic regime of metallic glasses, Applied Physics Letters 101 (12) (2012) 121906.

[62] C. A. Schuh, T. C. Hufnagel, U. Ramamurty, Mechanical behavior of amorphous alloys, Acta Materialia 55 (12) (2007) 4067–4109.

[63] M. Chen, Mechanical behavior of metallic glasses: microscopic understanding of strength and ductility, Annu. Rev. Mater. Res. 38 (2008) 445–469.

[64] H. B. Yu, K. Samwer, W. H. Wang, H. Y. Bai, Chemical influence on $\beta$-relaxations and the formation of molecule-like metallic glasses, Nature Communications 4 (1) (2013) 1–6.

[65] P. Wen, Z. F. Zhao, M. X. Pan, W. H. Wang, Mechanical relaxation in supercooled liquids of bulk metallic glasses, physica status solidi (a) 207 (12) (2010) 2693–2703.

[66] H. Yu, W. Wang, H. Bai, Y. Wu, M. Chen, Relating activation of shear transformation zones to $\beta$ relaxations in metallic glasses, Physical Review B 81 (22) (2010) 220201.

[67] D. Bedorf, K. Samwer, Length scale effects on relaxations in metallic glasses, Journal of non-crystalline solids 356 (6-8) (2010) 340–343.

[68] Z. Lu, W. Jiao, W. Wang, H. Bai, Flow unit perspective on room temperature homogeneous plastic deformation in metallic glasses, Physical review letters 113 (4) (2014) 045501.

[69] C. Wang, Z. Yang, T. Ma, Y. Sun, Y. Yin, Y. Gong, L. Gu, P. Wen, P. Zhu, Y. Long, et al., High stored energy of metallic glasses induced by high pressure, Applied Physics Letters 110 (11) (2017) 111901.

[70] J. Wang, Y. Shen, J. Perepezko, M. Ediger, Increasing the kinetic stability of bulk metallic glasses, Acta Materialia 104 (2016) 25–32.

[71] W. H. Wang, Correlations between elastic moduli and properties in bulk metallic glasses, Journal of Applied Physics 99 (9) (2006) 093506.

[72] W. H. Wang, The elastic properties, elastic models and elastic perspectives of metallic glasses, Progress in Materials Science 57 (3) (2012) 487–656.

[73] S. Li, P. Huang, F. Wang, Achieving pronounced $\beta$-relaxations and improved plasticity in cuzr metallic glass, Journal of Alloys and Compounds 850 (2021) 156774.

[74] B. Ruta, E. Pineda, Z. Evenson, Relaxation processes and physical aging in metallic glasses, Journal of Physics: Condensed Matter 29 (50) (2017) 503002.

[75] B. Wang, L. Wang, B. Shang, X. Gao, Y. Yang, H. Bai, M. Pan, W. Wang, P. Guan, Revealing the ultra-low-temperature relaxation peak in a model metallic glass, Acta Materialia 195 (2020) 611–620.

[76] Q. Wang, J. Liu, Y. Ye, T. Liu, S. Wang, C. Liu, J. Lu, Y. Yang, Universal secondary relaxation and unusual brittle-to-ductile transition in metallic glasses, Materials Today 20 (6) (2017) 293–300.

[77] T. Pérez-Castañeda, R. J. Jiménez-Riobóo, M. A. Ramos, Do two-level systems and boson peak persist or vanish in hyperaged geological glasses of amber?, Philosophical Magazine 96 (7-9) (2016) 774–787.

[78] J. Pan, Y. Wang, Q. Guo, D. Zhang, A. Greer, Y. Li, Extreme rejuvenation and softening in a bulk metallic glass, Nature communications 9 (1) (2018) 1–9.

[79] B. Shang, W. Wang, A. L. Greer, P. Guan, Atomistic modelling of thermal-cycling rejuvenation in metallic glasses, Acta Materialia 213 (2021) 116952.

[80] S. Ketov, Y. Sun, S. Nachum, Z. Lu, A. Checchi, A. Beraldin, H. Bai, W. Wang, D. Louzguine-Luzgin, M. Carpenter, et al., Rejuvenation of metallic glasses by non-affine thermal strain, Nature 524 (7564) (2015) 200–203.

[81] T. C. Hufnagel, Cryogenic rejuvenation, Nature materials 14 (9) (2015) 867–868.

[82] W. Guo, J. Saida, M. Zhao, S. Lü, S. Wu, Unconspicuous rejuvenation of a pd-based metallic glass upon deep cryogenic cycling treatment, Materials Science and Engineering: A 759 (2019) 59–64.

[83] S. Sohrabi, M. Ri, H. Jiang, L. Gu, P. Wen, Y. Sun, W. Wang, Prominent role of chemical heterogeneity on cryogenic rejuvenation and thermomechanical properties of la–al–ni metallic glass, Intermetallics 111 (2019) 106497.

[84] J. Pan, Y. P. Ivanov, W. Zhou, Y. Li, A. Greer, Strain-hardening and suppression of shear-banding in rejuvenated bulk metallic glass, Nature 578 (7796) (2020) 559–562.

[85] K.-W. Park, C.-M. Lee, M. Wakeda, Y. Shibutani, M. L. Falk, J.-C. Lee, Elastostatically

induced structural disordering in amorphous alloys, Acta Materialia 56 (19) (2008) 5440–5450.

[86] Y. Lou, X. Liu, X. Yang, Y. Ge, D. Zhao, H. Wang, L.-C. Zhang, Z. Liu, Fast rejuvenation in bulk metallic glass induced by ultrasonic vibration precompression, Intermetallics 118 (2020) 106687.

[87] F. Meng, K. Tsuchiya, I. Seiichiro, Y. Yokoyama, Reversible transition of deformation mode by structural rejuvenation and relaxation in bulk metallic glass, Applied Physics Letters 101 (12) (2012) 121914.

[88] J. Qiang, K. Tsuchiya, Composition dependence of mechanically-induced structural rejuvenation in zr-cu-al-ni metallic glasses, Journal of Alloys and Compounds 712 (2017) 250–255.

[89] S. González, J. Fornell, E. Pellicer, S. Suriñach, M. Baró, A. Greer, F. Belzunce, J. Sort, Influence of the shot-peening intensity on the structure and near-surface mechanical properties of ti40zr10cu38pd12 bulk metallic glass, Applied physics letters 103 (21) (2013) 211907.

[90] C. Meylan, J. Orava, A. Greer, Rejuvenation through plastic deformation of a la-based metallic glass measured by fast-scanning calorimetry, Journal of Non-Crystalline Solids: X 8 (2020) 100051.

[91] O. Haruyama, K. Kisara, A. Yamashita, K. Kogure, Y. Yokoyama, K. Sugiyama, Characterization of free volume in cold-rolled zr55cu30ni5al10 bulk metallic glasses, Acta materialia 61 (9) (2013) 3224–3232.

[92] X. Yuan, D. Şopu, J. Eckert, Origin of strain hardening in monolithic metallic glasses, Physical Review B 103 (14) (2021) L140107.

[93] W. Wang, Y. Yang, T. Nieh, C. Liu, On the source of plastic flow in metallic glasses: Concepts and models, Intermetallics 67 (2015) 81–86.

[94] M. M. Trexler, N. N. Thadhani, Mechanical properties of bulk metallic glasses, Progress in Materials Science 55 (8) (2010) 759–839.

[95] A. Greer, Y. Cheng, E. Ma, Shear bands in metallic glasses, Materials Science and Engineering: R: Reports 74 (4) (2013) 71–132.

[96] D. Turnbull, M. H. Cohen, Concerning reconstructive transformation and formation of glass, The Journal of Chemical Physics 29 (5) (1958) 1049–1054.

[97] F. Spaepen, A microscopic mechanism for steady state inhomogeneous flow in metallic

glasses, Acta metallurgica 25 (4) (1977) 407–415.

[98] D. Şopu, X. Yuan, F. Moitzi, F. Spieckermann, X. Bian, J. Eckert, From elastic excitations to macroscopic plasticity in metallic glasses, Applied Materials Today 22 (2021) 100958.

[99] D. Şopu, A. Stukowski, M. Stoica, S. Scudino, Atomic-level processes of shear band nucleation in metallic glasses, Physical review letters 119 (19) (2017) 195503.

[100] A. Argon, Plastic deformation in metallic glasses, Acta metallurgica 27 (1) (1979) 47–58.

[101] D. Srolovitz, V. Vitek, T. Egami, An atomistic study of deformation of amorphous metals, Acta Metallurgica 31 (2) (1983) 335–352.

[102] M. Zink, K. Samwer, W. Johnson, S. Mayr, Plastic deformation of metallic glasses: Size of shear transformation zones from molecular dynamics simulations, Physical Review B 73 (17) (2006) 172203.

[103] R. Dasgupta, H. G. E. Hentschel, I. Procaccia, Microscopic mechanism of shear bands in amorphous solids, Physical review letters 109 (25) (2012) 255502.

[104] D. Rodney, C. Schuh, Distribution of thermally activated plastic events in a flowing glass, Physical review letters 102 (23) (2009) 235503.

[105] D. Şopu, S. Scudino, X. Bian, C. Gammer, Eckert, J, Atomic-scale origin of shear band multiplication in heterogeneous metallic glasses, Scripta Materialia 178 (2020) 57–61.

[106] F. Shimizu, S. Ogata, J. Li, Yield point of metallic glass, Acta materialia 54 (16) (2006) 4293–4298.

[107] S. Ogata, F. Shimizu, J. Li, M. Wakeda, Y. Shibutani, Atomistic simulation of shear localization in cu–zr bulk metallic glass, Intermetallics 14 (8-9) (2006) 1033–1037.

[108] A. Cao, Y. Cheng, E. Ma, Structural processes that initiate shear localization in metallic glass, Acta Materialia 57 (17) (2009) 5146–5155.

[109] J. Li, Z. L. Wang, T. Hufnagel, Characterization of nanometer-scale defects in metallic glasses by quantitative high-resolution transmission electron microscopy, Physical Review B 65 (14) (2002) 144201.

[110] Y. Chen, T. Ohkubo, T. Mukai, K. Hono, Structure of shear bands in pd40ni40p20 bulk metallic glass, Journal of Materials Research 24 (1) (2009) 1–9.

[111] C. Liu, Y. Ikeda, R. Maaß, Strain-dependent shear-band structure in a zr-based bulk metallic glass, Scripta Materialia 190 (2021) 75–79.

[112] F. Moitzi, D. Şopu, D. Holec, D. Perera, N. Mousseau, J. Eckert, Chemical bonding effects on the brittle-to-ductile transition in metallic glasses, Acta Materialia 188 (2020)

273–281.

[113] K. Albe, Y. Ritter, D. Şopu, Enhancing the plasticity of metallic glasses: Shear band formation, nanocomposites and nanoglasses investigated by molecular dynamics simulations, Mechanics of Materials 67 (2013) 94–103.

[114] F. Méar, B. Doisneau, A. Yavari, A. Greer, Structural effects of shot-peening in bulk metallic glasses, Journal of alloys and compounds 483 (1-2) (2009) 256–259.

[115] F. Mear, G. Vaughan, A. Yavari, A. Greer, Residual-stress distribution in shot-peened metallic-glass plate, Philosophical Magazine Letters 88 (11) (2008) 757–766.

[116] Y. Cao, X. Xie, J. Antonaglia, B. Winiarski, G. Wang, Y. C. Shin, P. J. Withers, K. A. Dahmen, P. K. Liaw, Laser shock peening on zr-based bulk metallic glass and its effect on plasticity: experiment and modeling, Scientific reports 5 (1) (2015) 1–8.

[117] H. Fehske, R. Schneider, A. Weiße, Computational many-particle physics, Vol. 739, Springer, 2007.

[118] X. Li, H. Gao, Atomistic modelling of deformation and failure mechanisms in nanostructured materials, National Science Review 2 (2) (2015) 133–136.

[119] D. Sopu, Molecular dynamics simulations of metallic nanoglasses, Doctoral Thesis.

[120] D. Şopu, C. Soyarslan, B. Sarac, S. Bargmann, M. Stoica, J. Eckert, Structure-property relationships in nanoporous metallic glasses, Acta materialia 106 (2016) 199–207.

[121] D. Sopu, A. Foroughi, M. Stoica, J. Eckert, Brittle-to-ductile transition in metallic glass nanowires, Nano letters 16 (7) (2016) 4467–4471.

[122] D. Şopu, K. Albe, J. Eckert, Metallic glass nanolaminates with shape memory alloys, Acta Materialia 159 (2018) 344–351.

[123] V. Borovikov, M. I. Mendelev, A. H. King, Effects of stable and unstable stacking fault energy on dislocation nucleation in nano-crystalline metals, Modelling and Simulation in Materials Science and Engineering 24 (8) (2016) 085017.

[124] M. Mendelev, D. Sordelet, M. Kramer, Using atomistic computer simulations to analyze x-ray diffraction data from metallic glasses, Journal of Applied Physics 102 (4) (2007) 043501.

[125] J. Tersoff, Empirical interatomic potential for silicon with improved elastic properties, Physical Review B 38 (14) (1988) 9902.

[126] A. Stukowski, Visualization and analysis of atomistic simulation data with ovito–the open visualization tool, Modelling and simulation in materials science and engineering

18 (1) (2009) 015012.

[127] Y. Cheng, A. Cao, E. Ma, Correlation between the elastic modulus and the intrinsic plastic behavior of metallic glasses: The roles of atomic configuration and alloy composition, Acta Materialia 57 (11) (2009) 3253–3267.

[128] Y. Fan, T. Iwashita, T. Egami, Crossover from localized to cascade relaxations in metallic glasses, Physical Review Letters 115 (4) (2015) 045501.

[129] L. Tian, L. Li, J. Ding, N. Mousseau, Art_data_analyzer: Automating parallelized computations to study the evolution of materials, SoftwareX 9 (2019) 238–243.

[130] N. Mousseau, L. K. Béland, P. Brommer, J.-F. Joly, F. El-Mellouhi, E. Machado-Charry, M.-C. Marinica, P. Pochet, The activation-relaxation technique: Art nouveau and kinetic art, Journal of Atomic and Molecular Physics 2012.

# 7 Publication list

## 7.1 Publications included in this thesis

**X. Yuan**, D. Şopu, F. Moitzi, K. K. Song, J, Eckert. Intrinsic and extrinsic effects on the brittle-to-ductile transition in metallic glasses. **Journal of Applied Physics**, 2020, 128(12): 125102.

**X. Yuan**, D. Şopu, J. Eckert. Origin of strain hardening in monolithic metallic glasses. **Physical Review B**, 103.14 (2021): L140107.

**X. Yuan**, D. Şopu, F. Spieckermann, K. K. Song, S. V. Ketov, K. G. Prashanth, J. Eckert. Maximizing the degree of rejuvenation in metallic glasses. **Scripta Materialia**, 212 (2022): 114575.

**X. Yuan**, D. Şopu, K. K. Song, J. Eckert. Relaxation and Strain-Hardening Relationships in Highly Rejuvenated Metallic Glasses. **Materials** 15.5 (2022): 1702.

## 7.2 Publications not included in this thesis

**X. Yuan**, Z. Zhang, Q. Gao, L. Zhou, K. Song, X. Zou, D. Şopu, L. Hu, B. Sun, J. Eckert. Enhanced mechanical properties of Zr65Cu15Ni10Al10 bulk metallic glass by simultaneously introducing surface grooves and multiple shear bands. **Journal of Materials Research and Technology**, 2022, Accepted.

D. Şopu, **X. Yuan**, F. Moitzi, F. Spieckermann, X. Bian, J. Eckert. From elastic excitations to macroscopic plasticity in metallic glasses. **Applied Materials Today** 22 (2021): 100958.

D. Şopu, **X. Yuan**, J. Eckert. Annealing metallic glasses above $T_g$ in order to accelerate the relaxation process in molecular dynamics simulations. **Applied Physics Letters**, 120.1 (2022): 011904.

W. P. Wu, D. Şopu, **X. Yuan**, O. Adjaoud, K. K. Song, J. Eckert. Atomistic understanding of creep and relaxation mechanisms of Cu64Zr36 metallic glass at different temperatures and stress levels. **Journal of Non-Crystalline Solids**, 559 (2021): 120676.

W. P. Wu, D. Şopu, **X. Yuan**, J. Eckert. Aspect ratio-dependent nanoindentation behavior of Cu64Zr36 metallic glass nanopillars investigated by molecular dynamics simulations. **Journal of Applied Physics**, 128.8 (2020): 084303.

Q. Xu, D. Şopu, **X. Yuan**, D. Kiener, J. Eckert, Interface-related deformation phenomena in metallic glass/high entropy nanolaminates. **Acta Materialia**, 237 (2022): 118191.

# Part II: Publications included in this thesis

# Publication I

Journal of Applied Physics ARTICLE scitation.org/journal/jap

# Intrinsic and extrinsic effects on the brittle-to-ductile transition in metallic glasses

Cite as: J. Appl. Phys. **128**, 125102 (2020); doi: 10.1063/5.0020201
Submitted: 29 June 2020 · Accepted: 3 September 2020 ·
Published Online: 22 September 2020


X. Yuan,[1] D. Şopu,[1,2,a)] F. Moitzi,[1] K. K. Song,[3] and J. Eckert[1,4]

**AFFILIATIONS**

[1]Erich Schmid Institute of Materials Science, Austrian Academy of Sciences, Jahnstraße 12, 8700 Leoben, Austria
[2]Fachgebiet Materialmodellierung, Institut für Materialwissenschaft, TU Darmstadt, Otto-Berndt-Straße 3, D-64287 Darmstadt, Germany
[3]School of Mechanical, Electrical & Information Engineering, Shandong University (Weihai), Weihai 264209, China
[4]Department of Materials Science, Chair of Material Physics, Montanuniversität Leoben, Jahnstraße 12, 8700 Leoben, Austria

[a)]**Author to whom correspondence should be addressed:** daniel.sopu@oaew.ac.at

**ABSTRACT**

The effects of cooling rate, temperature, and applied strain rate on the tensile deformation behavior of a $Cu_{64}Zr_{36}$ metallic glass (MG) are investigated using large-scale molecular dynamics simulations. An increase in the quenching rate during sample preparation, as well as an increase of the temperature or the applied strain rate, affects the activation of shear transformation zones (STZs) and, consequently, the shear-banding processes, which ultimately causes a brittle-to-ductile transition in the deformation behavior of MGs. A quantitative interpretation for the observed enhanced ductility in MGs with an increasing quenching rate is obtained by sampling the saddle points on the potential energy surface. High quenching rates lead to lower energy barriers for activation of a local atomic rearrangement (STZ) as compared to those MGs obtained at low quenching rates. Although the glassy structure does not show significant variations with increasing temperature, the kinetic energy of the atoms increases dramatically, which allows the atoms to rearrange easily; therefore, the probability of homogeneous thermal activation of STZs increases. Finally, a large number of STZs can also be activated by deformation at high strain rates when a large amount of elastic energy is stored in the glassy matrix. Consequently, a high density of STZ events and, therefore, a more complex percolation process results in a low probability for strain localization and formation of critical shear bands. Our results provide an atomistic understanding for the strain localization mechanisms in metallic glasses and shed more light on the brittle-to-ductile transition.

## 1.Introduction

Analyzing and controlling the deformation mechanisms of metallic glasses (MGs) has attracted a large amount of research in the past few decades[1–6]. Because of the formation of highly localized shear bands, sudden catastrophic failure will appear during room temperature deformation, which extremely restricts the plasticity of MGs[5, 7–9]. So far, significant plasticity has been reported during high temperatures deformation tests[10], for high strain rates loading conditions[11] as well as in metallic glasses fabricated with higher cooling rates[12, 13]. Controlling the cooling rates, temperature and strain rates allows for homogeneous plastic strain distribution and hampers critical shear band generation. For instance, upon loading the shear band nucleation and evolution processes strongly depend on the testing temperature[14]. Indeed, it has been suggested that the volume[15] of shear transformation zones (STZ), the plasticity-carriers in MGs, increase with temperature. Furthermore, by controlling the cooling rates the amount of free volume induced during solidification can be varied ultimately, improving the plasticity of MGs[16]. Here, the excess free volume influences the energy barrier for STZ activation and consequently, determines the STZ volume, as well as their shape and distribution which has implications on the STZ percolation and shear band formation processes. Finally, when it comes to mechanical testing, a strain rate sensitivity of the deformation mechanism of MGs has been reported[17]. An increase in the STZ volume was observed with decreasing the loading rate which ultimately leads to better plasticity[18, 19]. All these studies suggest that STZ characteristics control the brittle-to-ductile transition in MGs. However, previous studies have mentioned that a STZ is not a structural defect but rather a local flow event where a group of atoms undergoes an inelastic shear distortion under the action of an applied stress[5]. Hence, a STZ cannot be visualized based on the conventional methods used generally to analyze crystalline defects such as dislocations and twins. Since Argon proposed the concept of shear transformation[20–22], no experiment was able to detect and visualize such an elementary event in MG. This is why most early work on STZ activation and percolation processes employed computer simulation, which remains a popular and powerful tool today in the study of the deformation of MGs. So far, large efforts have been undertaken to analyze and understand the mechanisms of STZ activation and percolation[23]. The condensation of STZs along a viable shear path causes the nucleation of a shear band[11, 24]. However, due to the amorphous nature of MGs and the spatial and temporal scales of the deformation

processes[4, 5, 25], the structure-property relationships and the atomic-level mechanism behind the brittle-to-ductile transition are challenging to be investigated though experiments. Molecular dynamics simulations (MD) have provided several useful insights into the atomic-level structure of MGs while theMolecular dynamics simulations scales of MD are ideal for analyzing the shear bands nucleation and propagation mechanisms. Recently, great advances have been made through joint efforts from simulations to reveal the structure of MGs[26–28], understanding the mechanism of shear band nucleation[23] and providing effective approaches to improve mechanical properties of MGs[11, 29–31]. The goal of this work is to couple temperature, cooling rate and applied stress effects to the deformation behavior of MGs and provide insights into the correlation between the atomic-scale mechanism of STZ activation and percolation and the macroscopic deformation process. We model the $Cu_{64}Zr_{36}$ MG system using MD simulations and provide a systematic investigation on the brittle-to-ductile transition during tensile deformation. A quantitative analysis of the impact of intrinsic and extrinsic factors on the strain localization process is provided. By analyzing the kinetic energy per atom the characteristics of the brittle-to-ductile transition with increasing temperature are disclosed. The effect of cooling rate, and basically, the effect of thermal history on structural fluctuations, will be quantified by sampling the activation energy barrier of local atomic rearrangements. Finally, the observed improved ductility during high strain rate deformation is elucidated by calculating the sign of the rotation angle[32].

## 2. Simulation approach

### 2.1.Molecular dynamics simulations

To analyze and understand the deformation mechanism of MG, tensile simulations were carried out with the large-scale molecular dynamics simulation software LAMMPS[33]. The interatomic interaction is described by the modified Finnis-Sinclair-type potential for Cu-Zr binary alloys proposed by Mendelev et al.[34]. For all simulations, a constant integration time step of 2 $fs$ was used. The MG sample was prepared following a four step procedure: For the first step, 900000 atoms were randomly distributed in a box of 2.5 $\times$ 55 $\times$ 110 $nm^3$ with periodic boundary conditions in all three directions and relaxed at 1600 $K$ for 1 $ns$ to ensure chemical homogeneity. A uniform-acceptance force bias Monte Carlo approach[35] and MD in an NPT ensemble were used alternately, to deal with the overlap between the atoms during the initial equilibration of the liquid structure[36]. Second, the melt was quenched from 1600 $K$ to 850

$K$ which is 50 $K$ above $T_g$ with a 10 $K/ps$ cooling rate. Then, the sample was cooled down with a cooling rate of 0.01 $K/ps$ from 850 $K$ to 750 $K$ to get a well-relaxed structure is in a temperature range of 100 $K$ around $T_g$(≈800 $K$). After reaching 750 $K$, a 4 $ns$ relaxation was performed on the sample and then the sample was quenched to 50 $K$ at 10 $K/ps$. The relaxed sample was replicated twice along the $x-$direction. A second glass was prepared by remelting at 1600 $K$ the previously prepared glass and quenched back to 50K with a higher cooling rate of 1 $K/ps$. Before tensile deformation, all samples were relaxed to zero pressure at 50 $K$ for 1 $ns$.

To study the effect of cooling rate on the deformation mechanism of $Cu_{64}Zr_{36}$ MG, the samples prepared at the two different cooling rates were deformed in tensile parallel to the z-direction with a constant engineering strain rate of 4 $\times$ $10^7$ $/s$ at 50 $K$. These tensile tests are denoted as T1 and T2, respectively. To investigate the temperature effect the initially prepared glass was heated to 300 K and relaxed at this temperature for 100 ps. Then, this sample was deformed with a constant engineering strain rate of 4 $\times$ $10^7$ $/s$ and this test was denoted as T3. Lastly, the effect of strain rate was analyzed by conducting a uniaxial tensile test using a higher strain rate of $10^9$ $/s$ at 50 $K$ and this test was called as T4. All tensile simulations were carried out in an NPT ensemble and periodic boundary conditions were applied in $x-$ and $z-$ directions while free surface conditions were applied in the $y-$direction to capture the shear band nucleation. Afterwards, the atomic-scale deformation mechanisms were analyzed by calculating the local atomic shear strain and rotation angle with the OVITO software[37].

### 2.2 Activation-Relaxation Technique

In our work, we used the Activation-Relaxation Technique (ART)[38–40] to investigate the activation barriers energy of $Cu_{64}Zr_{36}$ MG. ART is an open-ended saddle point search algorithm[38] which is known to be capable of providing the key connections between a given energy minimum state and its surrounding saddle states and neighboring local minima, such as the activation energy or the atomic displacement[41]. It offers a way to locally sample the potential energy landscape (PEL) and quantify activation pathways between adjacent energy minima. It is also capable of capturing high activation barrier events which are not accessible by MD[42–44]. In our research, the samples size of the ART simulation are 2.5 $\times$ 10.5 $\times$ 10.5 $nm^3$, both contains 18000 atoms and were created using two cooling rates of 0.01 $K/ps$ and 1 $K/ps$, respectively. The cooled samples were relaxed at around 0 $K$ with global interatomic forces minimized to $10^{-6}$ $eV/$Å before the ART simulation. The prepared samples with different cooling rates

served as the initial configurations in ART. The activation energy around each atom is calculated and 10 relaxation pathways were searched always starting from the same initial structure.

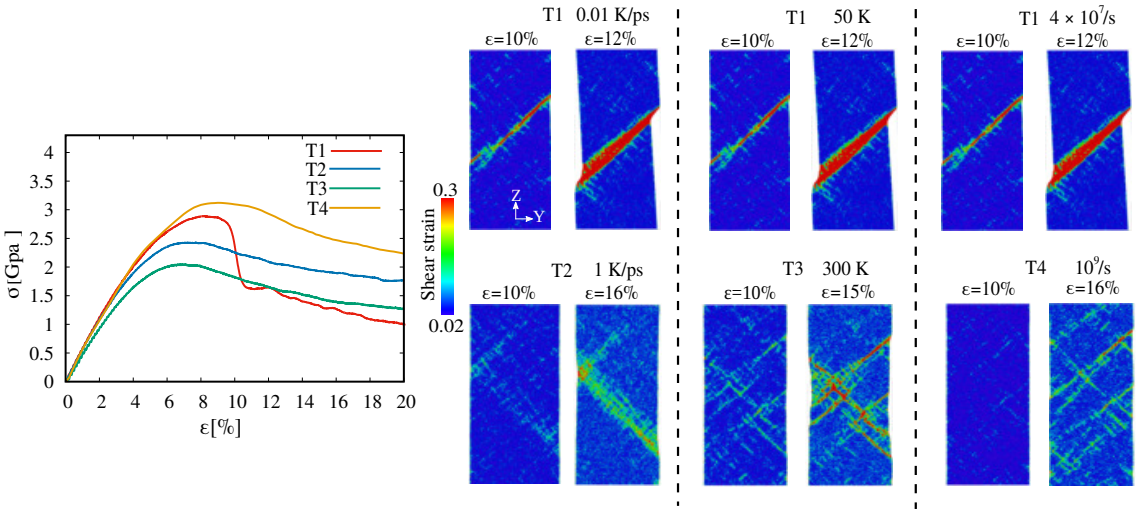


**Figure 7.1:** Uniaxial tensile stress-strain curves together with snapshots of the local atomic shear strain at different strain levels for two cooling rates (T1 and T2), two temperatures (T1 and T3) and two strain rates (T1 and T4). In T1 the plastic deformation is highly localized in one dominant shear band. Although the strain is also localized in T2 the shear band is wider and even at a strain level of 16% no shear offset can be identified. T3 shows that two main shear bands form that join with other embryonic shear bands. T4 shows a web-like network of embryonic shear bands and no dominant shear band forms even under extensive loading up to a strain of 16%.

## 3. Effect of quenching rate, temperature and strain rate on the deformation mechanism

The uniaxial tensile test stress-strain curves together with snapshots of the local atomic shear strain are shown for different cooling rates, temperatures and stain rates in Fig. 7.23. Under load, T1 exhibits a brittle-like fracture following the initiation and propagation of a highly localized shear band. This is consistent with the sudden stress drop in the stress-strain curve. Otherwise, T2, T3, and T4 show a different mechanical response compared with T1. Increasing the cooling rate during sample preparation, as well as an increase of temperature or applied strain rate, affects the shear band nucleation and propagation mechanisms during deformation finally causing a brittle-to-ductile transition. In the T2 case, when the sample is prepared at a cooling rate of two orders of magnitude higher than in the T1 case, one can see that the strain is still localized but the formed shear bands is wider with many plastic zones distributed randomly in the sample. Moreover, even at a high strain level of 16% no shear offset can be observed and the sample elongates along the z-direction instead of sliding along the shear band rendering in a

ductile-like deformation. With the increase of temperature, the plasticity in the MG is no longer localized in one dominant shear band. In the T3 case, two main shear bands form and joing with other embryonic shear bands. The interaction of these multiple shear bands does not allow any of the two shear bands to become critical resulting in ductile deformation. Comparing the stress-strain curves of T1 with T2 and T3, one can see that by increasing the cooling rate or by increasing the applied temperature not only the plasticity is strongly enhanced but also the yield strength of the MG decreases significantly. This observation is in agreement with previous experiments[10] and simulations[11]. For instance, significant tensile ductility was reported for microscopic samples of around 100 nm[45] as well as for high strain rates[46]. Here, we also find that increasing the applied strain rate results in a significant difference in plastic response as shown in Fig. 7.23. A pattern of multiple shear bands intersecting each other causes the formation of network-like defects in the sample instead of highly localized shear. Both the plasticity and yield strength increase when the strain rate increases from $4 \times 10^7$ $/s$ to $10^9$ $/s$. This behavior is attributed to the high tensile strain rate. According to Albe et al. [11], when the applied strain rate is higher than the shear band nucleation rate, shear band nuclei cannot mature into extended defects and then deformation becomes homogeneous. Besides, it seems that fast loading can also affect the activation of STZs and their interaction but an atomistic understanding of the underlying process clearly requires further study. At this point, we can conclude that quenching rate, temperature and strain rate are controlling factors for the brittle-to-ductile transition in MGs. Moreover, how these factors determine the transition in the strain localization mechanism is an important question that we address next.

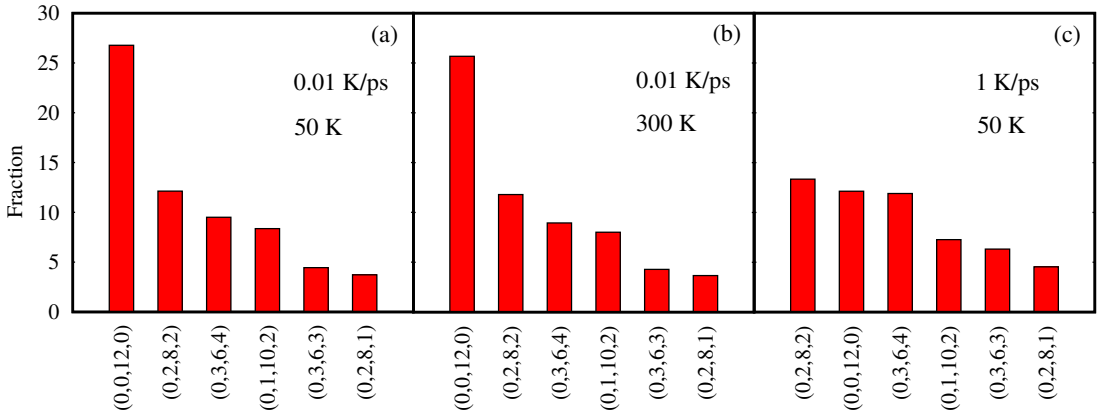


**Figure 7.2:** Histogram of the fraction of Cu-centered Voronoi polyhedra before tensile deformation in $Cu_{64}Zr_{36}$ metallic glass as a function of cooling rate and temperature. Panels (a) and (b) shows that the fraction of full icosahedra(FI) (0,0,12,0) is higher than 25% for a cooling rate of 0.01 $K/ps$. Panel (c) shows that the FI fraction decreases significantly to only 11% after quenching with a rate of 1 $K/ps$. Nevertheless, an increases in temperature slightly affects the local structure (panel (a) and (b)).

# 4. Quantitative analysis of the atomic-scale deformation mechanism

## 4.1 Effect of cooling rate

It has been reported that using a high cooling rate during MGs preparation can cause substantial tensile plasticity[12, 13]. This tendency can also be found in our research as discussed above. The observed brittle-to-ductile transition with increasing cooling rate is associated with the change in the deformation mechanism. As already shown in the literature, the structure of a MG is sensitive to the processing history (such as using different cooling rates for MG preparation)[47]. Cheng et al.[48] pointed out that the intrinsic mechanical properties of a MG are controlled by the composition and the internal atomic structure. In order to confirm the structural changes induced the by cooling rate, the structure of the undeformed sample was analyzed using the Voronoi tessellation method implemented in OVITO while we focus on the distribution of Cu-centered full icosahedra (FI) clusters. This icosahedral unit is the fingerprint of short-range order in $Cu_{64}Zr_{36}$ MG and plays an important role in the material properties[49, 50]. Fig. 7.24 shows the frequency distribution of the dominant Voronoi polyhedra in $Cu_{64}Zr_{36}$ MG.

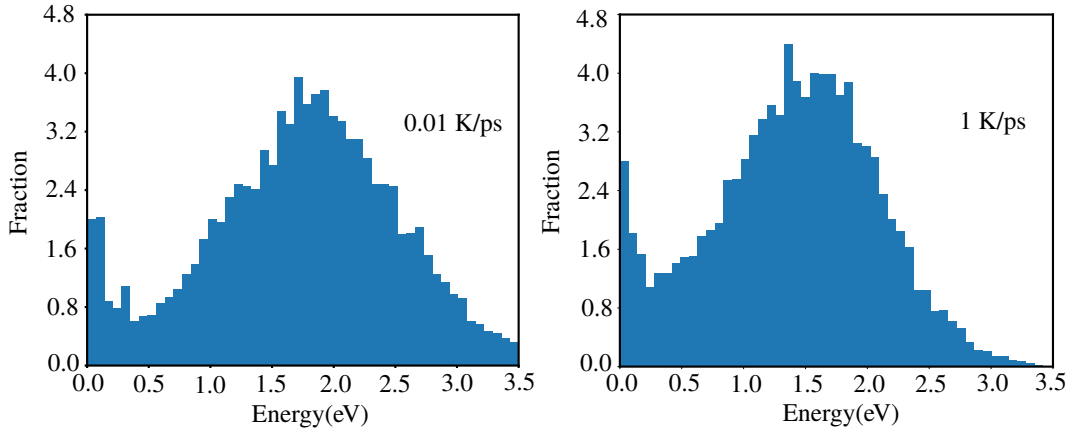


**Figure 7.3:** Histogram of the activation energy barrier for two MGs quenched at different cooling rates as obtained by ART.

After quenching with a 0.01 $K/ps$ cooling rate, the FI is the most prominent Voronoi polyhedron with a fraction higher than 25%, The percentage will significantly decrease to 11% when increasing the quenching rate to 1 $K/ps$ (Fig. 7.24(c)). The FI cluster exhibit a high packing density, high shear resistance, and low local atomic mobility[48, 51]. Our findings indicate that the local structure of the high cooling rate sample has a lower packing density than the low cooling rate sample. Although it is well known that different cooling histories can cause a significant change in the structure of MG's and hence, affect their plasticity, as atomic-level

understanding of the brittle-to-ductile transition mechanism is still lacking. Here, we give a quantitative analysis of the observed transition by sampling the activation energy barrier.

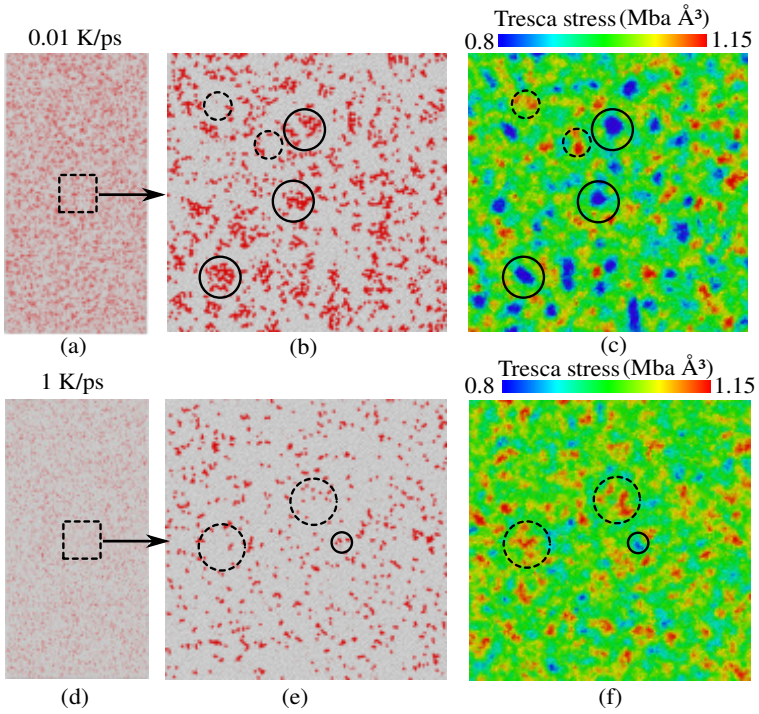


**Figure 7.4:** Structure-stress relation analysis before deformation. FI distribution (red atoms) at $\varepsilon$ = 0% (before deformation) for the sample quenched with 0.01 $K/ps$ (a) and 1 $K/ps$ (d) cooling rates. (b) and (e) panels are the enlarged dashed squares in (a) and (d). Panels (c) and (f) display the Tresca stress distribution of the dashed squares in (a) and (d).

The activation energy barrier is the energy differences between the initial minimum state and the saddle state in the potential energy landscape[42, 52] and it is the barrier that needs to be overcome to move atoms from the initial energy minimum position to an adjacent energy minimum position, In real space, this is usually observed as structural rearrangement of atoms[53]. The activation barrier is known to be correlated to the local structure in MGs[54, 55]. Atoms with low activation barriers are easy to rearrange during deformation. As one can find from Fig. 7.25, the sample prepared at 0.01 K/ps cooling rate experience a higher average activation energy barrier ($\approx$1.8 $eV$) compared to the one prepared at a much higher cooling rate ($\approx$1.6 $eV$). Moreover, in the sample quenched at 1 $K/ps$ almost 20% of the activation energy barriers are lower than 1.0 $eV$. The percentage will decrease to 10% when the quenching rate decreases to 0.01 $K/ps$. Local atomic rearrangement events will, therefore, be more likely in the fast quenched sample and STZ events can be activated at lower applied stress resulting in a much lower yield stress level as compared to the slowly cooled sample.

Elastostatic compression loading demonstrated that plastic atomic rearrangements take

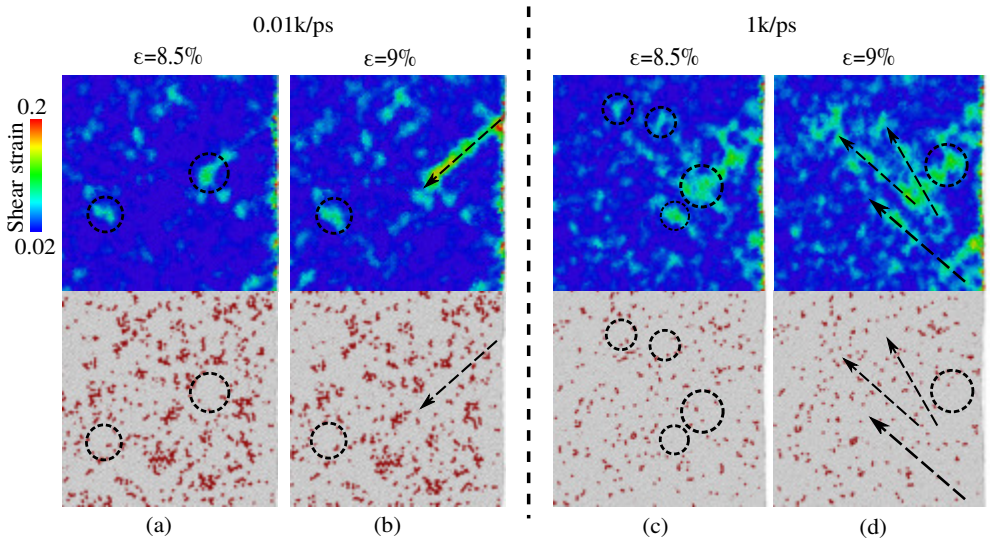


**Figure 7.5:** Correlation between atomic shear strain and FI cluster structure. (a) and (b) panels show that STZ activation and percolation processes are highly restricted by the distribution of a large number of FI clusters. Nevertheless, a low fraction of FI clusters results in a homogeneous activation of a large number of STZs, as shown in panels (c) and (d).

place at stresses well below the onset of plastic deformation[56]. Together with a highly heterogeneous atomic structure MGs also possess a high degree of local elastic fluctuations that may be activated to stresses below the macroscopic yield stress[57, 58]. Thus, the structure-stress relationship is investigated while the closed-packed FI clusters and the Tresca stress distributions are analyzed in comparison. In Fig. 7.26 one can see that those areas (solid line circles) with a high number of densely packed FI clusters show low values of the Tresca stress. These densely packed areas are shielded from the influence of the applied stress. On the other hand, areas with geometrical unfavorable motifs (low number of FI clusters) exhibit high stress concentration (dashed line circles). Moreover, the low volume fraction of FI clusters in the MG obtained at a high cooling rate results in an overall higher Tresca stress field that can be associated with the high degree of structural disorder (Fig. 7.26(f)). Under load, the stress for STZ activation is first overcome in these soft areas of high Tresca stress. Hence, the atoms in the more loosely packed areas are much more sensitive to the applied stress, and, therefore, are easy to be activated. Consequently, the low density of FI clusters in the fast quenched sample results in a homogeneous activation of a large number of STZs, and hence, a more homogeneous deformation distributed throughout the MG (see Fig. 7.5(c)). Additionally, the homogeneous network of STZs obstructs their percolation and the formation of a dominant shear band (see Fig. 7.5(d)). For the MG quenched at a low cooling rate, the Tresca stress field is overall much lower which ultimately results in a higher yield stress. In the early stage of deformation, only a

low number of STZs activate at those areas of high stress and low number of FI clusters (Fig. 7.5(a)). Since much higher stresses are required to activate new STZs in the glassy structure the initial STZs have enough time to percolate and a shear band develops along a viable path with less FI clusters so that the structure inside is softer that the surrounding matrix (Fig. 7.5(b)).

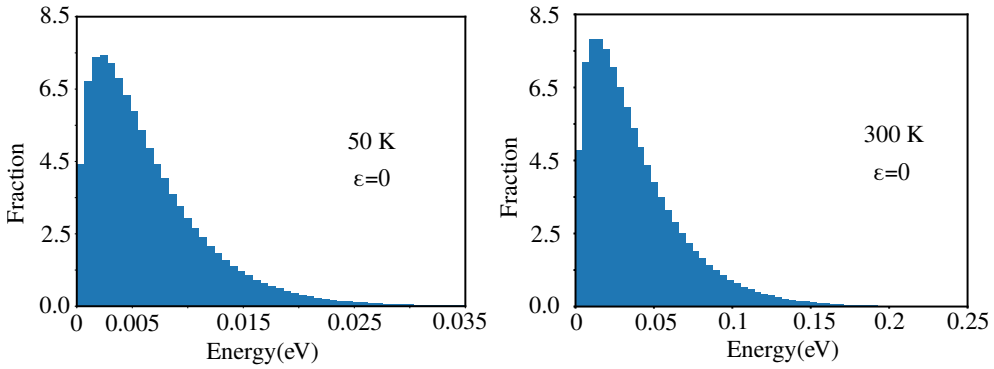


**Figure 7.6:** Average kinetic energy per atom in the sample at temperature of 50 $K$ and 300 $K$, respectively.

### 4.2 Effect of temperature

The deformation behavior of MGs is sensitive to temperature. At room temperature, plastic deformation in MGs occurs highly localized in one dominant shear band and the material fails via brittle fracture. Nevertheless, at high temperatures, i.e., at T$\geqslant$0.7$T_g$, MGs show considerable ductility and a STZ-dominated homogeneous plasticity[59]. Even when the deformation is conducted at temperatures much lower than $T_g$, i.e., at T$\approx$0.4$T_g$, a reasonable enhancement of plasticity has been observed[60]. Since structural features control the deformation behavior of MGs one can assume that the structure of glassy materials suffers large variations during heating even below $T_g$. A similar phenomenon was observed in our simulations. By increasing the temperature from 50$K$ to 300 $K$($\approx$0.38$T_g$) a brittle-to-ductile transition is found that is associated with a change in the deformation mechanism from one dominant shear band to a V-shape shear band region. Interestingly, we noticed that no obvious correlation between structural variations and the observed transition in the deformation behavior. Fig. 7.24 indicates that the local atomic structure does not considerably change after heating to 300 $K$. Nevertheless, the kinetic energy per atom shows a significant increase during heating, as shown in Fig. 7.6. The kinetic energy at 300 $K$ is almost ten times higher than the value at 50 $K$. All the kinetic energies are lower than 0.05 $eV$ at 50 $K$, while at 300 $K$ more than 40% exceed 0.05 $eV$. Thus, during high-temperature deformation, STZs can be also activated by thermal vibrations. Consequently, although the structure and the related activation energy does not change considerably with tem-

perature, STZs can easier overcome the energy barriers for activation by phonon pumping. As a results, with increasing the temperature STZ activation occurs at lower stress levels while the macroscopic yield stress will decrease accordingly (see Fig. 7.23). Moreover, a larger population of STZs will be activated in the glass matrix resulting in a more complex percolation process contributing to the proliferation of multiple shear bands (see Fig. 7.24). We have to mention that the structures obtained in MD simulations are not well-relaxed as those quenched in experiments at cooling rates order of magnitudes lower. Hence, the roughness of the potential energy surface is higher in experimental samples and consequently, the brittle-to-ductile transition takes place at temperatures much higher that those found in simulations.

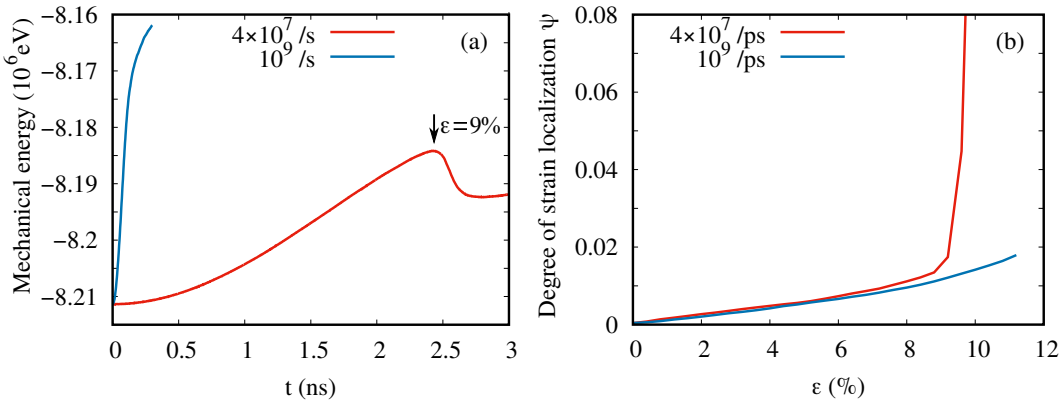


**Figure 7.7:** (a): Evolution of the mechanical energy of samples deformed at high strain and low strain rates. (b) High strain rate deformation shows lower $\psi$ values than the low strain rate deformation.

### 4.3. Effect of strain rate

In addition to the temperature and the quenching conditions, strain localization is very sensitive to the loading conditions. During plastic deformation, atoms must rearrange themselves to accommodate the increase of applied strain[61]. Greer et al.[62] suggested that energy is stored in the materials in the early stages of elastic deformation that finally, induces damage and defects in MGs. Fig. 7.7(a) revels that the mechanical energy (the summation of kinetic energy and potential energy of the system) sharply increases within an extremely short time in the sample during high strain rate deformation ($10^9/s$). Basically, at high strain rates one can assume that there is not enough time for local relaxations and stress redistribution and higher stresses are required for the atoms to rearrange and form STZs. This is mirrored in the high yield stress observed in the stress-strain curve (Fig. 7.23). Moreover, more stored energy means that more STZs can be activated later at higher stresses which explain the observed improved plasticity (see Fig. 7.23). When the strain rate is decreased to $4\times10^7/s$ the total energy in the system

increases smoothly and achieves a maximum at a strain level of 9% when a dominant shear band form. At the yield point, due to the low amount of stored energy, a smaller number of STZs is activated than in the high strain rate case. Moreover, the slower deformation process allows the first activated STZs to percolate along the direction of maximum resolved shear stress to form a dominant shear band. Afterwards, the energy evolution shows a steep decline that correlates with the shear band propagation.

These findings are supported by the degree of the strain localization parameter $\psi$ as shown in Fig. 7.7(b). Here, $\psi$ is defined as $\psi = \sqrt{\frac{1}{N}\sum_{i=1}^{N}(\eta_i^{Mises} - \eta_{ave}^{Mises})^2}$, where $\eta_{ave}^{Mises}$ is the average von Mises strain over all atoms in the whole simulation box [48, 63]. A larger $\psi$ value indicates larger variations in the atomic strain and a more localized deformation mode. Up to a strain level of 6% there is almost no difference in the $\psi$ value for the two strain rates which means that the strain rate does not affect the elastic properties of MGs. However, during yielding, the high strain rate deformation shows lower $\psi$ values that increase smoothly during loading indicating a homogeneous deformation process. Otherwise, the deformation at low strain rate shows large fluctuation in the $\psi$ value when a dominant shear band forms and propagates through the structure.

The transition in the deformation behavior with the strain rate is driven by time-dependent relaxation processes. Amorphous materials exhibit a local $\beta$-relaxation and a cooperative $\alpha$-relaxation that can be connected to the two mechanically activated processes such as STZ activation and shear-banding, respectively[64, 65]. While $\beta$-relaxation (STZ activation) can bust instantaneously, the $\alpha$-relaxation process occurs on longer time scales over which STZs percolate and SBs form. For deformation at high strain rates, there is no clear distinction between the two relaxation mechanisms while the degree of strain localization scales nearly linearly with the applied strain (Fig. 7.7). In this case, one can surmise that the percolation process is basically suppressed. However, at low strain rate the system has time to relax and two relaxation signatures can be observed. Already in the elastic regime, at a strain level of around 6% (when the two lines in Fig. 7.7(b) split), the $\beta$-relaxation mechanism set in and the first STZs activate, followed by the $\alpha$-relaxation when the STZs percolate and a dominant SB form ($\approx$9% strain).

Şopu et al.[23, 32] proposed an atomic mechanism of shear band nucleation and propagation, suggesting that the shear band formation process entails two main units: entities characterized by strong strain and vortex-like (rotating) structures. The vortex can be seen as the driving force to activate the next STZ during the percolation process. Hence, analysis of the rotation field is of primary importance for understanding the complex mechanism of the STZ

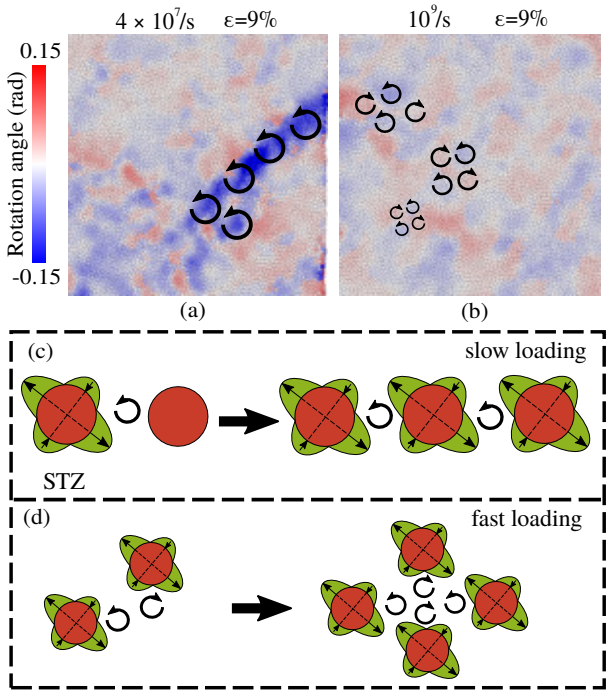


**Figure 7.8:** Atomic deformation mechanism resolved by the STZ-rotation unit. (a) and (c): At low strain rate deformation, the first STZs activates close to the surface of the sample while the connected rotation field activates the next STZ. The reiteration of these STZ-vortex unit events facilitates shear-band nucleation and propagation. (b) and (d): Many STZs with low atomic shear strain can be activated simultaneously and interact with each other through the rotation fields. Vortices of different rotation directions (clockwise and counterclockwise rotation represented by red and blue colors, respectively) hinder STZ percolation and prevent formation of a dominant shear band.

percolation process. Here, the vortexes are identified by analyzing the rotational part of the deformation gradient tensor and the results are presented in Fig. 7.8. In the sample deformed at low strain rate, the initial STZs are activated at the geometrical unfavorable motifs or regions of high stress. The Eshelby-like rotation field generated around the STZ will promote the activation of the next STZ and this kind of chain-like mechanism contributes to shear band nucleation and propagation throughout the sample (see Fig. 7.8(a) and (c)). In contrast, in the fast deformed MG, a much higher amount of elastic energy is injected into the structure within a short period resulting in the activation of a larger number of STZs. In this case, the STZ-rotation chain reaction process is constrained by the interaction between vortices of different rotation directions that eventually will cancel each other and diminishes the rotation field. (Fig. 7.8(b) and (d)). Due to this competing mechanism, STZs are difficult to assemble with each other and percolate to form a shear band. Moreover, the lack of energy release (blue curve in Fig. 7.7(a)), that usually take place during shear-band formation, results in the activation of even a higher number of STZs and, therefore, leads to even a more complex interactions and a low probability for strain localization. This scenario is supported by the monotonic increase in the

average atomic strain and the absolute value of the rotation angle during the loading process, as can be seen from Fig. 7.9. The rotation angle is almost equal to the atomic strain since the rotation field only relates to the activation of STZ. A further increase in the rotation and the atomic strain is restricted to the percolation process. Accordingly, at low strain rate deformation, when STZs can percolate and gradually develop into a shear band, a sudden increment of the average atomic strain and rotation will follow (Fig. 7.8(c)). In addition, a clear difference between the magnitude of atomic strain and rotation angle is observed that is attributed to local heating and viscous flow during the shearing process that perturbs the STZ-vortex sequence.

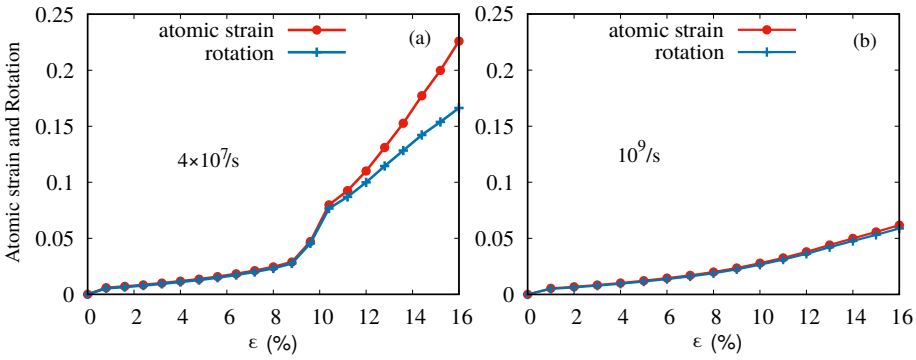


**Figure 7.9:** Relationship between average atomic strain and the average absolute value of the rotation. (a): The average atomic strain and rotation significantly increase at a strain level of 9%. (b): Because of the competition mechanism between the neighboring STZs and rotations, the average atomic strain and rotation increase monotonically and no sharp increase can be found even when the strain level approaches 16%.

In experiments, a brittle-to-ductile transition is usually observed with decreasing strain rate[10, 66]. Uniform elongation of a MGs nanowire was observed at low strain rate[67]. However, the difference between the strain rates used in these experiments and in MD simulations is ten orders of magnitude. At such a low strain rate thermally-activated driven processes induced structural relaxation that compensate for structural rejuvenation i.e STZ activation. Hence, the balance between the two processes (STZ activation vs. local $\beta$-relaxation process) delays the onset of catastrophic shear. In the MD time scale the thermally-activated relaxation (diffusional atomic rearrangement) is suppressed while the number of STZs (the degree of rejuvenation) increase with the applied strain rate.

## 5. Conclusion

In summary, the effects of cooling rate, temperature, and strain rate on the tensile deformation behavior of $Cu_{64}Zr_{36}$ metallic glass have been investigated. An improved ductility can

be induced by increasing cooling rate, temperature and strain rate.

1. A high cooling rate affects the atomic structure of the glass and leads to a higher degree of disorder corresponding to a low density of close packed Cu-centered full icosahedra. Sampling of the saddle points on the potential energy surface reveals that the activation energy barriers for local atomic rearrangements decrease with increasing cooling rate. Consequently, when deforming less ordered MGs, quenched at high cooling rates, a large number of homogeneously dispersed STZs get activated resulting in a more homogeneous deformation.

2. At high temperatures, although the local structure does not suffer important variations, the increase in the kinetic energy allows the atoms to easily overcome the activation energy barriers for rearrangement and hence, raises the probability for thermal activation of STZs.

3. By deforming at high strain rates a large amount of energy is stored in a short time in the material, resulting in large number of STZ events when yielding starts. The competing interaction of the homogeneous network of STZs through the two-unit STZ-vortex mechanism restricts STZ percolation and the formation of one dominate shear band.

Thus, the brittle-to-ductile transition of MGs can be promoted by controlling the STZ activation process. A large number of STZs and, consequently, improved plasticity can be achieved, to the same extent, by thermal treatment, enhancing thermal vibrations or injecting energy into the glassy structure.

**Acknowledgements** The authors acknowledge financial support by the China Scholarship Council (CSC, 201806220096), the Deutsche Forschungsgemeinschaft (DFG) (Grant no. SO 1518/1-1) and the European Research Council under the ERC Advanced Grant INTELHYB (Grant no. ERC-2013-ADG-340025). The authors are grateful for the computing time granted by the Lichtenberg high performance computer of the Technische Universität Darmstadt and the high performance cluster of the Montanuniversität Leoben.

**Data availability** The data that support the findings of this study are available from the corresponding author upon reasonable request.

## References


[1] W.-H. Wang, C. Dong, and C. Shek, "Bulk metallic glasses," Materials Science and Engineering: R: Reports **44**, 45–89 (2004).

[2] S. Scudino, H. Shakur Shahabi, M. Stoica, I. Kaban, B. Escher, U. Kühn, G. Vaughan, and J. Eckert, "Structural features of plastic deformation in bulk metallic glasses," Applied Physics Letters **106**, 031903 (2015).

[3] S. Feng, L. Qi, G. Li, and R. Liu, "Molecular dynamics simulation of structural characterization of elastic and inelastic deformation in zrcu metallic glasses," Journal of Nanomaterials **2014** (2014).

[4] T. C. Hufnagel, C. A. Schuh, and M. L. Falk, "Deformation of metallic glasses: Recent developments in theory, simulations, and experiments," Acta Materialia **109**, 375–393 (2016).

[5] A. Greer, Y. Cheng, and E. Ma, "Shear bands in metallic glasses," Materials Science and Engineering: R: Reports **74**, 71–132 (2013).

[6] C. Zhong, H. Zhang, Q. Cao, X. Wang, D. Zhang, U. Ramamurty, and J. Jiang, "Deformation behavior of metallic glasses with shear band like atomic structure: a molecular dynamics study," Scientific reports **6**, 30935 (2016).

[7] Z. Zhang, J. Eckert, and L. Schultz, "Difference in compressive and tensile fracture mechanisms of zr59cu20al10ni8ti3 bulk metallic glass," Acta Materialia **51**, 1167–1179 (2003).

[8] A. Sergueeva, N. Mara, J. Kuntz, E. Lavernia, and A. Mukherjee*, "Shear band formation and ductility in bulk metallic glass," Philosophical Magazine **85**, 2671–2687 (2005).

[9] R. Conner, W. L. Johnson, N. Paton, and W. Nix, "Shear bands and cracking of metallic glass plates in bending," Journal of applied physics **94**, 904–911 (2003).

[10] J. Lu, G. Ravichandran, and W. L. Johnson, "Deformation behavior of the zr41. 2ti13. 8cu12. 5ni10be22. 5 bulk metallic glass over a wide range of strain-rates and temperatures," Acta materialia **51**, 3429–3443 (2003).

[11] K. Albe, Y. Ritter, and D. Şopu, "Enhancing the plasticity of metallic glasses: Shear band formation, nanocomposites and nanoglasses investigated by molecular dynamics simulations," Mechanics of Materials **67**, 94–103 (2013).

[12] M. Jafary-Zadeh, R. Tavakoli, J. Koh, Z. Aitken, and Y.-W. Zhang, "Effect of chemical composition and affinity on the short-and medium-range order structures and mechanical properties of zr-ni-al metallic glass," Journal of Non-Crystalline Solids **456**, 68–75 (2017).

[13] J. Shen, Y. Huang, and J. Sun, "Plasticity of a ticu-based bulk metallic glass: Effect of cooling rate," Journal of Materials Research **22**, 3067–3074 (2007).

[14] C. Meduri, M. Hasan, S. Adam, and G. Kumar, "Effect of temperature on shear bands and bending plasticity of metallic glasses," Journal of Alloys and Compounds **732**, 922–927

(2018).
[15] S. Song, J. Jang, J. Huang, and T. Nieh, "Inhomogeneous to homogeneous transition in an au-based metallic glass and its deformation maps," Intermetallics **18**, 702–709 (2010).
[16] L. Chen, A. Setyawan, H. Kato, A. Inoue, G. Zhang, J. Saida, X. Wang, Q. Cao, and J. Jiang, "Free-volume-induced enhancement of plasticity in a monolithic bulk metallic glass at room temperature," Scripta Materialia **59**, 75–78 (2008).
[17] A. Bhattacharyya, G. Singh, K. E. Prasad, R. Narasimhan, and U. Ramamurty, "On the strain rate sensitivity of plastic flow in metallic glasses," Materials Science and Engineering: A **625**, 245–251 (2015).
[18] I.-C. Choi, Y. Zhao, B.-G. Yoo, Y.-J. Kim, J.-Y. Suh, U. Ramamurty, and J.-i. Jang, "Estimation of the shear transformation zone size in a bulk metallic glass through statistical analysis of the first pop-in stresses during spherical nanoindentation," Scripta Materialia **66**, 923–926 (2012).
[19] I.-C. Choi, Y. Zhao, Y.-J. Kim, B.-G. Yoo, J.-Y. Suh, U. Ramamurty, and J.-i. Jang, "Indentation size effect and shear transformation zone size in a bulk metallic glass in two different structural states," Acta materialia **60**, 6862–6868 (2012).
[20] A. Argon, "Plastic deformation in metallic glasses," Acta metall. **27**, 47–58 (1979).
[21] A. Argon, "Mechanisms of inelastic deformation in metallic glasses," Journal of Physics and Chemistry of Solids **43**, 945–961 (1982).
[22] A. Argon and L. T. Shi, "Development of visco-plastic deformation in metallic glasses," Acta Metallurgica **31**, 499–507 (1983).
[23] D. Şopu, A. Stukowski, M. Stoica, and S. Scudino, "Atomic-level processes of shear band nucleation in metallic glasses," Physical review letters **119**, 195503 (2017).
[24] C. Packard and C. Schuh, "Initiation of shear bands near a stress concentration in metallic glass," Acta Materialia **55**, 5348–5358 (2007).
[25] A. Hirata, P. Guan, T. Fujita, Y. Hirotsu, A. Inoue, A. R. Yavari, T. Sakurai, and M. Chen, "Direct observation of local atomic order in a metallic glass," Nature materials **10**, 28–33 (2011).
[26] H. Sheng, W. Luo, F. Alamgir, J. Bai, and E. Ma, "Atomic packing and short-to-medium-range order in metallic glasses," Nature **439**, 419–425 (2006).
[27] M. Kbirou, S. Trady, A. Hasnaoui, and M. Mazroui, "Short and medium-range orders in co3al metallic glass," Chemical Physics **513**, 58–66 (2018).
[28] A. Foroughi, R. Tavakoli, and H. Aashuri, "Molecular dynamics study of structural formation in cu50–zr50 bulk metallic glass," Journal of Non-Crystalline Solids **432**, 334–341 (2016).
[29] D. Şopu, C. Soyarslan, B. Sarac, S. Bargmann, M. Stoica, and J. Eckert, "Structure-property relationships in nanoporous metallic glasses," Acta materialia **106**, 199–207

(2016).
[30] C. Peng, D. Şopu, Y. Cheng, K. Song, S. Wang, J. Eckert, and L. Wang, "Deformation behavior of designed dual-phase cuzr metallic glasses," Materials & Design **168**, 107662 (2019).
[31] H. Song, S. Li, Y. Zhang, Q. Deng, T. Xu, and Y. Li, "Atomic simulations of plastic deformation behavior of cu50zr50 metallic glass," Journal of Non-Crystalline Solids **471**, 312–321 (2017).
[32] D. Şopu, S. Scudino, X. Bian, C. Gammer, and J. Eckert, "Atomic-scale origin of shear band multiplication in heterogeneous metallic glasses," Scripta Materialia **178**, 57–61 (2020).
[33] S. Plimpton, "Fast parallel algorithms for short-range molecular dynamics," Journal of computational physics **117**, 1–19 (1995).
[34] V. Borovikov, M. I. Mendelev, and A. H. King, "Effects of stable and unstable stacking fault energy on dislocation nucleation in nano-crystalline metals," Modelling and Simulation in Materials Science and Engineering **24**, 085017 (2016).
[35] M. J. Mees, G. Pourtois, E. C. Neyts, B. J. Thijsse, and A. Stesmans, "Uniform-acceptance force-bias monte carlo method with time scale to study solid-state diffusion," Physical Review B **85**, 134301 (2012).
[36] F. Moitzi, D. Şopu, D. Holec, D. Perera, N. Mousseau, and J. Eckert, "Chemical bonding effects on the brittle-to-ductile transition in metallic glasses," Acta Materialia **188**, 273–281 (2020).
[37] A. Stukowski, "Visualization and analysis of atomistic simulation data with ovito–the open visualization tool," Modelling and Simulation in Materials Science and Engineering **18**, 015012 (2009).
[38] N. Mousseau, L. K. Béland, P. Brommer, J.-F. Joly, F. El-Mellouhi, E. Machado-Charry, M.-C. Marinica, and P. Pochet, "The activation-relaxation technique: Art nouveau and kinetic art," Journal of Atomic and Molecular Physics **2012** (2012).
[39] E. Cances, F. Legoll, M.-C. Marinica, K. Minoukadeh, and F. Willaime, "Some improvements of the activation-relaxation technique method for finding transition pathways on potential energy surfaces," The Journal of chemical physics **130**, 114711 (2009).
[40] G. Barkema and N. Mousseau, "Event-based relaxation of continuous disordered systems," Physical review letters **77**, 4358 (1996).
[41] C. Liu, P. Guan, and Y. Fan, "Correlating defects density in metallic glasses with the distribution of inherent structures in potential energy landscape," Acta Materialia **161**, 295–301 (2018).
[42] Y. Fan, T. Iwashita, and T. Egami, "Energy landscape-driven non-equilibrium evolution of inherent structure in disordered material," Nature communications **8**, 1–7 (2017).

[43] H. Kallel, N. Mousseau, and F. Schiettekatte, "Evolution of the potential-energy surface of amorphous silicon," Physical review letters **105**, 045503 (2010).
[44] D. Rodney and C. Schuh, "Distribution of thermally activated plastic events in a flowing glass," Physical review letters **102**, 235503 (2009).
[45] H. Guo, P. Yan, Y. Wang, J. Tan, Z. Zhang, M. Sui, and E. Ma, "Tensile ductility and necking of metallic glass," Nature materials **6**, 735–739 (2007).
[46] Y. Yokoyama, K. Fujita, A. R. Yavari, and A. Inoue, "Malleable hypoeutectic zr–ni–cu–al bulk glassy alloys with tensile plastic elongation at room temperature," Philosophical magazine letters **89**, 322–334 (2009).
[47] F. Li, H. Zhang, X. Liu, C. Yu, and Z. Lu, "Effects of cooling rate on the atomic structure of cu64zr36 binary metallic glass," Computational Materials Science **141**, 59–67 (2018).
[48] Y. Cheng, A. Cao, and E. Ma, "Correlation between the elastic modulus and the intrinsic plastic behavior of metallic glasses: The roles of atomic configuration and alloy composition," Acta Materialia **57**, 3253–3267 (2009).
[49] J. Yuan-Qi and P. Ping, "Electronic structures of stable cu-centered cu-zr icosahedral clusters studied by density functional theory," Acta Physica Sinica **67** (2018).
[50] Y. Cheng, A. J. Cao, H. Sheng, and E. Ma, "Local order influences initiation of plastic flow in metallic glass: Effects of alloy composition and sample cooling history," Acta Materialia **56**, 5263–5275 (2008).
[51] Y. Cheng, H. Sheng, and E. Ma, "Relationship between structure, dynamics, and mechanical properties in metallic glass-forming alloys," Physical Review B **78**, 014207 (2008).
[52] Y. Fan, T. Iwashita, and T. Egami, "Crossover from localized to cascade relaxations in metallic glasses," Physical review letters **115**, 045501 (2015).
[53] Y. Cheng and E. Ma, "Atomic-level structure and structure–property relationship in metallic glasses," Progress in materials science **56**, 379–473 (2011).
[54] H. Xu and M. Li, "Activation-relaxation technique study on $\beta$-relaxation in la55ni20al25 and cu46zr46al8 metallic glasses," Intermetallics **94**, 10–16 (2018).
[55] J. Ding, Y.-Q. Cheng, H. Sheng, M. Asta, R. O. Ritchie, and E. Ma, "Universal structural parameter to quantitatively predict metallic glass properties," Nature communications **7**, 1–10 (2016).
[56] K.-W. Park, C.-M. Lee, M. Wakeda, Y. Shibutani, M. L. Falk, and J.-C. Lee, "Elastostatically induced structural disordering in amorphous alloys," Acta materialia **56**, 5440–5450 (2008).
[57] C. Liu and R. Maaß, "Elastic fluctuations and structural heterogeneities in metallic glasses," Advanced Functional Materials **28**, 1800388 (2018).
[58] B. Shang, P. Guan, and J.-L. Barrat, "Elastic avalanches reveal marginal behavior in amorphous solids," Proceedings of the National Academy of Sciences **117**, 86–92 (2020).
[59] C. A. Schuh, T. C. Hufnagel, and U. Ramamurty, "Mechanical behavior of amorphous

alloys," Acta Materialia **55**, 4067–4109 (2007).
[60] C. Wang, Q. P. Cao, X. D. Wang, D. X. Zhang, U. Ramamurty, R. L. Narayan, and J.-Z. Jiang, "Intermediate temperature brittleness in metallic glasses," Advanced Materials **29**, 1605537 (2017).
[61] P. Cao, M. P. Short, and S. Yip, "Potential energy landscape activations governing plastic flows in glass rheology," Proceedings of the National Academy of Sciences **116**, 18790–18797 (2019).
[62] A. Greer and Y. Sun, "Stored energy in metallic glasses due to strains within the elastic limit," Philosophical Magazine **96**, 1643–1663 (2016).
[63] D. Şopu, X. Yuan, F. Moitzi, M. Stoica, and J. Eckert, "Structure–property relationships in shape memory metallic glass composites," Materials **12**, 1419 (2019).
[64] H. Yu, X. Shen, Z. Wang, L. Gu, W. Wang, and H. Bai, "Tensile plasticity in metallic glasses with pronounced $\beta$ relaxations," Physical review letters **108**, 015504 (2012).
[65] S. Mayr, "Activation energy of shear transformation zones: A key for understanding rheology of glasses and liquids," Physical review letters **97**, 195501 (2006).
[66] W. Ma, H. Kou, J. Li, H. Chang, and L. Zhou, "Effect of strain rate on compressive behavior of ti-based bulk metallic glass at room temperature," Journal of alloys and compounds **472**, 214–218 (2009).
[67] Q. Deng, Y. Cheng, Y. Yue, L. Zhang, Z. Zhang, X. Han, and E. Ma, "Uniform tensile elongation in framed submicron metallic glass specimen in the limit of suppressed shear banding," Acta materialia **59**, 6511–6518 (2011).

# Publication II

Scripta Materialia 212 (2022) 114575

Contents lists available at ScienceDirect

Scripta Materialia

journal homepage: www.elsevier.com/locate/scriptamat

## Maximizing the degree of rejuvenation in metallic glasses

X. Yuan[a], D. Şopu[a,b,*], F. Spieckermann[c], K.K. Song[d], S.V. Ketov[a], K.G. Prashanth[a,e,f], J. Eckert[a,c]

[a] Erich Schmid Institute of Materials Science, Austrian Academy of Sciences, Jahnstraße 12, Leoben A-8700, Austria
[b] Institut für Materialwissenschaft, Fachgebiet Materialmodellierung, Technische Universität Darmstadt, Otto-Berndt-Str. 3, Darmstadt D-64287, Germany
[c] Department of Materials Science, Chair of Materials Physics, Mountanuniversität Leoben, Jahnstraße 12, Leoben A-8700, Austria
[d] School of Mechanical, Electrical and Information Engineering, Shandong University (Weihai), Weihai 264209, China
[e] Department of Mechanical and Industrial Engineering, Tallinn University of Technology, Ehitajete tee 5, Tallinn 19086, Estonia
[f] CBCMT, School of Mechanical Engineering, Vellore Institute of Technology, Vellore, Tamil Nadu 632 014, India

ARTICLE INFO

*Article history:*
Received 12 November 2021
Revised 25 January 2022
Accepted 25 January 2022

*Keywords:*
Metallic glasses
Molecular dynamics simulations
Rejuvenation
Relaxation

ABSTRACT

As the reverse process of relaxation, rejuvenation is the structural excitation process that can bring metallic glasses (MGs) to a higher energy state and usually increases their free volume. Here, using a dilution procedure conducted by randomly removing atoms from the modeled glass matrix, the degree of rejuvenation can be systematically controlled and the maximum rejuvenation threshold of MGs is identified. The structural relaxation is activated during the rejuvenation process and the dynamic balance between free volume creation and annihilation defines the rejuvenation ability of MGs. The highest degree of rejuvenation correlates to the flow strain of the materials and the structure is similar to that found in shear bands.

Due to the existence of long-range disordered structure, MGs are thermodynamically in a metastable state and they would spontaneously convert to a lower energy state via aging (relaxation). Intriguingly, as-cast MGs can also undergo an energy increase process with the external energy injection which is called rejuvenation. Rejuvenation can be achieved by recovery annealing [1, 2] and faster quenching [3], thermal cycling [4], elastostatic and heavy plastic deformation [5–9], etc. As the inverse process of aging, rejuvenation can inspire the structure of MGs to restore flexibility with a significant increase of free volume and enthalpy [9–13]. In general, rejuvenation is accompanied by free volume generation but, in some conditions, such as compressive pressure-promoted thermally annealed, negative (compressive) volume strains of high-energy state were observed in well-ordered high-pressure glasses [14–16]. In this case, the local structure and the internal stress state of the MG are modulated [17].

Previous research has shown that rejuvenation is an effective way to improve the deformation behavior of MGs [5, 18] and now it is regarded as a promising approach for tuning the deformability of MGs and it has captured increasing attention due to its scientific significance. Both relaxation and rejuvenation processes are highly dependent on the MGs chemical composition, the initial energy state, and the non-uniformity of the original structure [19–21]. For example, cryogenic thermal cycling contributes to the apparent rejuvenation in $Zr_{55}Cu_{30}Al_{10}Ni_5$ but causes only an inconspicuous rejuvenation in $Pd_{42.5}Cu_{30}Ni_{7.5}P_{20}$ [22]. Furthermore, the rejuvenation degree of low-purity La-based MG is significantly higher than that of the high-purity La-based glassy system [23]. For La-based glassy system [4] it has been found that the rejuvenation is always followed by a relaxation process during cryogenic thermal cycling which may indicate the existence of a rejuvenation threshold in MGs. Despite the high amount of research reports on the rejuvenation topic, a systematic atomic-level analysis of the key factors that determine the degree of rejuvenation in MGs is still lacking.

Compared to the experimental limitation, molecular dynamics (MD) simulations give an effective way to study the atomic-scale processes in materials and provide useful insights into the rejuvenation and relaxation process of MGs [24, 25]. More interestingly, MD simulation allows the control of every single atom in the glass matrix, which provides a possible strategy to control the free volume that can be injected into the glassy matrix and, ultimately, contributes to the understanding of the links between local structure and atomic dynamics. Here, a systematic rejuvenation process is conducted to $Cu_{64}Zr_{36}$ MG by randomly diluting the system with the help of MD modeling. To reinforce and verify the results, we conducted similar simulations for a metal-metalloid $Pd_{35}Si_{65}$ glassy system. Finally, by analyzing the atomic dynamic behavior

and the structural variations during the rejuvenation process the rejuvenation threshold of MGs is identified.

For studying the rejuvenation behavior of MG, classical MD simulations were performed using the program package LAMMPS [26] and the python scripting interface. $Cu_{64}Zr_{36}$ and $Pd_{35}Si_{65}$ MGs consisting of 48,000 atoms with the dimensions of around $8 \times 8 \times 12$ nm $^3$ were used as a prototype materials. The interatomic interactions in the CuZr system were described by the Finnis-Sinclair-type potential developed by Mendelev et al. [27]. The PdSi system was simulated with hybrid interatomic potentials including the many-body potential Embedded Atom Method (EAM) [28] and Bond-Order potential [29] calculations. The initial liquid structures were quenched down from 2000 K to 50 K with a cooling rate of 0.01 k/s. The time step was set to 2 fs, constant pressure and temperature (NPT ensemble) were employed and periodic boundary conditions were applied in all three directions. After cooling down to 50 K, the systems were equilibrated for 1 ns to get the initial as-cast structures. The dilution process of the glass systems was conducted by randomly removing atoms from the initial as-cast structures and the dilution degree was represented by the percentage of atoms that are removed from the system. More than 7,000 steps of the removing procedure were applied to the sample and one atom was deleted at each step. A 10 ps relaxation was conducted after each time an atom was removed in order to equilibrate the structure. During the dilution process, the average atomic volume, the atomic displacement, and the fraction of Cu-centered Voronoi polyhedra were calculated and visualized with OVITO software [30] which includes an analysis modifier that calculates the Voronoi tessellation [31].

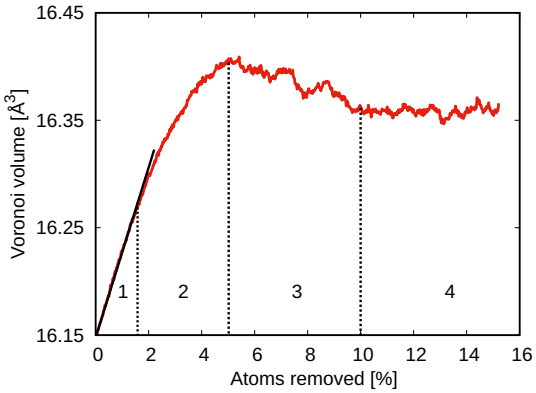


**Figure 7.10:** The evolution of Voronoi volume during the dilution process in $Cu_{64}Zr_{36}$ MG. The curve can be divided into four stages. During stage 1, the Voronoi volume increases linearly with increasing dilution level. After $\approx 2\%$ of atoms are removed from the glass matrix the Voronoi volume continues to increase but with a lower rate in stage 2. In stage 3 the average Voronoi volume starts to decrease and finally shows a steady state variation in stage 4.

By diluting the system by randomly removing atoms from the equilibrated glass matrix, free volume content increases which could be correlated to the rejuvenation of MGs. The free volume is defined as the Voronoi volume less the atomic core volume [10, 32]. As the atomic core volume is generally a constant value, the free volume is represented by the average atomic Voronoi volume in this work. As can be seen in Figure 7.17, four stages in the Voronoi volume evolution can be found during the dilution procedure of $Cu_{64}Zr_{36}$ MG. In the first stage, the effect of dilution increases linearly the average Voronoi volume, illustrating that the MG is rejuvenated and more and more free volume is retained in the glassy matrix. After removing $\approx 2\%$ of atoms, the Voronoi volume continues to increase but at a lower rate until $\approx 5\%$. With further removing atoms from the glass, contrary to the dramatic increase seen in stages 1 and 2, the Voronoi volume smoothly decreases in stage 3 and finally keeps a constant value in stage 4. Before the beginning of dilution, the atoms are densely packed in the equilibrated as-cast glass matrix. When removing atoms from the sample, one by one during stage 1, excess free volume is gradually injected into the glass and due to the generation of these vacancies, the neighbor atoms can locally start to rearrange trying to occupy the free space (see the inset in Figure 7.18). The upper row in Figure 7.18 shows the non-affine displacement magnitude of the atoms during dilution which is used to highlight the rearrangement of atoms. A slice with a width of 10 Å is chosen as an object and only the atoms with the displacement larger than 0.7 Å are shown here. Atoms with large non-affine strain or diffusional atomic arrangements with a mean square displacement distributed around 0.7 Å can be seen as the activation of $\beta$ relaxation [33].

Regarding relaxation processes, in general, glassy systems universally exhibit two main relaxations processes: the primary $\alpha$ and secondary $\beta$ relaxations. The $\alpha$ relaxation undergoes near the glass transition temperature (Tg) and diminishes below Tg [34, 35] and is associated with the large cooperative atomic mobility leading to irreversible viscous flow [36]. The $\beta$ relaxation, which initiates at high temperature and continues below Tg, has been linked to reversible local transitions of small chain-like groups of atoms [37, 38]. Although the time scales of MD simulations can not capture a long time thermal structural relaxation processes, the atomic rearrangements that are activated by the continuously generating free volume could resemble these thermal processes. Consequently, vacancy creation and the corresponding free volume generation accelerates the atoms and biases the structure towards a wide range of possible glassy states. Furthermore, it is assumed that structural relaxation could be well described by the same atomic-level movement such as the stress-driven shear transformation zone activation [33]. Consequently, thermal-, stress-, or even artificial-driven atomic rearrangements in

MGs should show similar characteristics.

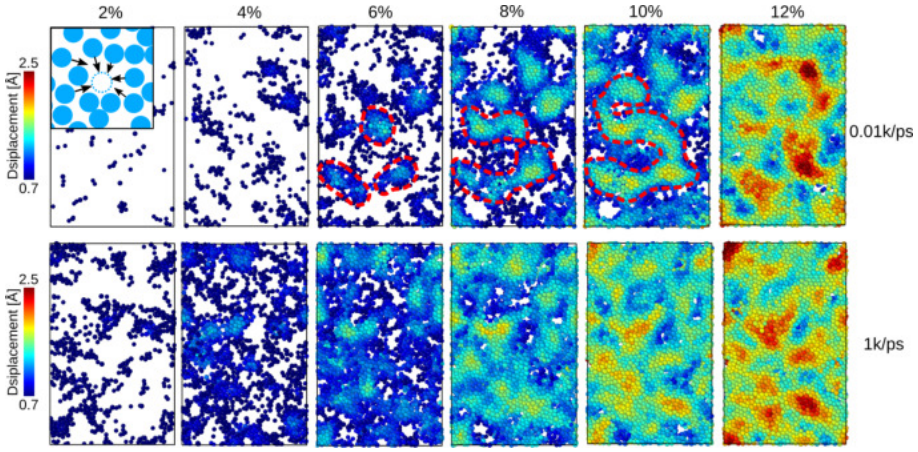


**Figure 7.11:** The atomic displacement magnitude of the system during the dilution process in $Cu_{64}Zr_{36}$ MG. Only those atoms with a displacement magnitude larger than 0.7 are shown.

As shown in Figure 7.17, a linear volume increase can be seen at the beginning of the dilution ($\approx 2\%$). At this stage, individual vacancies are created and only a few neighboring atoms are activated trying to close the vacancy while most of the free volume remains localized into the matrix (inset in Figure 7.18 upper panel). Under further dilution, the atomic rearrangement is highly localized, while in the meantime, the removal is randomly conducted in the whole sample, the free volume generation is much faster than its annihilation through vacancy squeezing. As atoms were further removed from the glass matrix, vacancies precipitates and clusters of atoms of high displacement start forming (Figure 7.18 upper panel, $4\%$) that could correlate to the initiation of $\beta$ relaxation. The clusters grow during dilution and string-like atomic rearrangement takes place as a result of the linkage of many highly localized rearrangements (Figure 7.18 upper panel, $6\% - 10\%$), which contributes to the deceleration of the $\beta$ relaxation [39] and the transition to $\alpha$ relaxation. At this point, the dynamic behavior of the system changes from rejuvenation domination to a complex rejuvenation-relaxation competing mode. As the dilution process further continues, a complete transition from $\beta$ to $\alpha$ relaxations occur resulting in a homogeneous atomic rearrangement related to a macroscopic viscous flow (Figure 7.18 upper panel, $10\% - 12\%$). The local atomic hops finally develop into a long-range chain reaction, resulting in the dominant $\alpha$ relaxation behavior [39] when the atomic rearrangement can not be restricted locally anymore. The spatially homogeneous relaxation corresponds to the presence of "mobile" atoms in the glass matrix. Hence, although atoms are still removed from the sample (free volume continue to be generated), the "mobile" atoms will fill the vacancy place immediately that leads, in the end, to the dynamic balance between free volume creation

and annihilation. This is reflected in the constant variation of the Voronoi volume in Figure 7.17, stage 4. During the final stage of dilution, a steady fluctuation in the Voronoi volume illustrates that no more free volume can be injected into the sample and the glassy structure can not be further rejuvenated. Based on the results, one may reasonably assume that the MGs can not be rejuvenated unlimitedly and the threshold for rejuvenation can be found. In order to prove this, the same dilution procedure is applied to another CuZr MG with the same chemical composition but produced at a much higher cooling rate of 1 k/ps. With increasing the cooling rate a higher amount of free volume is frozen into the glassy structure resulting in an overall increase of Voronoi volume, $\Delta$ V $\approx 0.5\%$ (see Figure 7.19 a). Although the two as-cast MGs show different average Voronoi volume, after dilution, both structures have the same density which means the same degree of rejuvenation. Additionally, comparing the Voronoi volume variation during the dilution process for the two samples one could see that stage 2, observed in the slower cooled MG, did not appear in the curve of the MG prepared at a higher cooling rate (see Figure 7.19 a). The non-affine displacement magnitude of the atoms during dilution for the faster cooled sample is analyzed and shown in Figure 7.18, lower panels. As we discussed above, an obvious trend of the transition from highly localized $\beta$ relaxations to homogeneous $\alpha$ relaxation can be found during the dilution process of the more relaxed sample. In this case, the clustered excess free volume resulted from the vacancy formation during first stage of dilution is confined by the elastic matrix that results in an average Voronoi volume higher than that observed at a later stage of the dilution process (stage 3). Contrary to the case seen in the lower cooled sample, a more homogeneous atomic rearrangement is activated at the very early stage of the dilution process for the faster cooled MG. In this case, at 4% of dilution, the $\alpha$ relaxation (homogeneous flow) is already activated while at 6% of dilution total homogeneous atomic motion can be found. The early activation of $\alpha$ relaxation can lead to a balance between free volume creation and annihilation and no more excess free volume can be injected into the glass matrix. Hence, after 4% dilution the average Voronoi volume holds a constant value during the entire dilution process (Figure 7.19 a). A similar trend was observed for the potential energy. The potential energy of the two samples increases during the rejuvenation process and converges to the same value that remains constant in stage 4. Further details about potential energy evolution are presented in the Supplemental Material, Sec. S1.

In order to further elucidate the physical reason for the different rejuvenation behavior of the two as-cast MGs during dilution, we also compared the Voronoi volume variation with the flow strain of these two samples under the uniaxial tensile test (Figure 7.19 b). Previously, it has

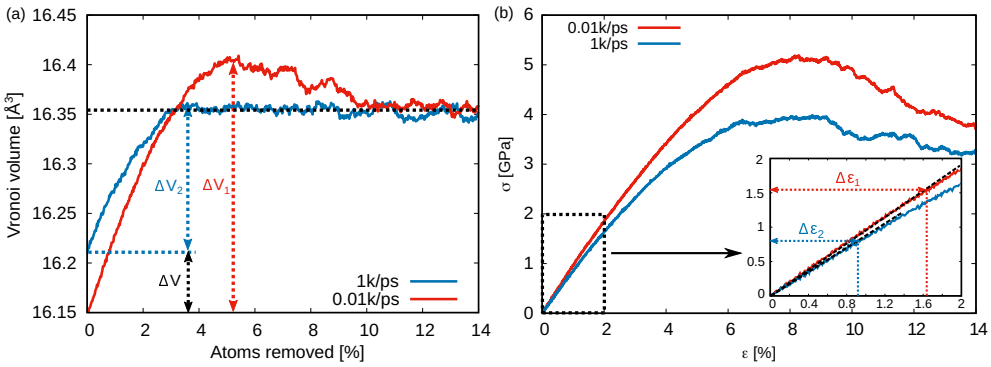


**Figure 7.12:** (a) The evolution of Voronoi volume during the dilution process for the samples with the cooling rate of 1k/ps. The result for the sample with 0.01k/ps cooling rate is also shown here for comparison. (b) The stress-strain curves of the slower cooled and higher cooled samples for the uniaxial tensile tests.

been shown that the excess free volume that could be stabilized within the glass-glass interfaces in nanoglasses depends on the flow strain of the material [40]. From the linear extrapolation of the stress-strain curves of the two samples, an flow strain of $\Delta\ \epsilon_1 \approx 1.6\%$ for the slower cooled MG and of $\Delta\ \epsilon_2 \approx 0.9\%$ for the faster cooled one can be found. Interestingly, if we compare these values with the Voronoi volume variation during the dilution process and translate the volume increment to the flow strain, a striking agreement relationship can be found. For the slower cooled sample, the Voronoi volume increases almost $1.6\%$ (see Figure 7.19 a, $\Delta\ V_1$) to the maximum value during dilution, which well matches the linearly elastic strain of $1.6\%$ in the stress-strain curve. Similarly, a $\Delta\ V_2 \approx 0.9\%$ increase of Voronoi volume for the faster cooled sample is in excellent agreement with the $0.9\%$ value of the flow strain. A similar correlation is also found for a metal-metalloid $Pd_{35}Si_{65}$ alloy. However, due to the high fraction of rigid covalent Si-Si bonds, the atomic rearrangement is less pronounced during the dilution process [41] and, hence, the Voronoi volume can increase up to $\approx 4\%$. Also, this value matches well the flow strain of $Pd_{35}Si_{65}$ MG (for details see Supplemental Material, Sec. S2).

One should mention at this stage that all these values correspond to a homogeneous rejuvenation process where the whole volume of the glass is perturbed and hence, also the relaxation process is homogeneous. If one considers the case of a locally rejuvenation process, for instance, through irradiation with heavy ions [42, 43] the local affected zone will be confined by the elastic/unaffected matrix. In this case, we can expect higher rejuvenated states and consequently, higher excess free volume after the thermal spike relaxation process. When repeating the dilution simulations for the slower cooled $Cu_{64}Zr_{36}$ MG using an NVT ensemble (holding constant the volume of the sample) the amount of free volume injected into the system goes up to $12\%$ followed by free volume precipitation and voids formation (for details see Supplemental

Material, Sec. S3).

The dilution simulations that we conduct in this work prove the existence of the rejuvenation threshold for MGs. However, creating free volume by continuously removing atoms from the glass matrix is a highly artificial operation that is impossible to reproduce in experiments. Considering this limitation, we try to correlate the dilution process to a more pragmatic rejuvenation process, i.e. the shear bands formation in MGs [44]. Accordingly, a $Cu_{64}Zr_{36}$ MG sample consisting of 1,500,000 atoms was prepared following the same procedure used to prepare the structure for studying the dilution process. A uniaxial tensile test with a strain rate of $4 \times 10^{7}$ /s was conducted until $\varepsilon = 16\%$ when the system is plastically deformed and mature shear bands are already formed. The atoms with a shear strain higher than 0.2 [45] at $\varepsilon = 16\%$ are selected as shear band atoms (SB-atoms) and the Voronoi volume evolution of those atoms are calculated and shown in Figure 7.20 a, dashed line. The volume of SB-atoms is calculated after the deformed system is relaxed to zero stress at each strain level in order to exclude the elastic strain from the Voronoi volume calculation. Interestingly, as can be seen from Figure 7.20 a, the Voronoi volume of the SB-atoms shows a steady fluctuation after $\varepsilon = 12\%$ (when the SB formed), which is very close to the value at the final stage of the dilution process. This further illustrates that MG cannot be rejuvenated unlimitedly and even the density of the highly sheared material (SB-atoms) will not overcome the rejuvenation threshold.

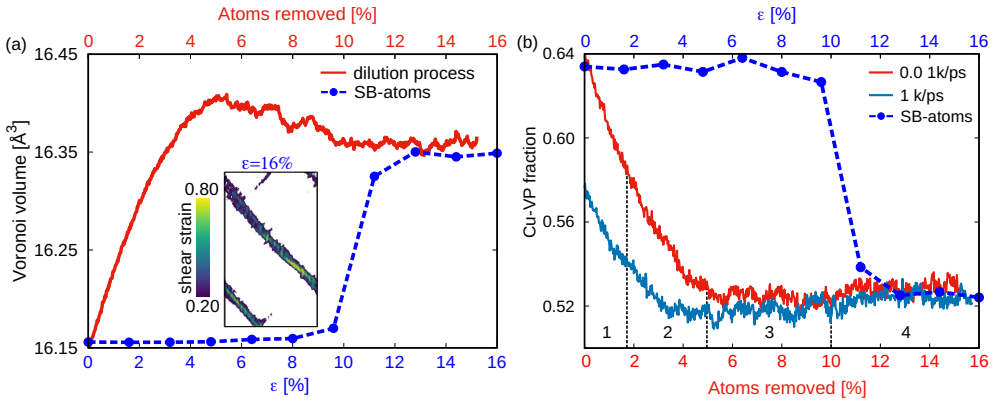


**Figure 7.13:** (a) The dashed line illustrates the evolution of the Voronoi volume of the SB-atoms during the uniaxial tensile deformation process of $Cu_{64}Zr_{36}$ MG. Inset shows the SB-atoms, only those atoms with a shear strain higher than 0.2 at $\varepsilon = 16\%$ are selected. The dilution process of the sample obtained at a cooling rate of 0.01k/ps is shown in the solid line for comparison. (b) The atomic structure evolution highlighted by Cu-VP during the dilution process of the two MGs prepared at different cooling rates. The fraction of Cu-VP of SB-atoms during tensile deformation is also monitored and shown in a dashed line for comparison.

MD simulations are of particular interest to characterize atomic structure in MGs. For the MGs in the present work, the relative populations of the Voronoi polyhedra are analyzed in order

to correlate the structure variation during the dilution process to the rejuvenation/relaxation mechanisms. The most five favored Cu-centered Voronoi polyhedra (Cu-VP) are chosen, treated as the fingerprint of short-range-order (SRO) in $Cu_{64}Zr_{36}$ MG [46], as representative structure parameter for the atomic-scale heterogeneity [10, 47–50]. In Figure 7.20 b, the population of the Cu-VP at different stages of dilution for the two $Cu_{64}Zr_{36}$ samples prepared at different cooling rates are shown. In the well-relaxed glass (low cooling rate), at the first two stages of dilution, the Cu-VP decreased from 63.5% to nearly 52%, indicating that the atomic structure evolved to a more disordered state due to the effect of structural rejuvenation. After, the fraction of Cu-VP remains constant in stages 3 and 4. Stage 4, as we mentioned above, corresponds to the $\alpha$ relaxation and viscous flow and the topological structure of MG resembles one of the supercooled states. The less relaxed glass, obtained at a higher quenching rate of 1k/ps shows a much lower fraction of Cu-VP( $\approx 57.5\%$). Under dilution, this value shows a slight decrease to $\approx 52\%$ and remains relatively constant after $4\%$ of dilution when the $\alpha$ relaxation activates (homogeneous flow). Additionally, the fraction of Cu-VP of the SB-atoms during the deformation process is monitored, only after the effect of elastic strain is removed (the deformed system is relaxed to zero stress at each strain level). One can see in Figure 7.20 b, dashed line, that the change of the fraction of Cu-VP of SB-atoms shows a steady evolution during the plastic deformation stage. Hence, SRO variations in shear bands correlate with the MG structure in the final stage of the dilution process, indicating that the diluted MGs and the shear band show a similar structural state corresponding to the highest degree of rejuvenation.

To summarize, in the present work by randomly removing atoms from monolithic MGs, the rejuvenation level was controlled and a threshold for rejuvenation was found. Vacancies creation allowed to generate free volume and disrupt the SRO and, consequently, to systematically rejuvenate MGs. In this way, by controlling the percentage of atoms that are homogeneously removed from the glass matrix four stages of dilution have been identified: (I) The linear increase in free volume correlates to individual vacancy formation. (II) The precipitation of vacancies allows for the relaxation of a small fraction of the free volume through local rearrangements or $\beta$ relaxation. (III) Once a high density of vacancies are created, enhancing the atomic mobility, the $\alpha$ relaxation counterbalances the rejuvenation process. (IV) Finally, with further dilution, a dynamic balance between free volume generation and annihilation is achieved and the "highest rejuvenated" state is found. The degree of excess free volume correlates to the yield flow of the material. Moreover, the SRO and the density of shear bands show similar values as found in the final stage of dilution. Basically, the structure of a shear band can be seen as the "high-

est rejuvenated" state. Furthermore, when a MG is only locally rejuvenated and the affected zone is confined by the elastic matrix the excess free volume and the corresponding degree of rejuvenation increase.

## Declaration of competing interest

The authors declare that they have no known competing financial interests or personal relationships that could have appeared to influence the work reported in this paper.

## Acknowledgments

The authors acknowledge financial support by the China Scholarship Council (CSC, 201806220096), the Deutsche Forschungsgemeinschaft (DFG) (Grant no. SO 1518/1-1), the European Research Council under the ERC Advanced Grant INTELHYB (Grant no. ERC-2013-ADG-340025) and the National Natural Science Foundation of China (51871132). The authors are grateful for the computing time granted by the Lichtenberg high performance computer of the Technische Universität Darmstadt.

## References


[1] J. Saida, R. Yamada, M. Wakeda, Appl. Phys. Lett. 103 (2013) 221910. doi:https://doi.org/10.1063/1.4835076.

[2] S. Küchemann, P. M. Derlet, C. Liu, D. Rosenthal, G. Sparks, W. S. Larson, R. Maaß, Adv. Funct. Mater. 28 (2018) 1805385. doi:https://doi.org/10.1002/adfm.201805385.

[3] M. Wakeda, J. Saida, J. Li, S. Ogata, Sci. Rep. 5 (2015) 1–8. doi:https://doi.org/10.1038/srep10545.

[4] S. Ketov, Y. Sun, S. Nachum, Z. Lu, A. Checchi, A. Beraldin, H. Bai, W. Wang, D. Louzguine-Luzgin, M. Carpenter, et al., Nature. 524 (2015) 200–203. doi:https://doi.org/10.1038/nature14674.

[5] J. Pan, Y. Wang, Q. Guo, D. Zhang, A. Greer, Y. Li, Nat. Commun. 9 (2018) 1–9. doi:https://doi.org/10.1038/s41467-018-02943-4.

[6] K.-W. Park, C.-M. Lee, M. Wakeda, Y. Shibutani, M. L. Falk, J.-C. Lee, Acta mater. 56 (2008) 5440–5450. doi:https://doi.org/10.1016/j.actamat.2008.07.033.

[7] A. Concustell, F. Méar, S. Surinach, M. Baró, A. Greer, Philos. Mag. Lett. 89 (2009) 831–840. doi:https://doi.org/10.1080/09500830903337919.

[8] W. Dmowski, Y. Yokoyama, A. Chuang, Y. Ren, M. Umemoto, K. Tsuchiya, A. Inoue, T. Egami, Acta Mater. 58 (2010) 429–438. doi:https://doi.org/10.1016/j.actamat.2009.09.021.

[9] G. Ding, C. Li, A. Zaccone, W. Wang, H. Lei, F. Jiang, Z. Ling, M. Jiang, Sci. Adv. 5 (2019) eaaw6249. doi:https://doi.org/10.1126/sciadv.aaw6249.

[10] S. Feng, K. Chan, L. Zhao, S. Pan, L. Qi, L. Wang, R. Liu, Mater. Design. 158 (2018) 248–255. doi:https://doi.org/10.1016/j.matdes.2018.08.040.

[11] J. Saida, R. Yamada, M. Wakeda, S. Ogata, Sci. Technol. Adv. Mater. 18 (2017) 152–162. doi:https://doi.org/10.1080/14686996.2017.1280369.

[12] S. Li, J. Zhang, Z. Sha, J. Alloys Compd. 848 (2020) 156597. doi:https://doi.org/10.1016/j.jallcom.2020.156597.

[13] Z. H. Mahmoud, H. Barazandeh, S. M. Mostafavi, K. Ershov, A. Goncharov, A. S. Kuznetsov, O. D. Kravchenko, Y. Zhu, J. Mater. Res. Technol. 11 (2021) 2015–2020. doi:https://doi.org/10.1016/j.jmrt.2021.02.025.

[14] T. Ge, C. Wang, J. Tan, T. Ma, X. Yu, C. Jin, W. Wang, H. Bai, J. Appl. Phys. 121 (2017) 205109. doi:https://doi.org/10.1063/1.4983017.

[15] C. Wang, Z. Yang, T. Ma, Y. Sun, Y. Yin, Y. Gong, L. Gu, P. Wen, P. Zhu, Y. Long, et al., Appl. Phys. Lett. 110 (2017) 111901. doi:https://doi.org/10.1063/1.4978600.

[16] N. Miyazaki, M. Wakeda, Y.-J. Wang, S. Ogata, Npj Comput. Mater. 2 (2016) 1–9.

doi:https://doi.org/10.1038/npjcompumats.2016.13.
[17] X. Yuan, D. Şopu, J. Eckert, Phys. Rev. B 103 (2021) L140107. doi:10.1103/PhysRevB.103.L140107.
[18] J. Pan, Y. P. Ivanov, W. Zhou, Y. Li, A. Greer, Nature. 578 (2020) 559–562. doi:https://doi.org/10.1038/s41586-020-2016-3.
[19] S. Kang, Q. Cao, J. Liu, Y. Tang, X. Wang, D. Zhang, I. Ahn, A. Caron, J. Jiang, J. Alloys Compd. 795 (2019) 493–500. doi:https://doi.org/10.1016/j.jallcom.2019.05.026.
[20] W. Guo, Y. Shao, J. Saida, M. Zhao, S. Lü, S. Wu, J. Alloys Compd. 795 (2019) 314–318. doi:https://doi.org/10.1016/j.jallcom.2019.04.340.
[21] S. V. Ketov, A. S. Trifonov, Y. P. Ivanov, A. Y. Churyumov, A. V. Lubenchenko, A. A. Batrakov, J. Jiang, D. V. Louzguine-Luzgin, J. Eckert, J. Orava, et al., NPG Asia Mater. 10 (2018) 137–145. doi:https://doi.org/10.1038/s41427-018-0019-4.
[22] W. Guo, J. Saida, M. Zhao, S. Lü, S. Wu, Mater. Sci. Eng. A. 759 (2019) 59–64. doi:https://doi.org/10.1016/j.msea.2019.05.019.
[23] S. Sohrabi, M. Ri, H. Jiang, L. Gu, P. Wen, Y. Sun, W. Wang, Intermetallics 111 (2019) 106497. doi:https://doi.org/10.1016/j.intermet.2019.106497.
[24] H.-B. Yu, R. Richert, K. Samwer, Sci. Adv. 3 (2017) e1701577. doi:https://doi/10.1126/sciadv.1701577.
[25] B. Shang, W. Wang, A. L. Greer, P. Guan, Acta Mater. 213 (2021) 116952. doi:https://doi.org/10.1016/j.actamat.2021.116952.
[26] S. Plimpton, J. Comput. Phys. 117 (1995) 1–19. doi:https://doi.org/10.1006/jcph.1995.1039.
[27] M. Mendelev, D. Sordelet, M. Kramer, J. Appl. Phys. 102 (2007) 043501. doi:https://doi.org/10.1063/1.2769157.
[28] H. W. Sheng, M. J. Kramer, A. Cadien, T. Fujita, M. W. Chen, Phys. Rev. B 83 (2011) 134118. URL: https://link.aps.org/doi/10.1103/PhysRevB.83.134118. doi:10.1103/PhysRevB.83.134118.
[29] J. Tersoff, Phys. Rev. B 38 (1988) 9902–9905. URL: https://link.aps.org/doi/10.1103/PhysRevB.38.9902. doi:10.1103/PhysRevB.38.9902.
[30] A. Stukowski, Model. Simul. Mater. Sci. Eng. 18 (2009) 015012. doi:https://doi.org/10.1088/0965-0393/18/1/015012.
[31] W. Brostow, M. Chybicki, R. Laskowski, J. Rybicki, Phys. Rev. B. 57 (1998) 13448. doi:https://doi.org/10.1103/PhysRevB.57.13448.
[32] Q.-K. Li, M. Li, Mater. Trans. 48 (2007) 1816–1821. doi:https://doi.org/10.2320/matertrans.MJ200785.
[33] D. Şopu, X. Yuan, F. Moitzi, F. Spieckermann, X. Bian, J. Eckert, Appl. Mater. Today. 22 (2021) 100958. doi:http://dx.doi.org/10.1016/j.apmt.2021.100958.
[34] J. C. Dyre, Rev. Mod. Phys. 78 (2006) 953. doi:https://doi.org/10.1103/

RevModPhys.78.953.
[35] H.-B. Yu, W.-H. Wang, K. Samwer, Mater. Today. 16 (2013) 183–191. doi:https://doi.org/10.1016/j.mattod.2013.05.002.
[36] S. Küchemann, R. Maaß, Scr. Mater. 137 (2017) 5–8. doi:https://doi.org/10.1016/j.scriptamat.2017.04.034.
[37] S. Swayamjyoti, J. F. Löffler, P. Derlet, Phys. Rev. B. 89 (2014) 224201. doi:10.1103/PhysRevB.89.224201.
[38] H. Teichler, J. Non-Cryst. Solids. 293 (2001) 339–344. doi:https://doi.org/10.1016/S0022-3093(01)00684-6.
[39] Q. Wang, S. Zhang, Y. Yang, Y. Dong, C. Liu, J. Lu, Nat. Commun. 6 (2015) 1–6. doi:https://doi.org/10.1038/ncomms8876.
[40] D. Şopu, K. Albe, Y. Ritter, H. Gleiter, Appl. Phys. Lett. 94 (2009) 191911. doi:https://doi.org/10.1063/1.3130209.
[41] F. Moitzi, D. Şopu, D. Holec, D. Perera, N. Mousseau, J. Eckert, Acta Mater. 188 (2020) 273–281. doi:https://doi.org/10.1016/j.actamat.2020.02.002.
[42] D. Magagnosc, R. Ehrbar, G. Kumar, M. He, J. Schroers, D. Gianola, Sci. Rep. 3 (2013) 1–6. doi:https://doi.org/10.1038/srep01096.
[43] D. Magagnosc, G. Kumar, J. Schroers, P. Felfer, J. Cairney, D. Gianola, Acta Mater. 74 (2014) 165–182. doi:https://doi.org/10.1016/j.actamat.2014.04.002.
[44] J. Pan, Q. Chen, L. Liu, Y. Li, Acta Mater. 59 (2011) 5146–5158. doi:https://doi.org/10.1016/j.actamat.2011.04.047.
[45] K. Albe, Y. Ritter, D. Şopu, Mech. Mater. 67 (2013) 94–103. doi:https://doi.org/10.1016/j.mechmat.2013.06.004.
[46] Y. Cheng, A. J. Cao, H. Sheng, E. Ma, Acta Mater. 56 (2008) 5263–5275. doi:https://doi.org/10.1016/j.actamat.2008.07.011.
[47] J. Ding, Y.-Q. Cheng, E. Ma, Acta mater. 69 (2014) 343–354. doi:https://doi.org/10.1016/j.actamat.2014.02.005.
[48] X. Yuan, D. Şopu, F. Moitzi, K. Song, J. Eckert, J. Appl. Phys. 128 (2020) 125102. doi:https://doi.org/10.1063/5.0020201.
[49] D. Şopu, S. Scudino, X. Bian, C. Gammer, J. Eckert, Scr. Mater. 178 (2020) 57–61. doi:https://doi.org/10.1016/j.scriptamat.2019.11.006.
[50] C. Peng, D. Şopu, Y. Cheng, K. K. Song, S. Wang, J. Eckert, L. Wang, Mater. Design. 168 (2019) 107662. doi:https://doi.org/10.1016/j.matdes.2019.107662.

# Supplementary Materials

### S1. Evolution of the potential energy during the dilution process for the $Cu_{64}Zr_{36}$ metallic glasses

The potential energy for two samples obtained at different cooling rates is calculated and shown in Fig. 7.14. The potential energy of both samples increases during the rejuvenation process. The early dilution procedure destroys the short range order (strong bonds) and pushes the system to a more disordered state and weaker atomic bonds which leads to the increase of potential energy. When the homogeneously activated $\alpha$ relaxation counterbalances the rejuvenation process, the potential energy of the two samples converges to the same value which is constant with further dilution. This confirms that the glass can not be rejuvenated anymore reaching the highest degree of rejuvenation.

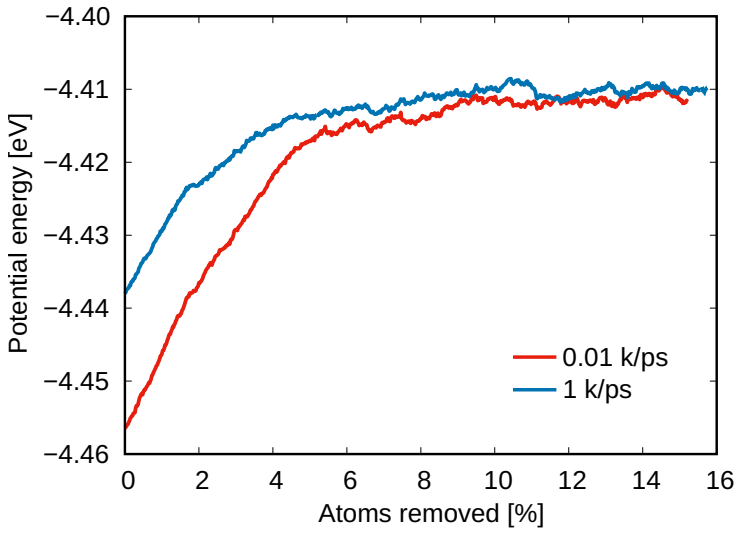


**Figure 7.14:** The change of potential energy during the dilution process for the $Cu_{64}Zr_{36}$ glassy system obtained at different cooling rates.

### S2. Dilution process for $Pd_{35}Si_{65}$ glassy system

A similar dilution process was conducted to the as-cast metal-metalloid $Pd_{35}Si_{65}$ glassy system and the Voronoi volume evolution was monitored and shown in Fig. 7.15 a. Due to a high fraction of rigid covalent Si-Si bonds, the atomic rearrangements become slower during the dilution process and hence, a larger fraction of Voronoi volume can be stabilized in the glass ($\Delta$ V $\approx 4\,\%$ ) This value correlates well with the value of the flow strain $\Delta\,\epsilon \approx 4\,\%$ of $Pd_{35}Si_{65}$ alloy (see Fig. 7.15 b).

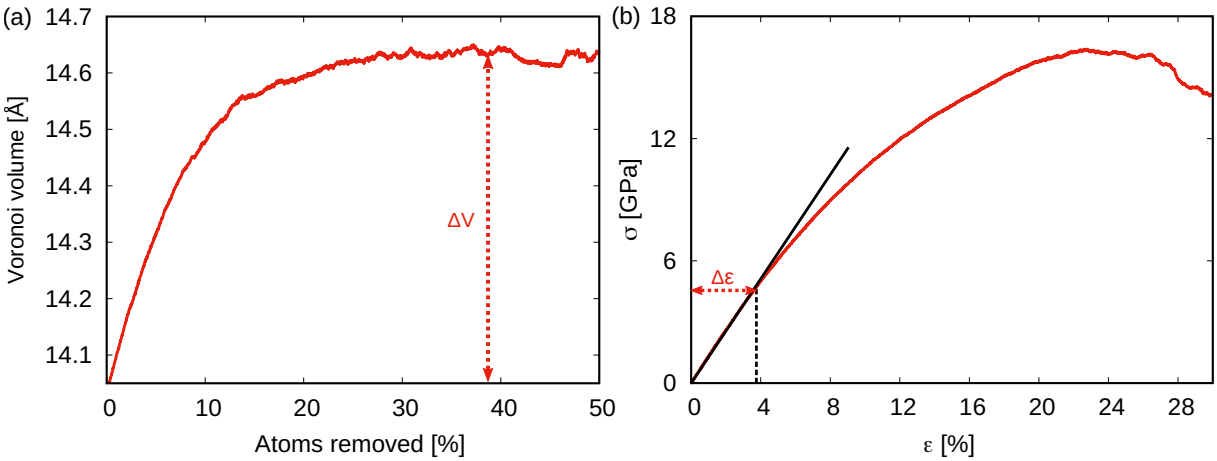


**Figure 7.15:** (a) The evolution of Voronoi volume during the dilution process for the $Pd_{35}Si_{65}$ glassy system. (b) The stress-strain curves of the as-cast sample for the uniaxial tensile test.

## S3. Voids formation during the dilution process of $Cu_{64}Zr_{36}$ glassy system

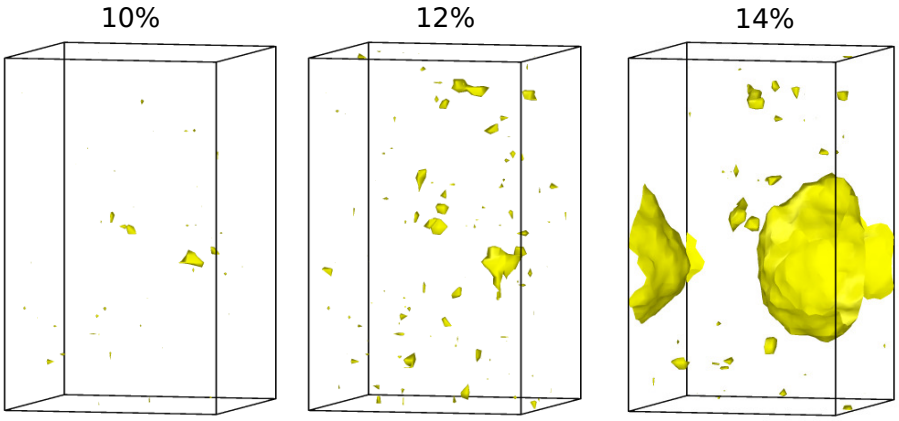


**Figure 7.16:** Vacancies percolation and voids formation in a simulation where the volume of the system stays constant. The voids are highlighted by the mesh surface.

Fig. 7.16 shows the dilution process of the as-cast $Cu_{64}Zr_{36}$ glassy system in a NVT ensemble (holding constant the volume of the sample). This simulation reproduces a local rejuvenation behavior when the affected zone is confined by the surrounding elastic matrix. In this case, the amount of free volume injected into the system goes up to 12%. The Voronoi volume of the structure corresponds to the density of the glass at an elevated temperature (in the order of the melting temperature). Once the excess free volume saturates, voids start forming by vacancies percolation.

# Publication III

*materials*

MDPI

*Article*

# Relaxation and Strain-Hardening Relationships in Highly Rejuvenated Metallic Glasses

**Xudong Yuan [1], Daniel Şopu [1,2,*], Kaikai Song [3] and Jürgen Eckert [1,4]**

[1] Erich Schmid Institute of Materials Science, Austrian Academy of Sciences, Jahnstraße 12, A-8700 Leoben, Austria; xudong.yuan@oeaw.ac.at (X.Y.); juergen.eckert@unileoben.ac.at (J.E.)
[2] Fachgebiet Materialmodellierung, Institut für Materialwissenschaft, Technische Universität Darmstadt, Otto-Berndt-Straße 3, D-64287 Darmstadt, Germany
[3] School of Mechanical, Electrical and Information Engineering, Shandong University (Weihai), Weihai 264209, China; songkaikai@sdu.edu.cn
[4] Department of Materials Science, Chair of Materials Physics, Montanuniversität Leoben, Jahnstraße 12, A-8700 Leoben, Austria
* Correspondence: daniel.sopu@oeaw.ac.at

check for updates

**Citation:** Yuan, X.; Şopu, D.; Song, K.; Eckert, J. Relaxation and Strain-Hardening Relationships in Highly Rejuvenated Metallic Glasses. *Materials* **2022**, *15*, 1702. https://doi.org/10.3390/ma15051702

Academic Editor: Łukasz Hawełek

Received: 31 December 2021
Accepted: 22 February 2022
Published: 24 February 2022

**Publisher's Note:** MDPI stays neutral with regard to jurisdictional claims in published maps and institutional affiliations.

**Abstract:** One way to rejuvenate metallic glasses is to increase their free volume. Here, by randomly removing atoms from the glass matrix, free volume is homogeneously generated in metallic glasses, and glassy states with different degrees of rejuvenation are designed and further mechanically tested. We find that the free volume in the rejuvenated glasses can be annihilated under tensile or compressive deformation that consequently leads to structural relaxation and strain-hardening. Additionally, the deformation mechanism of highly rejuvenated metallic glasses during the uniaxial loading–unloading tensile tests is investigated, in order to provide a systematic understanding of the relaxation and strain-hardening relationship. The observed strain-hardening in the highly rejuvenated metallic glasses corresponds to stress-driven structural and residual stress relaxation during cycling deformation. Nevertheless, the rejuvenated metallic glasses relax to a more stable state but could not recover their initial as-cast state.

**Keywords:** metallic glass; molecular dynamics simulations; rejuvenation; relaxation; strain-hardening

## 1. Introduction

Metallic glasses (MGs) are obtained by fast cooling from the melt to avoid crystallization and exhibit a disordered structure with higher-energy states [1–3]. As-cast MGs are thermodynamically metastable and can spontaneously convert to a lower energy state via aging (relaxation) [4, 5]. However, many strategies can push MGs to undergo an opposite process and reach a more disordered state which is called rejuvenation. Rejuvenation can be induced by reheating [6–8] and faster quenching [9], thermal cycling [10], elastostatic and heavy plastic deformation [11–15], irradiation [16], etc. Rejuvenation is an effective way to inspire the structure of MGs to restore flexibility with the increase of free volume and enthalpy [17–20] and it is regarded as a promising approach for tuning the deformability of MGs. It is now seen as a common way to improve the plasticity of MGs [11, 21] since it can ameliorate the highly localized deformation mechanism and could ultimately eliminate the formation of critical shear bands [7, 11]. Moreover, structural rejuvenation can also provide strain-hardening under certain loading conditions [21].

Although rejuvenation has captured increasing attention due to its scientific significance, the precise control of the degree of rejuvenation in MGs and the design of highly rejuvenated MGs is still a challenge in experimental work. Rejuvenation is usually associated with free volume accumulation that results to structural softening and hardness reduction. Strain softening is the Achilles' heel of MGs. While strain-hardening is familiar in polycrystalline metals, it is not found in most MGs [22, 23]. However, in some particular cases, strain-hardening has been also observed in monolithic MGs. Here, the suppression of shearing through size or geometric constraints, as demonstrated for nanosized samples [24, 25] or notched rods [26], may also lead to the apparent strain-hardening. Besides this, extreme rejuvenated MGs could even show strain-hardening that was associated with structural relaxation when loaded in uniaxial tension or compression which can be regarded as a return from the rejuvenated state [21]. Nevertheless, strain-hardening is evaluated with respect to the highly rejuvenated state and the structure never recovers the hardness of the initial as-cast state. Thus, a systematic understanding of the relationship between the degree of rejuvenation and deformation behavior in MGs is missing and an atomistic and mechanistic explanation for experimental observations is required. Additionally, the correlation between structural rejuvenation and the transition from strain-softening to strain-hardening behavior needs to be further studied. Compared to the limitation of the exper-

iment, molecular dynamics (MD) simulations provide useful insights into the rejuvenation and relaxation process of MGs [4, 27]. Moreover, MD simulations allows to quantitatively control the fraction of free volume into the glass matrix and, hence, provide a systematic strategy to manipulate the degree of rejuvenation in MGs [28].

In this work, we present MD computer simulations of the deformation behavior of MGs with a controlled degree of rejuvenation. Free volume is homogeneously introduced into the glass matrix by creating vacancies. Uniaxial tensile and compression tests are conducted and the deformation behavior of the rejuvenated glass systems was investigated in comparison to the as-cast MG. In addition, loading–unloading cycling tensile tests are simulated and the mechanism of strain-hardening in the highly rejuvenated MG is highlighted.

## 2. Simulation Details

### 2.1 Samples Preparation

For studying the mechanical properties of the rejuvenated MGs, classical MD simulations were performed using the program package LAMMPS [29] and the python scripting interface. A $Cu_{64}Zr_{36}$ glassy system of 48,000 atoms with the dimensions of around $8 \times 8 \times 12$ nm $^3$ was used as a prototype material. The system was relaxed at 2000 K for 2 ns to get the chemical homogeneity liquid and then quenched down to 50 K with a constant cooling rate of $10^{10}$ K/s. The constant pressure and temperature (NPT) ensemble were employed and periodic boundary conditions (PBCs) were applied in all three directions during the quenching process. The interatomic interactions were described by the modified Finnis–Sinclair type potential for CuZr binary alloys proposed by Mendelev et al. [30]. For all simulations a constant integration time step of 2 fs was used. After cooling down to 50 K, the system was equilibrated for 1 ns to get the stable initial as-cast MG structure. We homogeneously introduced free volume and systematically rejuvenate the as-cast MG system by applying a dilution procedure through vacancy creation presented in detail in our previous study [28]. In short, atoms are randomly removed from the initial as-cast structure and the degree of rejuvenation is represented by the percentage of atoms that are removed from the system. During the dilution process, the free volume evolution was analyzed to describe the structural state of the system.

### 2.2 Deformation Tests

In this work, uniaxial tensile and compressive tests were conducted to MGs with different de-

grees of rejuvenation. The temperature was controlled at 50 K using the NPT ensemble. PBCs are used in all three directions. Before loading, the samples are relaxed for 100 ps and all tests were performed under a constant engineering strain rate of $4 \times 10^{7}$/s. The loads were applied along $z$-direction while the stress in the other two directions is kept as zero. Additionally, recent experimental work has shown that compression-induced rejuvenation goes along with strain-hardening in mechanical deformation. In order to provide further analysis of strain-hardening in rejuvenated MG, loading-unloading cycling tensile tests were applied to the as-cast and highly rejuvenated glass samples that are designed by diluting the as-cast MG. At each cycle, the samples were loaded just before the yielding point and then were spontaneously unloaded to zero stress and further relaxed for 1 ns to get an equilibrium state. The evolution of the free volume and the atomic shear strain for each sample are visualized using the OVITO analysis and visualization software [31].

## 3. Results and Discussions

By randomly removing atoms from the as-cast glassy matrix, free volume content increases, which could be correlated to the rejuvenation of MGs [15]. The generation and annihilation of free volume during the dilution procedure were monitored and represented by the Voronoi volume variation which is calculated by the Voronoi tessellation method [19, 32, 33]. As shown in Figure 7.17a, four stages of Voronoi volume evolution can be found. In our previous work, the atomic-scale dynamic behavior of the system during the dilution process was investigated [28]. The Voronoi volume linearly increases during stage $I$ and slowly increase at stage $II$, illustrating that the free volume continues to be generated inside the glassy matrix during the dilution process [34]. Continuing to remove atoms from the system, the activation of $\beta$ relaxation and the transit to $\alpha$ relaxation corresponds to a decrease of Voronoi volume as observed in stage $III$. As enough atoms are removed from the glassy system, the dominant $\alpha$ relaxation behavior is activated and the competition between free volume creation and annihilation defines the dynamic balance in the Voronoi volume (Figure 7.17a stage $IV$). At this stage, the free volume can not be generated in the glassy matrix with further dilution and the rejuvenation reaches a threshold, which can be called the highly rejuvenated state.

It has been previously shown that structure rejuvenation in MGs is an effective strategy to tailor its mechanical properties [7, 15, 21, 35–37]. In order to investigate the mechanical properties of the MG systems with different degrees of rejuvenation, the deformation behavior

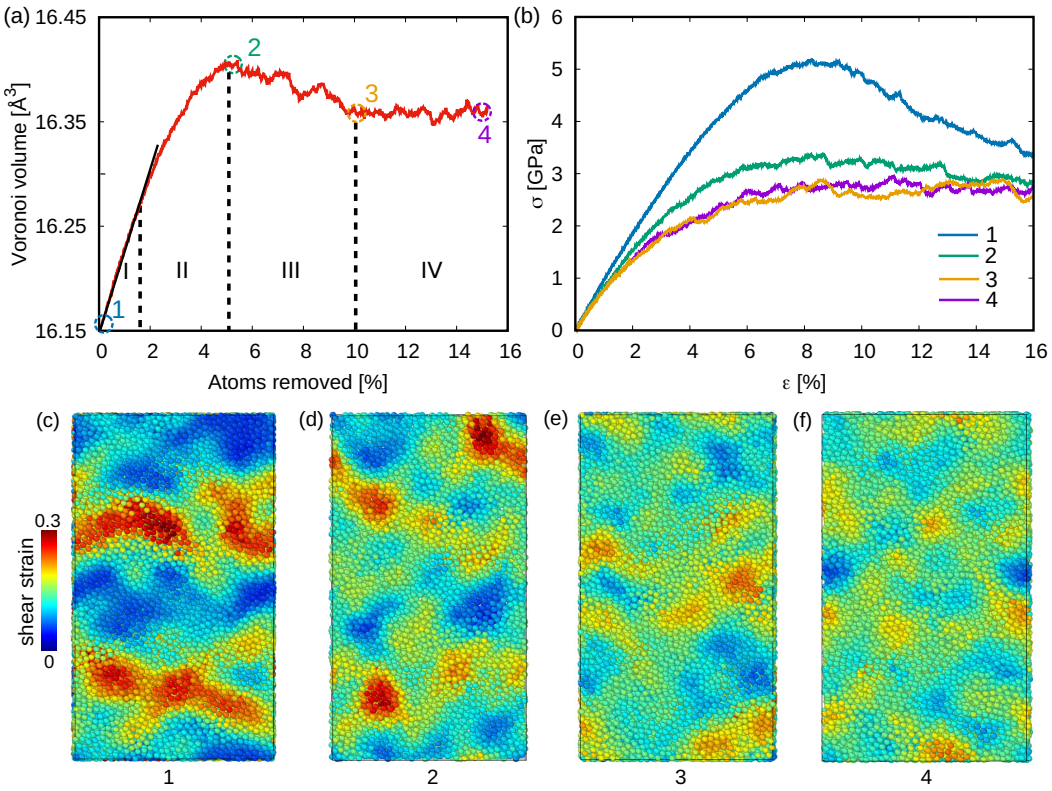


**Figure 7.17:** (**a**) The evolution of Voronoi volume during the dilution process. Four samples are picked up at different rejuvenation levels during the dilution process and are marked as sample 1, 2, 3 and 4. (**b**) Stress–strain curves for the four samples during tensile test. (**c**–**f**) The atomic strain map at the strain level of 16% for the four tested samples.

of MGs at different stages of dilution was tested under uniaxial tensile loading. Four samples which are picked from the glassy structure at a different dilution level are chosen as the loading objects (Figure 7.17a) and the results of the tensile tests are analyzed. Figure 7.17b shows the stress–strain curves of the four loaded samples where a clear strain softening effect can be seen from sample 1 to sample 4. The higher the rejuvenation level, the lower yield stress and the better plasticity the sample has. For sample 1, a sudden stress drop appears in the plastic deformation region of the stress–strain curve which indicates a strain-softening behavior of the as-cast glass and also reflects the tendency of a highly localized deformation (Figure 7.17c). The smooth slope in the stress–strain curve of sample 2 compared to sample 1 highlights a more homogeneous deformation mode. At this point, the $\beta$ relaxation is pronounced due to the excess free volume which can be associated with the activation of a large number of shear transformation zones (STZs) [38–40]. Due to the existence of earlier activated STZs, lower stress is needed for the formation of plastic zones, which finally leads to lower yield stress compared to sample 1. Nevertheless, the $\beta$ relaxation is the locally string-like dynamic behavior of atoms [38, 41, 42] and, hence, localized deformation can still be seen in sample 2, as highlighted in

Figure 7.17d. Finally, in sample 3 and sample 4, although these two tested systems are picked at different dilution levels, in both, the activated $\alpha$ relaxation is driven by atoms of high mobility. Eventually, a homogeneous deformation mechanism instead of localized shear deformation can be seen in these two samples (see Figure 7.17e,f).

The evolution of Voronoi volume with respect to tensile deformation for the four chosen samples is monitored and shown in Figure 7.18a. Not surprisingly, for sample 1, the Voronoi volume increases significantly with the applied external strain and remains higher even after removing the load indicating a deformation induced rejuvenation process [14, 43–46]. On the contrary, under tensile loading the other three samples with different degrees of rejuvenation (sample 2, sample 3 and sample 4) show initially a slight increase of the Voronoi volume corresponding to elastic stretching of the bonds. However, once the load is released, the Voronoi volume decreases resembling a relaxation process. A similar effect is observed when deforming in compression (see Figure 7.18b). The Voronoi volume in sample 1 decreases at the early stage of loading due to the system's elastic shrinkage and then increases indicating a deformation-induced free volume generation process (rejuvenation). It is worth noticing that the Voronoi volume of the rejuvenated samples always decreases during the compression process and, for sample 2, it can further decrease compared to samples 3 and 4 when the strain level overcomes 6%. As we mentioned above, samples 3 and 4 are highly rejuvenated MGs, and thus have lower yield stress compared to sample 2, and they can show homogeneous viscous flow without the formation of any localized shear bands during plastic deformation. Contrary to samples 3 and 4, sample 2 is in a more ordered state with a higher fraction of short-range order clusters (SRO) and also has higher contents of free volume (Figure 7.17a). This explains, on one hand, the higher Voronoi volume value before the compression test. On the other hand, a higher fraction of SRO means a higher yield stress that allows the system to compress (elastically deform) to a lower volume before yielding. The evaluation of Voronoi volume during deformation and unloading indicates that the as-cast MGs always rejuvenate under deformation while, on the contrary, the extreme rejuvenated systems exhibit constantly structural relaxation. Nevertheless, one should mention that there is still a marginal difference between the values of Voronoi volume after conducting tensile and compression cycling loading. After deformation, the glassy systems contain both elastic strains (expand/tensile strains and shrinkage/compressive strains) and plastic strains. When the applied stress is released, the elastic strains are mostly released but there are always some residual stresses confined into the glassy matrix [47].

Previous studies have shown that extreme rejuvenated MGs could even exhibit strain-

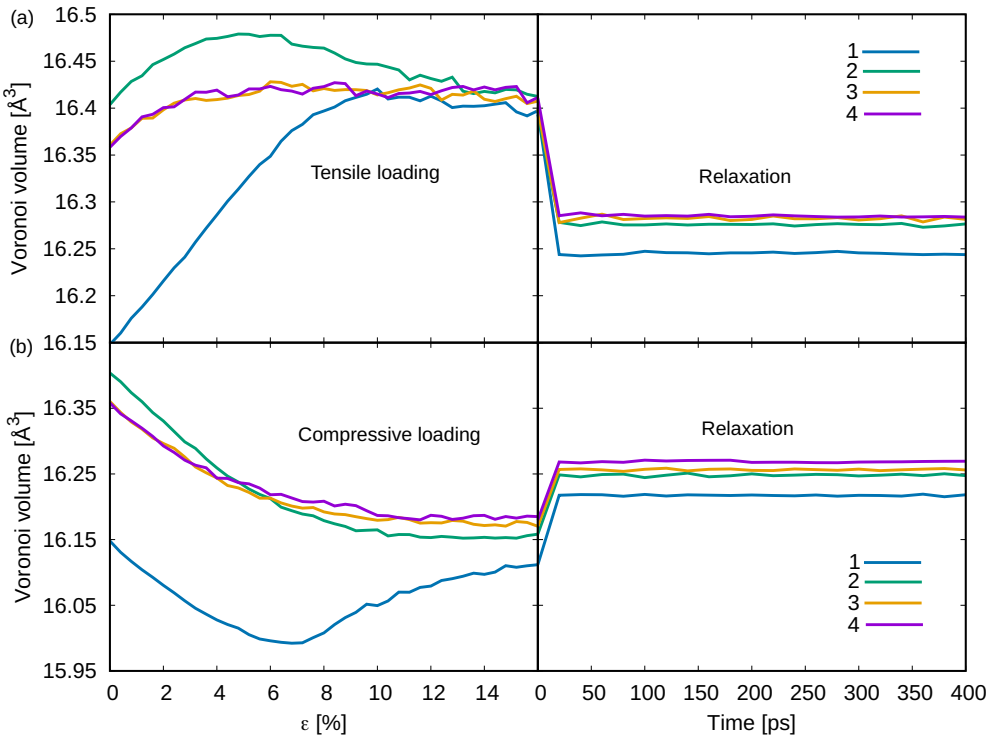


**Figure 7.18:** The Voronoi volume evolution for the four tested samples during (**a**) tensile and (**b**) compressive loading and during the unloading and relaxation processes.

hardening when loaded in uniaxial tension or compression [21]. Hence, we correlate the return from the rejuvenation states during loading to the experimentally observed strain-hardening. To do this, the highly rejuvenated MG (sample 4) is uniaxially deformed before yielding, and is then unloaded-reloaded several times. The same deformation process was applied to the as-cast MG (sample 1) for comparison. Figure 7.19 shows the stress–strain curves of the cycling tensile tests for the two samples. As expected, the stress–strain curves in Figure 7.19a indicate that the yield stress of sample 1 keeps a constant value at each reloading. Contrary to sample 1, Figure 7.19b shows that the yield stress of sample 4 gets higher on successive loadings, which indicates strain-hardening. As we discussed above, the rejuvenated MG exhibits relaxation during cycling deformation, which could be the reason for the observed strain-hardening. In order to prove this, the Voronoi volume evolution during the whole process for the two samples is monitored and shown in Figure 7.20. During each time of loading, the Voronoi volume of sample 1 linearly increases due to the elastic expansion caused by the applied stress. After releasing the applied stress, the volume can immediately decrease to its unloaded value. No extra free volume generation or annihilation after each cycle is observed indicating no structural fluctuations. As for sample 4, the Voronoi volume also increases with the applied stress during reloading. However, it is worth noting that at each time of unloading stage, the Voronoi volume can decrease

to a lower value compared to its last unloaded state, which reveals a stress-driven relaxation behavior. Under given deformation conditions, an MG can approach a steady-state energy [7]. The highly rejuvenated MG has a higher initial energy state and contains a higher fraction of free volume (see Figure 7.17a) compared to the as-cast MG. The excess free volume could be released via a stress-driven relaxation turning to a more stable state that, in the end, causes the observed strain-hardening behavior in highly rejuvenated MG.

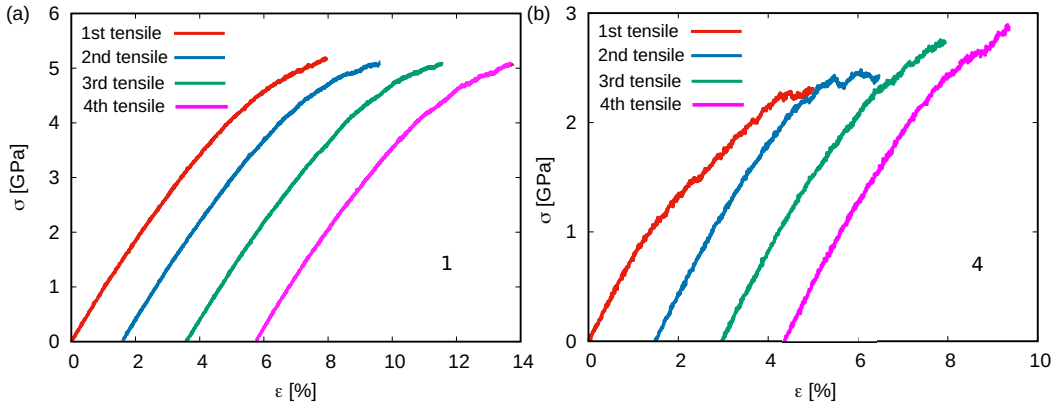


**Figure 7.19:** The stress–strain curves of the loading–unloading tensile test of (**a**) the as-cast MG (sample 1) and (**b**) the highly rejuvenated MG (sample 4).

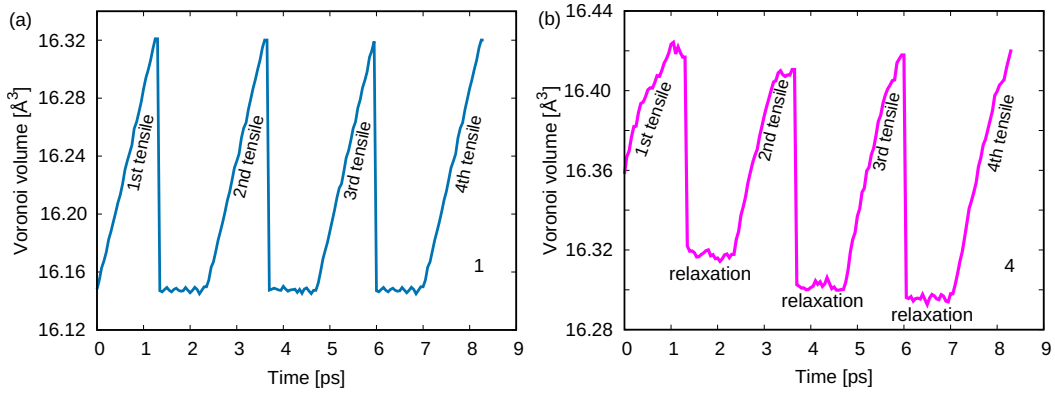


**Figure 7.20:** Voronoi volume evolution during cycling tensile test of (**a**) the as-cast MG (sample 1) and (**b**) the highly rejuvenated MG (sample 4).

As the cycling loading proceeds, the stress–strain curves show strain-hardening behavior up to the 40th reloading test (see Figure 7.21). This is supported by the continuous decrease of the free volume and the potential energy observed for sample 4 (see Figure 7.22a,b). The correlation between the variations in the atomic-level structure of the glassy system and the observed strain-hardening can be quantified using the fraction of the most favored Cu-centered short-range order (Cu-SRO) clusters (Figure 7.22c). As expected, the fast increases of the Cu-SRO fraction from 1st to 15th cycles demonstrate a continuous structural relaxation process that

reverts the system towards a more ordered state. Interestingly, the linear-like variation of Cu-SRO fraction from the 15th to 40th cycles indicates that there is no further structural relaxation. This suggests that the stress-driven structural relaxation is not the only reason for the observed strain-hardening in the rejuvenated MGs during the cycling tensile. Since residual stresses also can be responsible for the efficient strain-hardening in MGs [47], the internal stress state of the rejuvenated MG during each unloading stage was monitored and represented by the von Mises stress (VMS). As shown in Figure 7.22d, the decrease of VMS during the whole cycling process indicates that the residual stress, which was generated during the initial dilution process, is slowly released.

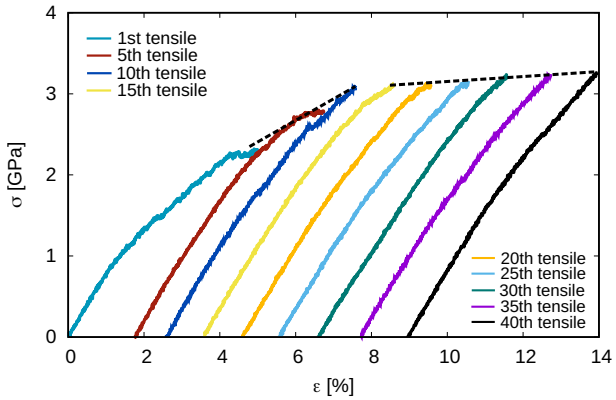


**Figure 7.21:** The evolution of stress–strain curves of the highly rejuvenated MG from the 1st to 40th reloading tensile tests. The dashed lines display the two regimes of the strain-hardening behavior.

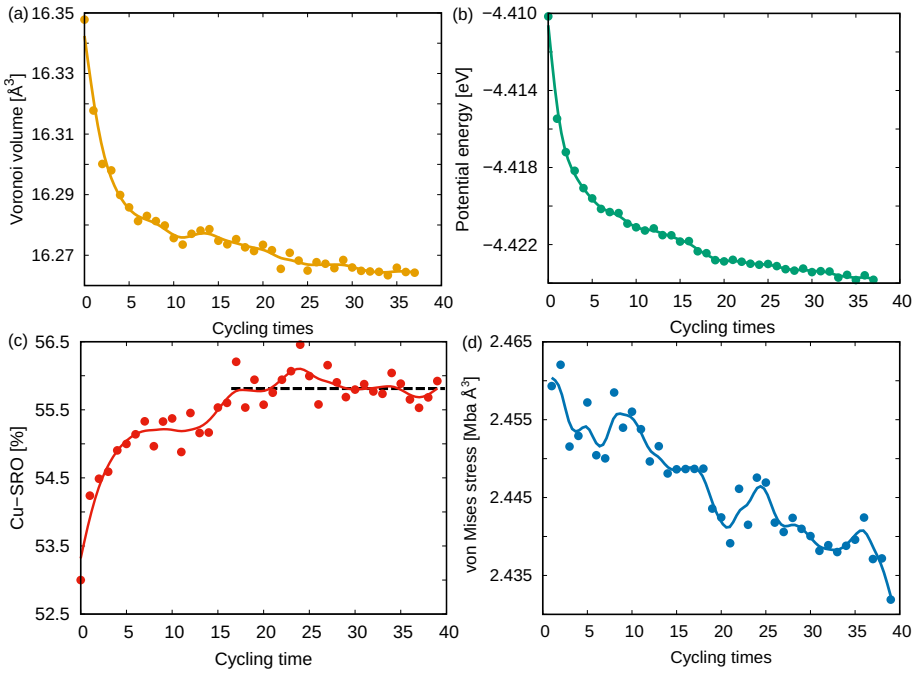


**Figure 7.22:** Evolution of (**a**) the Voronoi volume, (**b**) the potential energy, (**c**) the fraction of Cu–SRO, and (**d**) the von Mises stress of the highly rejuvenated MG during the 40 times cycling tensile tests. All of the parameters were calculated at each unloading stage.

The highly rejuvenated MG, sample 4, is in a high-energy state that possesses a high fraction of disordered structures and, at the same time, contains residual stresses. At the early stage of cycling loading (before the 15th cycle), stress-induced structural relaxation pushes the system towards a more ordered state and leads to significant strain-hardening behavior (Figure 7.21). After, the structural relaxation becomes sluggish (Figure 7.22c) but residual stresses still exist in the glass. Therefore, as the cycling loading continues (after 15th cycle), the residual stresses are still released (Figure 7.22d) during each loading stage that slightly lowers the excess free volume and the potential energy of the system (Figure 7.22a,b) and, consequently, increases the yield stress at the next cycle. Although the stress relaxation during the unloading–reloading process continues even after the 40th cycle, it is worth noticing that the hardening effect would level off and the rejuvenated MG could not achieve the strength of the as-cast state. Hence, one may reasonably predict that cycling loading can never relax a highly rejuvenated MG back to its initial as-cast state (at least after a reasonable number of cycles). To overcome shear-softening and achieve "real" strain-hardening and extensive ductility, one may shift focus to stress modulated MGs with residual stresses [47].

## 4. Conclusions

To summarize, in the present work, by randomly removing atoms from monolithic MGs, glass structures with different degrees of rejuvenation were designed and mechanically tested. Contrary to the observed rejuvenation behavior in the as-cast glassy system, the extreme rejuvenated MG exhibited structural and stress relaxation during uniaxial deformation. Under cycling tensile loading, the highly rejuvenated MG showed strain-hardening mainly for two reasons: (1) The effect of stress-induced structural relaxation that progressively decreases the potential energy and free volume. (2) As the structural relaxation becomes sluggish, the unloading–reloading process continues to release internal residual stresses from the glass that, over progressive cycling loading, induce further strain-hardening. The incremental relaxation process during the cycling loading–unloading tests leads the rejuvenated MG towards a more stable state. Nevertheless, no evidence shows that it can recover the hardness of the initial as-cast state even after 40 cycling tensile tests.

## Authorcontributions

X.Y. contributed to visualization, formal analysis and data analysis, writing the original draft.

D.Ş. contributed to conceptualization, formal analysis, data analysis, supervision, writing the original draft and further reviewing and editing. K.K.S. contributed to further reviewing and editing. J.E. contributed to conceptualization, supervision and further reviewing and editing. All authors have read and agreed to the published version of the manuscript.

## Funding

This research was funded by the Deutsche Forschungsgemeinschaft (DFG) (Grant No. SO 1518/1-1), the European Research Council under the ERC Advanced Grant INTELHYB (grant ERC-2013-ADG-340025) and the National Natural Science Foundation of China (51871132).

## Acknowledges

The authors acknowledge financial support by the China Scholarship Council (CSC, 201806220096). The authors are grateful for the computing time granted by the Lichtenberg high performance computer of the Technische Universität Darmstadt.

## References

[1] Wang, W.H.; Dong, C.; Shek, C. Bulk metallic glasses. *Mater. Sci. Eng. R Rep.* **2004**, *44*, 45–89.

[2] Greer, A.L. Metallic glasses. In *Physical Metallurgy* ; Elsevier, Amsterdam, Netherlands, 2014; pp. 305–385.

[3] Löffler, J.F. Bulk metallic glasses. *Intermetallics* **2003**, *11*, 529–540.

[4] Yu, H.B.; Richert, R.; Samwer, K. Structural rearrangements governing Johari-Goldstein relaxations in metallic glasses. *Sci. Adv.* **2017**, *3*, e1701577.

[5] Gallino, I.; Busch, R. Relaxation pathways in metallic glasses. *JOM* **2017**, *69*, 2171–2177.

[6] Saida, J.; Yamada, R.; Wakeda, M. Recovery of less relaxed state in Zr-Al-Ni-Cu bulk metallic glass annealed above glass transition temperature. *Appl. Phys. Lett.* **2013**, *103*, 221910.

[7] Sun, Y.; Concustell, A.; Greer, A.L. Thermomechanical processing of metallic glasses: Extending the range of the glassy state. *Nat. Rev. Mater.* **2016**, *1*, 1–14.

[8] Küchemann, S.; Derlet, P.M.; Liu, C.; Rosenthal, D.; Sparks, G.; Larson, W.S.; Maaß, R. Energy storage in metallic glasses via flash annealing. *Adv. Funct. Mater.* **2018**, *28*, 1805385.

[9] Controlled rejuvenation of amorphous metals with thermal processing.

[10] Ketov, S.; Sun, Y.; Nachum, S.; Lu, Z.; Checchi, A.; Beraldin, A.; Bai, H.; Wang, W.;

Louzguine-Luzgin, D.; Carpenter, M.; et al. Rejuvenation of metallic glasses by non-affine thermal strain. *Nature* **2015**, *524*, 200–203.

[11] Pan, J.; Wang, Y.; Guo, Q.; Zhang, D.; Greer, A.; Li, Y. Extreme rejuvenation and softening in a bulk metallic glass. *Nat. Commun.* **2018**, *9*, 1–9.

[12] Park, K.W.; Lee, C.M.; Wakeda, M.; Shibutani, Y.; Falk, M.L.; Lee, J.C. Elastostatically induced structural disordering in amorphous alloys. *Acta Mater.* **2008**, *56*, 5440–5450.

[13] Concustell, A.; Méar, F.; Surinach, S.; Baró, M.; Greer, A. Structural relaxation and rejuvenation in a metallic glass induced by shot-peening. *Philos. Mag. Lett.* **2009**, *89*, 831–840.

[14] Dmowski, W.; Yokoyama, Y.; Chuang, A.; Ren, Y.; Umemoto, M.; Tsuchiya, K.; Inoue, A.; Egami, T. Structural rejuvenation in a bulk metallic glass induced by severe plastic deformation. *Acta Mater.* **2010**, *58*, 429–438.

[15] Ding, G.; Li, C.; Zaccone, A.; Wang, W.; Lei, H.; Jiang, F.; Ling, Z.; Jiang, M. Ultrafast extreme rejuvenation of metallic glasses by shock compression. *Sci. Adv.* **2019**, *5*, eaaw6249.

[16] Xiao, Q.; Huang, L.; Shi, Y. Suppression of shear banding in amorphous ZrCuAl nanopillars by irradiation. *J. Appl. Phys.* **2013**, *113*, 083514.

[17] Fan, Y.; Iwashita, T.; Egami, T. How thermally activated deformation starts in metallic glass. *Nat. Commun.* **2014**, *5*, 1–7.

[18] Saida, J.; Yamada, R.; Wakeda, M.; Ogata, S. Thermal rejuvenation in metallic glasses. *Sci. Technol. Adv. MaTerialS* **2017**, *18*, 152–162.

[19] Feng, S.; Chan, K.; Zhao, L.; Pan, S.; Qi, L.; Wang, L.; Liu, R. Rejuvenation by weakening the medium range order in Zr46Cu46Al8 metallic glass with pressure preloading: A molecular dynamics simulation study. *Mater. Des.* **2018**, *158*, 248–255.

[20] Ding, J.; Cheng, Y.Q.; Sheng, H.; Asta, M.; Ritchie, R.O.; Ma, E. Universal structural parameter to quantitatively predict metallic glass properties. *Nat. Commun.* **2016**, *7*, 1–10.

[21] Pan, J.; Ivanov, Y.P.; Zhou, W.; Li, Y.; Greer, A. Strain-hardening and suppression of shear-banding in rejuvenated bulk metallic glass. *Nature* **2020**, *578*, 559–562.

[22] Tang, B.; Erb, U.; Brooks, I. Strain hardening in polycrystalline and nanocrystalline nickel. In *Advanced Materials Research*; Trans Tech Publications Ltd., Stafa-Zurich, Switzerland, 2012; Volume 409, pp. 550–554.

[23] Yoo, B.G.; Park, K.W.; Lee, J.C.; Ramamurty, U.; Jang, J.i. Role of free volume in strain softening of as-cast and annealed bulk metallic glass. *J. Mater. Res.* **2009**, *24*, 1405–1416.

[24] Jang, D.; Greer, J.R. Transition from a strong-yet-brittle to a stronger-and-ductile state by size reduction of metallic glasses. *Nat. Mater.* **2010**, *9*, 215–219.

[25] Tian, L.; Cheng, Y.Q.; Shan, Z.W.; Li, J.; Wang, C.C.; Han, X.D.; Sun, J.; Ma, E. Approaching the ideal elastic limit of metallic glasses. *Nat. Commun.* **2012**, *3*, 1–6.

[26] Wang, Z.; Pan, J.; Li, Y.; Schuh, C.A. Densification and strain hardening of a metallic glass under tension at room temperature. *Phys. Rev. Lett.* **2013**, *111*, 135504.

[27] Shang, B.; Wang, W.; Greer, A.L.; Guan, P. Atomistic modelling of thermal-cycling rejuvenation in metallic glasses. *Acta Mater.* **2021**, *213*, 116952.

[28] Yuan, X.; Şopu, D.; Spieckermann, F.; Song, K.; Ketov, S.; Prashanth, K.; Eckert, J. Maximizing the degree of rejuvenation in metallic glasses. *Scr. Mater.* **2022**, *212*, 114575.

[29] Plimpton, S. Fast parallel algorithms for short-range molecular dynamics. *J. Comput. Phys.* **1995**, *117*, 1–19.

[30] Mendelev, M.; Sordelet, D.; Kramer, M. Using atomistic computer simulations to analyze X-ray diffraction data from metallic glasses. *J. Appl. Phys.* **2007**, *102*, 043501.

[31] Stukowski, A. Visualization and analysis of atomistic simulation data with OVITO–the Open Visualization Tool. *Model. Simul. Mater. Sci. Eng.* **2009**, *18*, 015012, doi:10.1088/0965-0393/18/1/015012.

[32] Brostow, W.; Chybicki, M.; Laskowski, R.; Rybicki, J. Voronoi polyhedra and Delaunay simplexes in the structural analysis of molecular-dynamics-simulated materials. *Phys. Rev. B* **1998**, *57*, 13448.

[33] Li, Q.K.; Li, M. Free volume evolution in metallic glasses subjected to mechanical deformation. *Mater. Trans.* **2007**, *48*, 1816–1821.

[34] Mahmoud, Z.H.; Barazandeh, H.; Mostafavi, S.M.; Ershov, K.; Goncharov, A.; Kuznetsov, A.S.; Kravchenko, O.D.; Zhu, Y. identification of rejuvenation and relaxation regions in a Zr-based metallic glass induced by laser shock peening. *J. Mater. Res. Technol.* **2021**, *11*, 2015–2020.

[35] Greer, A.; Sun, Y. Stored energy in metallic glasses due to strains within the elastic limit. *Philos. Mag.* **2016**, *96*, 1643–1663.

[36] Şopu, D.; Scudino, S.; Bian, X.; Gammer, C.; Eckert, J. Atomic-scale origin of shear band multiplication in heterogeneous metallic glasses. *Scr. Mater.* **2020**, *178*, 57–61.

[37] Sopu, D.; Foroughi, A.; Stoica, M.; Eckert, J. Brittle-to-ductile transition in metallic glass nanowires. *Nano Lett.* **2016**, *16*, 4467–4471.

[38] Şopu, D.; Yuan, X.; Moitzi, F.; Spieckermann, F.; Bian, X.; Eckert, J. From elastic excitations to macroscopic plasticity in metallic glasses. *Appl. Mater. Today* **2021**, *22*, 100958.

[39] Rodney, D.; Schuh, C. Distribution of thermally activated plastic events in a flowing glass. *Phys. Rev. Lett.* **2009**, *102*, 235503.

[40] Zink, M.; Samwer, K.; Johnson, W.; Mayr, S. Validity of temperature and time equiva-

lence in metallic glasses during shear deformation. *Phys. Rev. B* **2006**, *74*, 012201.

[41] Swayamjyoti, S.; Löffler, J.F.; Derlet, P. Local structural excitations in model glasses. *Phys. Rev. B* **2014**, *89*, 224201.

[42] Teichler, H. Structural dynamics on the $\mu$s scale in molecular-dynamics simulated, deeply undercooled, glass-forming $Ni_{0.5}Zr_{0.5}$. *J. Non-Cryst. Solids* **2001**, *293*, 339–344.

[43] Meng, F.; Tsuchiya, K.; Seiichiro, I.; Yokoyama, Y. Reversible transition of deformation mode by structural rejuvenation and relaxation in bulk metallic glass. *Appl. Phys. Lett.* **2012**, *101*, 121914.

[44] Qiang, J.; Tsuchiya, K. Composition dependence of mechanically-induced structural rejuvenation in Zr-Cu-Al-Ni metallic glasses. *J. Alloy. Compd.* **2017**, *712*, 250–255.

[45] Louzguine-Luzgin, D.; Ketov, S.; Wang, Z.; Miyama, M.; Tsarkov, A.; Churyumov, A.Y. Plastic deformation studies of Zr-based bulk metallic glassy samples with a low aspect ratio. *Mater. Sci. Eng. A* **2014**, *616*, 288–296.

[46] Haruyama, O.; Kisara, K.; Yamashita, A.; Kogure, K.; Yokoyama, Y.; Sugiyama, K. Characterization of free volume in cold-rolled $Zr_{55}Cu_{30}Ni_5Al_{10}$ bulk metallic glasses. *Acta Mater.* **2013**, *61*, 3224–3232.

[47] Yuan, X.; Şopu, D.; Eckert, J. Origin of strain hardening in monolithic metallic glasses. *Phys. Rev. B* **2021**, *103*, L140107.

# Publication IV

PHYSICAL REVIEW B **103**, L140107 (2021)

Letter

## Origin of strain hardening in monolithic metallic glasses

X. Yuan,[1] D. Şopu,[1,2,*] and J. Eckert[1,3]

[1]*Erich Schmid Institute of Materials Science, Austrian Academy of Sciences, Jahnstraße 12, A-8700 Leoben, Austria*

[2]*Technische Universität Darmstadt, Institut für Materialwissenschaft, Fachgebiet Materialmodellierung, Otto-Berndt-Straße 3, D-64287 Darmstadt, Germany*

[3]*Department of Materials Science, Chair of Materials Physics, Mountanuniversität Leoben, Jahnstraße 12, A-8700 Leoben, Austria*

(Received 9 January 2021; accepted 13 April 2021; published 29 April 2021)

To overcome the brittleness of metallic glasses (MGs), their structure, chemistry, or loading conditions are usually controlled. Here, the local stress state in MGs was modulated without affecting their structure. The elastically designed MG heterostructures provide enhanced ductility together with strain hardening during loading. The stress heterogeneity leads to shear band multiplication that consequently enhances the macroscopic ductility of MGs. In addition, the residual compressive stress significantly increases the strength of the glass and is responsible for the observed strain hardening.

DOI: 10.1103/PhysRevB.103.L140107

Enhancing the plasticity [1–4] and overcoming the strain-softening of MGs remains a long-standing issue in materials physics. A common strategy to prevent brittle catastrophic failure at room temperature is the synthesis of MG composites with soft crystalline phases [5, 6]. In general, a secondary phase improves the ductility of MG composites but compromises their strength [1]. To overcome the inverse strength-ductility relationship MG composites containing shape memory crystals were successfully developed. Here, hardening through deformation-induced martensitic transformation of the incorporated crystals overwhelms the shear banding-induced softening of the glassy matrix [7]. Additionally, the suppression of shearing through size or geometric constraints, as demonstrated for nanosized samples [8, 9] or notched rods [10], may also lead to the apparent strain-hardening.

Recently, it has been shown that strain-hardening and enhanced ductility can be also achieved in monolithic MGs even without limitations in size or mechanical constraints when they are highly rejuvenated [11]. Generally, extrem rejuvenation of MG structures by pre-deformation techniques lowers their yield stress, and can in special cases enable strain-hardening. This exceptional strain-hardening was associated with structural relaxation, which can be regarded as return from the rejuvenated state. Nevertheless, if so, then a similar phenomenon must be observed in MG structures subjected to rejuvenation by thermal cycling, elastostatic loading or other rejuvenation techniques that leads to an even stronger rejuvenation effect comparable with that seen after heavy plastic deformation [12]. Furthermore, structural rejuvenation involves plastic strain and shear band formation that is usually confined to a thickness of $10-20\ nm$ [13]. Consequently, even the proliferation of a large number of shear bands would result in a low volume fraction of rejuvenated material with respect to the total volume of the sample. Hence, considering the possibility of returning from a highly rejuvenated state to an even more aged state could not fully explain the observed strain-hardening. However, while the formation of a high density of shear bands can safely explain the observed extensive homogeneous flow, we assume that the strain-hardening arises not from intrinsic changes to the glassy structure, but rather from residual stresses imparted during the pre-deformation protocol. During triaxial tests the formation of a large number of intersecting shear bands is actually the driving force for the local stress modulation between these shear bands that could span over several microns [14]. This, in turn, results in the generation of a stress gradient within the sample [14] and the change in the sign of stress from compressive to tensile across shear bands [15]. Consequently, all these could alter the further shear-banding process and enable strain-hardening in uniaxial tensile tests.

Here we rely on computational modeling to provide an atomistic model to clarify what causes enhanced tensile ductility and strain-hardening in monolithic MGs. By modulating the internal stress state and the local structure of the glass, we differentiate between the role of stress heterogeneities, residual stresses and structural heterogeneities in improving the mechanical properties of MGs. Additionally, we focus our attention on clarifying the origins of strain-hardening in monolithic MGs as one of the most debated aspects of the last decades.

To provide an atomistic picture of the deformation mechanisms of stress/structurally modulated MG heterostructures large-scale molecular dynamics (MD) simulations were carried out using the LAMMPS software [16]. The $Cu_{64}Zr_{36}$ MG was used as a prototype material and the interatomic interactions were described by the Finnis-Sinclair type potential developed by Mendelev et al. [17]. The starting liquid structure was obtained by randomly distributing 0.9 million atoms in a box of $5.6\times23\times113\ nm^{\ 2}$ with periodic boundary conditions (PBCs) in all directions. Uniform-acceptance force bias Monte Carlo [18] and MD in an NPT ensemble were used alternately, in order to deal with the overlapping atoms during the initial equilibration of the liquid structure. The liquid structure was cooled down 50 $K$ above $T_g$ at a rate of $10^{11}\ K/s$ starting from 2000 $K$. The cooling rate was reduced to $10^{10}\ K/s$ in a temperature range of 100 $K$ around $T_g$ where the local structure of MGs mostly develop [19, 20]. After cooling down to 50 $K$ below Tg annealing for 4.0 $ns$ was performed. The final cooling to 50 $K$ was then done with $10^{11}\ K/s$ at zero pressure to obtain an initial as-cast glass (AC).

The design of stress-modulated MG heterostructures is schematically presented in Fig. 7.23. Glassy blocks of different stress state (compressive and tensile) were created in three steps: (i) the initial AC block was affine transformed by increasing or decreasing the size along the $z$-direction by different percentages. (ii) These blocks were remelted to 2000 $K$ to release the residual stresses and then quenched down to 50 $K$ following similar procedure as described for the AC glass. (iii) Stress modulated MG heterostructures were constructed by joining these blocks mutually after they have been re-scaled along the $z$-direction to the original size of the AC block. Further details about the sample preparation are presented in the Supplementary Materials [21], Sec. S1. In the following discussion, the T and C terminology means that the glassy blocks are under tensile or compressive stress states.

Tensile tests were performed under a constant engineering strain rate of $4\times10^{7}\ /s$ in a NPT ensemble at 50 $K$ with PBCs in all directions. Before tensile loading, all of the systems are relaxated for 100 $ps$ under the constraint along $z$-direction while allowing the other two directions to relax in order to retain the residual stress that are generated by pre-deformation.

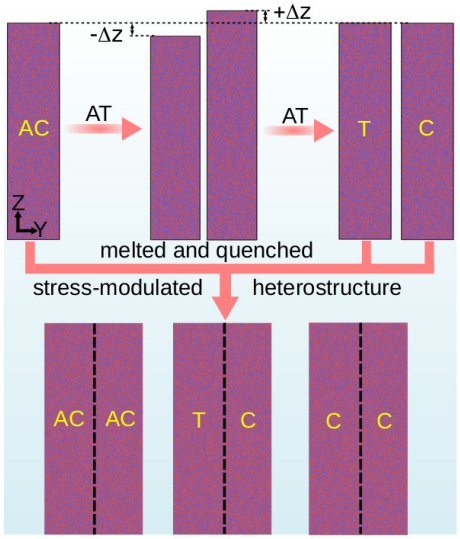


**Figure 7.23:** Schematic representation of construction of stress-modulated $Cu_{64}Zr_{36}$ samples. An affine transformation (AT) along the z-direction was executed on the AC via changing the size by $\pm$ $\Delta$z ( $\pm$ 1%, $\pm$ 2%, etc.). The re-scaled blocks were remelted at 2000 $K$ and quenched down to 50 $K$ following the same cooling procedure as done for the AC sample. Elastic pre-deformation was conducted by applying an AT in $z$-direction to the re-cooled samples to re-scale their size to the one of the AC block to obtain pre-tensile (T) and pre-compressive (C) stressed parts. Stress modulated MG heterostructures were prepared by assembling AC, C, and T mutually, leaving a 0.2 $nm$ interface between the blocks.

The deformation behavior was analyzed by the calculation and visualization of the sign of rotation angle, as implemented in the software OVITO [25] using a python scripting interface. The atomic-level local structure was analyzed in terms of local entropy which shows a high predictive power and allows for the gradual representation of the atomic-level local structure without any prior information on a reference configuration [26] (Further details about the rotation angle and local entropy calculation are presented in the Supplementary Materials [21], Sec. S3 and S4). These two parameters were evaluated at each atomic site from the relative displacements of neighboring atoms within a cut-off range of 6 Å. The stress state of the samples was monitored by the stress tensor along tensile direction $pzz$. All parameters were evaluated along the $y$-axis at $\varepsilon$ = 0% and average values were calculated within a narrow slab with a width of 1 $nm$ that scans along the selected area in steps of 0.2 $nm$.

Monolithic MGs generally show nearly zero ductility at room temperature due to the highly localized nature of the deformation process [27, 28]. The deformation of two AC glassy blocks separated by one interface the deformation is highly localized in one single shear band (Fig. 7.24(a)). The propagation of the shear band causes the stress drop in the stress-strain curve. Usually, a very effective strategy to attenuate the brittleness of MGs is the introduction of structural heterogeneities in terms of harder (denser) and softer glassy (rejuvenated) regions (Hard-Soft heterostructure) [29, 30]. The shear bands are branched and deflected in the areas

ahead of the soft/hard interface, favoring shear band multiplication [29, 31]. More informations about deformation mechanims in structural modulated MG heterostructures can be found in the Supplementary Materials [21], Sec. S2. The soft structural heterogeneities are beneficial for improving the plasticity of MGs but sacrifice their strength. Despite tremendous efforts and progress the achievement of both, strain-hardening and enhanced ductility, remains a major challenge.

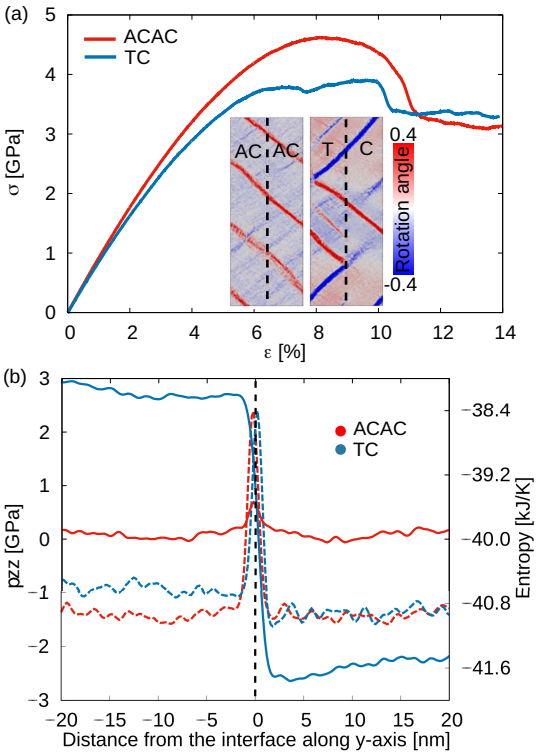


**Figure 7.24:** (a): Tensile stress-strain curves of TC and ACAC samples. The embedded panels illustrate the sign of the rotation angle (radians) of the ACAC sample and TC sample at $\varepsilon$ = 14%. (b): The distribution of stress (solid lines) and local entropy (dashed lines) along the $y$-axis in the TC and ACAC samples at $\varepsilon$ = 0%.

Since the propagation of a shear band is a stress-driven process [32, 33] one may wonder whether the deformation behavior of MGs can be controlled by modulating their internal stress states. As shown in Fig. 7.24, we designed a two-zone heterostructure of same structure but different stress state by combining T and C glassy blocks with residual stresses along $z$-direction of about $\pm$ 3 $GPa$. The distribution of stress shows an obvious variation across the interface while the local entropy indicates a homogeneous distribution in the entire sample (Fig. 7.24(b)). As the external load is zero, $\varepsilon$=0%, the significant stress difference found across the interface in TC sample corresponds to tensile and compressive residual stresses induced by the elastic pre-deformation process (see Fig. 7.24(b)). However, the average residual stress in the TC heterostructure is close to zero (shown as the equivalent absolute value of $pzz$ in the T and C

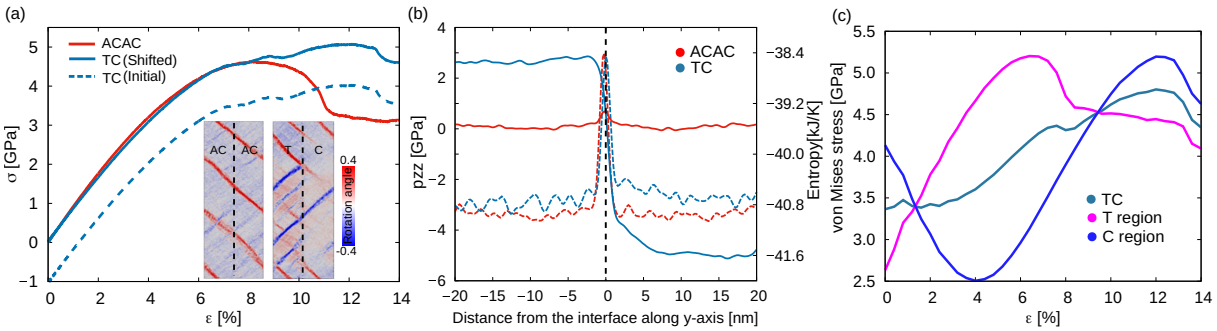


**Figure 7.25:** (a) Tensile stress-strain curves of the TC and ACAC samples. The dashed line represents the initial curve of the TC sample and the negative stress value at zero strain indicates a compressive residual stress. For a better comparison with the ACAC sample, the starting point of the dashed line is shifted to zero stress. The embedded panels illustrate the sign of the rotation angle (radians) of the TC and ACAC samples at $\varepsilon$ = 14%. (b) Distribution of stress (solid line) and local entropy (dashed line) along the $y$-axis in the TC and ACAC samples at $\varepsilon$ = 0%. (c) The von Mises stress of T region, C region and the entire TC sample during deformation are calculated individually for comparison. The decrease of von Mises stress in the C region before 4% strain corresponds to the dismissal process of the residual compressive stress.

parts in Fig. 7.24(b)). Due to the stress-modulation the sample can be seen as a dual-phase heterostructure that will yield at different strain/stress levels. At the early plastic stage, shear is firstly activated in the T region and the shear band front attempts to extend across the interface to transect over the entire sample. However, the residual compressive stress in the C region obstructs these shear bands. The STZs have to overcome a higher average activation energy barrier in the C region and, hence, STZ activation and percolation are deferred. With further loading, more and more shear bands nucleate in the T region and the deformation develops through a highly organized pattern of multiple shear bands distributed uniformly throughout the structure (Fig. 2(a)). The interaction of the multiple shear bands delays fracture and gives rise to a ductile deformation process. Although the stress heterogeneity enhances the tensile ductility, the yield stress of the TC heterostructure decreases from 4.5 $GPa$ to 3.8 $GPa$ (Fig. 7.24(a)) as a consequence of shear softening: every shear event corresponds to a stress drop.

Previous research suggests that the compressive residual stress can be considered as an apparent contribution to the increased strength in gradient-structured materials [34] and even in chemically strengthened oxide glasses, so-called Gorilla Glass [35]. More interestingly, it was suggested that even MGs can exhibit remarkable work-hardening like behavior and significant increase of plastic strain that was correlated to the residual compressive stress imparted during surface mechanical attrition treatment [36]. Additionally, MD simulations of cyclic indentation loading in CuZr metallic glass revealed also hardening behavior induced by confined microplasticity and local accumulation of irreversible compressive shear strain [37, 38]. In the

following, therefore, we designed a stress-modulated MG heterostructure with an overall compressive stress by assembling the T and C blocks with a nominal stress along $z$-direction of $\approx$2.5 GPa and -5 GPa. The distribution of the local entropy and stress in the TC heterostructure (Fig. 7.25(b)) illustrates that the elastic pre-deformation will not cause significant changes to the atomic structure but will drastically increase the residual stress in the glass. Fig. 7.25(a) compare the stress-strain curves of the ACAC sample and the TC heterostructure. As expected, the compressive residual stress mirrors to a negative stress value at $\varepsilon$ = 0% (dashed line) and, basically, the stress-strain curve do not start from zero as found for the ACAC sample and other heterostructures with zero residual stress. Moreover, contrary to the suddenly stress-drop seen in the ACAC sample, the yield stress in the stress modulated heterostructure increases with applied strain indicating "real" strain-hardening with an ultimate strength of 5.1 $GPa$ (after re-scaling the stress-strain curve to zero). During tensile deformation, the part of the heterostructure with a tensile residual stress yields first and many shear bands confined to the T region nucleate. Since none of these shear bands becomes critical the applied stress cannot be compensated by the shear stress released which explains strain-hardening that can reach $\varepsilon$=13% (see Fig. 7.25(a)). With the shear band inhibited by the compressive residual stress, the heterostructure shows high ductility and toughness.

Under tensile loading, the residual compressive stress can be seen as a back stress [39] that must be overcome by the system to switch to a tensile stress state. To clarify this aspect we evaluate separately the von Mises stress evolution in T and C blocks in comparison to the von Mises stress within the whole sample. The von Mises stress corresponds to the deformation energy due to pure distortion [29] and it reflects the overall stress state of the system. As shown in Fig. 7.25(c), the von Mises stress in the T block starts to increase monotonically until the yielding point when partially the stress is released during shearing process. On the other hand, initially the von Mises stress in the C block decreases until a strain level of 4% followed by an increases up to a strain level of 13% when some shear bands from the T block start propagating through the C block. Basically, the mechanical response of the TC heterostructure can be predicted based on the rule of mixtures of the two glassy blocks.

With further loading, after $\varepsilon$=13%, a first small stress drop in the stress-strain curve of TC heterostructure can be observed. This correlates with the yielding of the C region (Fig. 7.25(a)). Nevertheless, compared to the TC heterostructure with zero residual compressive stress, no dominant shear band forms resulting in a rather uniform deformation through the formation and intersection of multiple shear bands. Based on the above comparison, we conclude that

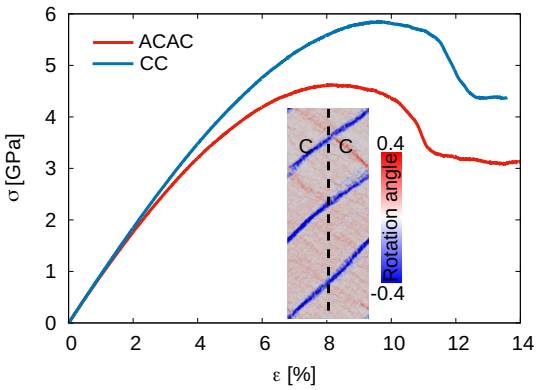


**Figure 7.26:** Tensile stress-strain curves of the CC and ACAC samples. The rotation angle (radians) at $\varepsilon = 14\%$ is shown in the embedded panel.

while structural or stress heterogeneities contribute to ductile improvement the compressive residual stress is the crucial factor for strain-hardening. The best combination of high ductility and strain-hardening may be obtained in heterostructures with large fluctuations in the local stress and residual stress magnitudes overcoming the shear-induced softening. As shown in Fig. 7.26, a heterostructure that only has compressive residual stress and no stress-modulation (by combine two C glassy blocks) shows brittle deformation by the formation of a single dominant shear band.

As shown previously [10, 12], deformation under triaxial compression is an inhomogeneous method to rejuvenate MG structures by the formation of a highly dense network of shear bands. Although the structure between the shear bands, which occupies the largest volume, does not undergo important modifications, its stress state is strongly modulated by the shear process. Even without the triaxial constraint, after cutting out the highly rejuvenated region within the notched rod, the residual stress remains confined in the structure. The formation of such a complex network of intersecting shear bands will suppress elastic relaxation. This actually explains the observed strain-hardening without mechanical constraints in ref. [11]. However, such kind of rejuvenation procedure cannot systematically control and manipulate the structural and elastic heterogeneity in MGs and, therefore, better methods able to systematically tailor the residual stress must be developed if one wants to apply the full potential of metallic glasses as structural materials.

In summary, the correlation between the deformation behavior and the residual stress modulation in MGs was investigated. Strain-hardening together with enhanced tensile ductility in monolithic MGs can be attained by only modulating the internal residual stress without changing their local structure. Overall, compressive residual stresses together with a heterogeneous

stress distribution enable strain-hardening together with extensive homogeneous flow. The stress heterogeneity caused by the residual stresses imparted during suitable pre-deformation protocols can change the shear band dynamics leading to the formation and interaction of multiple shear bands, which consequently enhances the deformability. Moreover, the residual compressive stress offsets the external tensile stress, which delays shear band formation and, therefore, is responsible for effcient strain-hardening and toughness. The fact that MGs can overcome shear-softening mechanical behavior and achieve strain-hardening and extensive ductility at room temperature without affecting structural order underpins the potential of using MGs as structural materials.

The authors acknowledge financial support by the China Scholarship Council (CSC, 201806220096), the Deutsche Forschungsgemeinschaft (DFG) (Grant no. SO 1518/1-1) and the European Research Council under the ERC Advanced Grant INTELHYB (Grant no. ERC-2013-ADG-340025). The authors are grateful for the computing time granted by the Lichtenberg high performance computer of the Technische Universität Darmstadt and the high performance cluster of the Montanuniversität Leoben.

## References


[1] D. C. Hofmann, J.-Y. Suh, A. Wiest, G. Duan, M.-L. Lind, M. D. Demetriou, and W. L. Johnson, Nature **451**, 1085 (2008).

[2] S. Pauly, S. Gorantla, G. Wang, U. Kühn, and J. Eckert, Nat. Mater. **9**, 473 (2010).

[3] D. C. Hofmann, Science **329**, 1294 (2010).

[4] K. Albe, Y. Ritter, and D. Şopu, Mech. Mater. **67**, 94 (2013).

[5] G. He, J. Eckert, W. Löser, and L. Schultz, Nat. Mater. **2**, 33 (2003).

[6] M. Calin, J. Eckert, and L. Schultz, Scr. Mater. **48**, 653 (2003).

[7] Y. Wu, Y. Xiao, G. Chen, C. T. Liu, and Z. Lu, Adv. Mater. **22**, 2770 (2010).

[8] D. Jang and J. R. Greer, Nat. Mater. **9**, 215 (2010).

[9] L. Tian, Y.-Q. Cheng, Z.-W. Shan, J. Li, C.-C. Wang, X.-D. Han, J. Sun, and E. Ma, Nat. Commun. **3**, 1 (2012).

[10] Z. T. Wang, J. Pan, Y. Li, and C. A. Schuh, Phys. Rev. Lett. **111**, 135504 (2013).

[11] J. Pan, Y. P. Ivanov, W. Zhou, Y. Li, and A. Greer, Nature **578**, 559 (2020).

[12] A. Greer and Y. Sun, Philos. Mag. **96**, 1643 (2016).

[13] Y. Zhang and A. Greer, Appl. Phys. Lett. **89**, 071907 (2006).

[14] R. Maaß, K. Samwer, W. Arnold, and C. Volkert, Appl. Phys. Lett. **105**, 171902 (2014).

[15] S. Scudino, J. Alloys Compd. **773**, 883 (2019).

[16] S. Plimpton, J. Comput. Phys. **117**, 1 (1995).

[17] M. Mendelev, D. Sordelet, and M. Kramer, J. Appl. Phys. **102**, 043501 (2007).

[18] M. J. Mees, G. Pourtois, E. C. Neyts, B. J. Thijsse, and A. Stesmans, Phys. Rev. B. **85**, 134301 (2012).

[19] A. Foroughi, H. Ashuri, R. Tavakoli, M. Stoica, D. Şopu, and J. Eckert, J. Appl. Phys. **122**, 215106 (2017).

[20] F. Moitzi, D. Şopu, D. Holec, D. Perera, N. Mousseau, and J. Eckert, Acta. Mater. **188**, 273 (2020).

[21] See Supplemental Material at [URL] for additional information regarding heterostructures preparation, rotation angle and local entropy calculation, and structure analysis, which includes Refs. [22-25] .

[22] Y. Cheng, A. J. Cao, H. Sheng, and E. Ma, Acta. Mater. **56**, 5263 (2008).

[23] P. M. Piaggi and M. Parrinello, J. Chem. Phys. **147**, 114112 (2017).

[24] W. Brostow, M. Chybicki, R. Laskowski, and J. Rybicki, Phys. Rev. B. **57**, 13448 (1998).

[25] A. Stukowski, Model. Simul. Mater. Sci. Eng. **18**, 015012 (2009).

[26] D. Şopu, F. Moitzi, N. Mousseau, and J. Eckert, Appl. Mater. Today **21**, 100828 (2020).

[27] F. Shimizu, S. Ogata, and J. Li, Acta. Mater. **54**, 4293 (2006).

[28] D. Şopu, A. Stukowski, M. Stoica, and S. Scudino, Phys. Rev. Lett. **119**, 195503 (2017).

[29] D. Şopu, S. Scudino, X. Bian, C. Gammer, and J. Eckert, Scr. Mater. **178**, 57 (2020).

[30] C. Liu and R. Maaß, Adv. Funct. Mater. **28**, 1800388 (2018).

[31] S. Scudino, J. Bian, H. S. Shahabi, D. Şopu, J. Sort, J. Eckert, and G. Liu, Sci. Rep. **8**, 1 (2018).

[32] S. G. Mayr, Phys. Rev. Lett. **97**, 195501 (2006).

[33] F. Delogu, Phys. Rev. Lett. **100**, 255901 (2008).

[34] M.-X. Yang, R.-G. Li, P. Jiang, F.-P. Yuan, Y.-D. Wang, Y.-T. Zhu, and X.-L. Wu, Mater. Res. Lett. **7**, 433 (2019).

[35] N. Terakado, R. Sasaki, Y. Takahashi, T. Fujiwara, S. Orihara, and Y. Orihara, Commun. Phys. **3**, 1 (2020).

[36] J. J. Liu, Q. Wang, K. Sun, S. Gravier, J. J. Blandin, B. Sun, and J. Lu, J. Iron Steel Res. Int. **24**, 475 (2017).

[37] C. Deng and C. A. Schuh, Appl. Phys. Lett. **100**, 251909 (2012).

[38] D. Zhao, H. Zhao, B. Zhu, and S. Wang, Appl. Surf. Sci. **416**, 14 (2017).

[39] Y. Zhu and X. Wu, Mater. Res. Lett. **7**, 393 (2019).

# Supplementary Materials

### S1: Preparation of stress-modulated MG heterostructures

Glassy blocks of different stress state were created in three steps:

1. Initial size modification: The initial AC block was affine transformed by increasing or decreasing the size along the $z$-direction by different percentages. In the present work, we finally adopted 5 new blocks which was created by increasing the size by 2%, 3% and 4% and decreasing by 1% and 2%.

2. Remelting: The new blocks were remelted to 2000 $K$ (to release the artificial residual stress) and then quenched down to 50 $K$ following similar procedure as described for the AC glass (see the methods in the main manuscript). In order to control the sample sizes, the remelting and quenching procedure was conducted in a NPT ensemble while holding fix the $x$- and $z$-directions while the residual stress can be released along $y$-direction.

3. Pre-deformation: Elastic pre-deformation was conducted by applying an affine transformation in $z$-direction to the requenched blocks and re-scaling their size to the one of the AC block to obtain pre-tensile (T) and pre-compressive (C) stressed parts. For example, the block which was decreased by 1% in the first step will be increased by 1% along $z$-direction to recover the size of the initial AC sample (1% pre-tensile). Similar procedure was followed for all of the blocks controlling in the way the magnitude and the sign (tensile vs. compressive) of the residual stress (see Table 1 and the negative value means the compressive stress state).

**Table 1:** The stress state of all the blocks after pre-deformation

| Affine transformation along z-direction | Increase | | Decrease | | | Initial AC |
|---|---|---|---|---|---|---|
| | 1% | 2% | 2% | 3% | 4% | |
| Stress along z-direction(pzz) (GPa) | 2.5 | 3.0 | -1.2 | -3.0 | -5.0 | 0 |

Stress modulated MG heterostructures were constructed by combining the pre-deformed blocks mutually and leave an 0.2 $nm$ interface in between. In order to introduce the interface in the ACAC sample and deal with periodic boundaries, a layer of atoms (around 0.3 $nm$) was cut from one edge of the $y$-axis in the initial AC sample that leaves unaffected the composition of the sample ($Cu_{64}Zr_{36}$). After, we joined together the sliced AC block with the other (untainted) AC block and create the ACAC sample. The same procedure is followed for the CC sample to generate the interface. For the TC samples, the affine-deformation protocol perturbs the periodic boundary conditions on $y$-axis and, hence, there is not need to generate an interface by

removing a thin slab of atoms. Prior to deformation, all of the heterostructures were relaxed at 50 $K$ for 100 $ps$ in an NPT ensemble and holding fix the $z$- direction and allowing the other two directions to relax in order to hold the residual stress generated by the pre-deformation process.

**S2: Hard-Soft heterostructure preparation and deformation mechanisms**

Fig. 7.27 shows the preparation procedure of the Hard-Soft heterostructure. The initial AC block was regarded as the Hard part. The Hard block is remelted to 2000 $K$ and quenched down to 50 $K$ with a much faster cooling rate $10^{12}$ $K/s$ while holding fixed the $x$- and $z$-directions. The new glassy samples prepared at a much higher cooling rate show a higher defective order and lower density (main text, Ref. [22]). Finally, we assemble the Hard and Soft blocks and leave an 0.2 $nm$ interface in between.

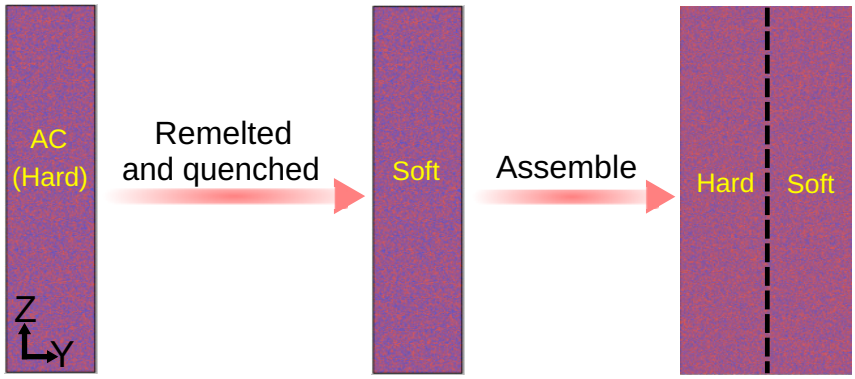


**Figure 7.27:** Schematic diagram of Hard-Soft heterostructure preparation.

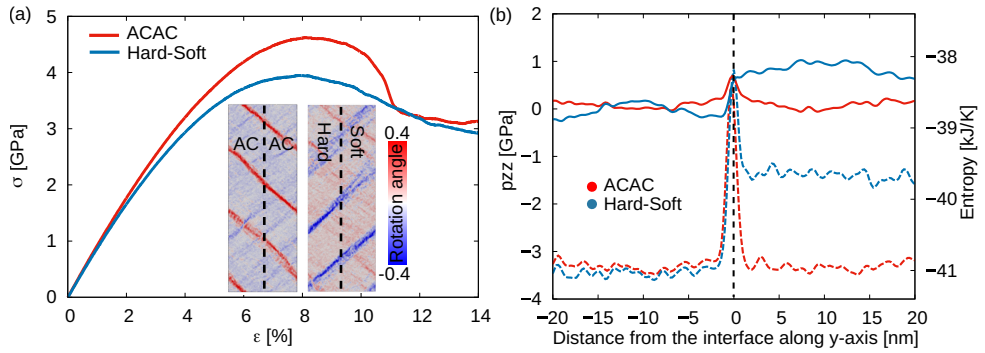


**Figure 7.28:** (a): Stress-strain curves together with snapshots of the rotation angle at $\varepsilon$ = 14% for the ACAC sample and a Hard-Soft sample. (b): Variation of stress (solid lines) and local entropy (dashed lines) across the interface ($y$ = 0) when $\varepsilon$ = 0%.

In Fig. S2 (a) the deformation mechanisms in the ACAC sample and a structural modulated (Hard-Soft) heterostructure are compared. After yielding, one shear band forms and extends across the interface transecting the ACAC sample and leading to brittle-like fracture. Otherwise, in the Hard-Soft heterostructure, shear band branching and multiplication commence when the shear band reaches the interface. Here, structural fluctuations, in terms of topological

disordering in the soft phase, perturb the STZ percolation process and hinder the formation of critical shear bands. The distribution of the local entropy effectively representing the atomic-level local structure of $Cu_{64}Zr_{36}$ metallic glass, displays a strong variation in the Hard and Soft regions (Fig. 7.28 (b)). Nevertheless, the weak fluctuation of the stress across the interface indicates a homogeneous stress distribution in the Hard-Soft heterostructure.

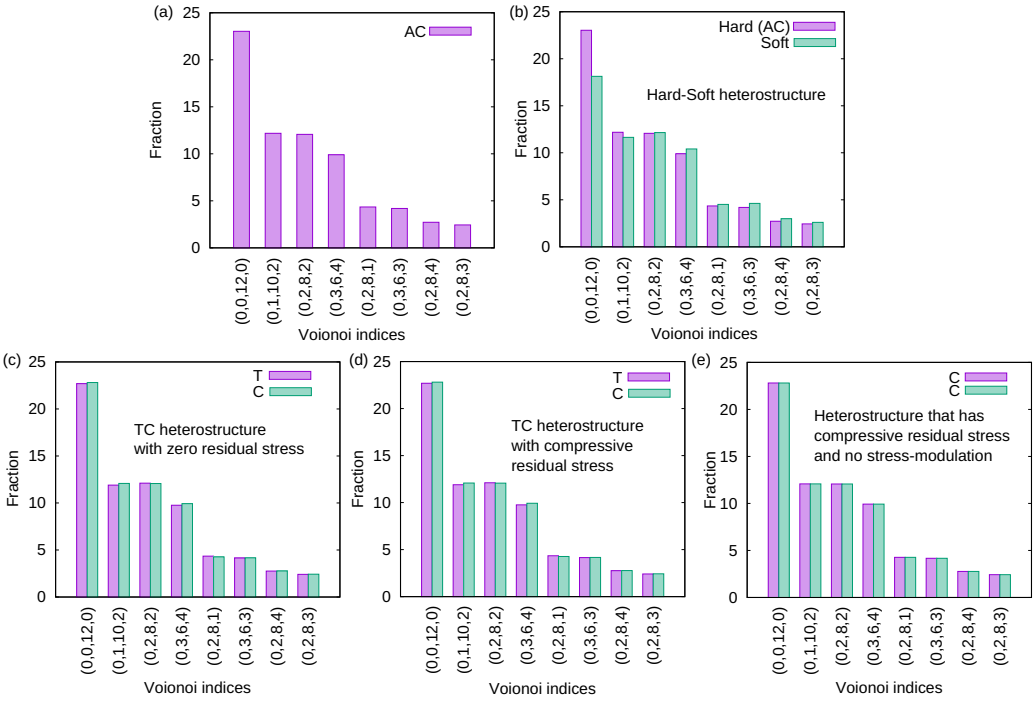


**Figure 7.29:** (b), (c), (d) and (e) shows the atomic-level structure of all the designed heterostructures while the structure of the initial AC block is shown in (a) for comparison. As we mentioned, it is obvious that the elastic pre-compression process we applied in the present work did not cause significant changes to the atomic structure in the glassy blocks.

### S3: Rotation angle calculation

In OVITO, the local rotation R is encoded as a quaternion R=(X, Y, Z, W) and is output by the modifier as a particle property named Rotation. The angle of rotation can be visualized by using the Compute Property modifier as follow: $2\times\ acos$(Rotation.W). Additionally, the sign of rotation angle with respect to a certain direction can be calculated: $sign$(Rotation.X)$\times 2\times\ acos$(Rotation.W), where, in our case, X is the direction perpendicular to shear plan.

In the present work we use the rotation angle instead of the atomic strain to visualized the deformation behaviour in metallic glasses since the sign of rotation angle with respect to a certain direction can be calculated and, hence, one can also visualize the shear band orientations (blue and red colors), along 45° and -45° with respect to the loading direction.

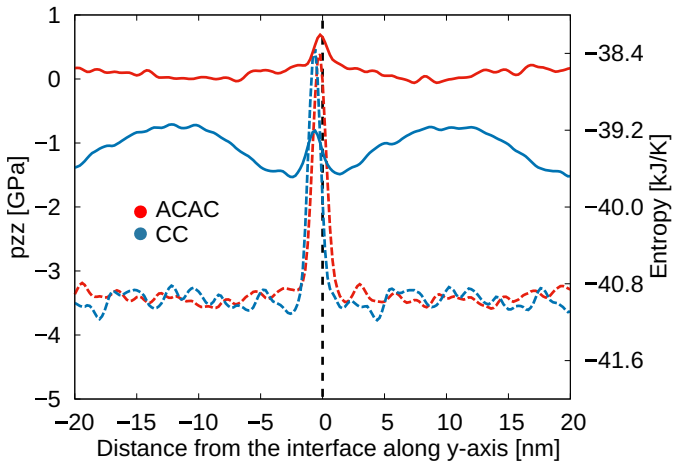


**Figure 7.30:** The distribution of stress (solid lines) and local entropy (dashed lines) along the y-axis in the CC and ACAC samples at $\varepsilon = 0\%$.

### S4: Local entropy calculation

Piaggi et al. (main text, Ref. [23]) introduced a novel structural fingerprint based on an approximate expression for the entropy projected on individual atoms in order to distinguish between order and disordered local environment. The radial distribution function $g_m^i(r)$ for an atom $i$ that is surrounded by an atoms $j$ at a distance $r_{ij}$ is given by

$$g_m^i(r) = \frac{1}{4\pi\rho r^2} \sum_j \frac{1}{\sqrt{2\pi\sigma^2}} e^{(r-r_{ij})^2/(2\sigma^2)}, \tag{10}$$

where $\rho$ is the average density in the glass and $\sigma$ is a broadening parameter.

The atom positions are broadened by a Gaussian peak. The entropy equation is based on an expansion of the entropy of liquid systems in n body correlation functions. For the local atom based entropy only the two body term is considered:

$$s_2^i(r) = -2\pi\rho k_B \int_0^{r_m} \left[ g_m^i(r) \ln(g_m^i(r)) - g_m^i(r) + 1 \right] r^2 \, dr \tag{11}$$

The local entropy is evaluated at each atomic site including the neighboring atoms within a cutoff range of 6 (including the second neighbor shell).

### S5: Atomic-level structure analysis

Fig. 7.29 shows the atomic-level structure of all the samples that we designed in the present work. The structure was represented by the fraction of Cu-centered short-range order clusters and analyzed using the OVITO software (main text, Ref. [25]) which includes an analysis

modifier that calculates the Voronoi tessellation (main text, Ref. [24]).

**S6: The stress and entropy distributions of the CC sample**

Fig. 7.30 shows the distribution of stress and local entropy along the y-axis in the CC sample as comparison to ACAC sample.